Identification of forming limits of sheet metals with an in-plane biaxial tensile test

Xiao Song

Thèse

UNIVERSITE BRETAGNE LOIRE

THESE INSA Rennes
sous le sceau de l'Université Bretagne Loire
pour obtenir le titre de
DOCTEUR DE L'INSA RENNES
Spécialité : Génie Mécanique

présentée par
Xiao SONG
ECOLE DOCTORALE : *SPI*
LABORATOIRE : *LGCGM*

Identification of forming limits of sheet metals with an in-plane biaxial tensile test

Thèse soutenue le 27.03.2018
devant le jury composé de :

Pierre-Olivier BOUCHARD
Professeur, CEMEF, Mines ParisTech / Président
Pascale BALLAND
Professeur, Lab. SYMME, Univ. Savoie Mont Blanc / Rapporteur
Sébastien THIBAUD
Professeur, Institut FEMTO-ST, ENSMM / Rapporteur
Eric RAGNEAU
Professeur, LGCGM, INSA de Rennes / Directeur de thèse
Lionel LEOTOING
Maître de Conférences, LGCGM, INSA de Rennes / Co-encadrant
Dominique GUINES
Maître de Conférences, LGCGM, INSA de Rennes / Co-encadrant

Identification of forming limits of sheet metals with an in-plane biaxial tensile test

Xiao SONG

En partenariat avec

This is for you, my dear Nan

Thank you for accompanying and supporting me in France

Abstract

Sheet metal forming is very common in industry for producing various components. The optimal use of materials, like light alloys or high strength steels in transportation for energy economy, requires in-depth analysis of their formability. Usually, the formability of sheet metal is controlled by the onset of localized necking, and the forming limit curve at necking (FLCN), generally restricted to linear strain paths, is adopted. However, under specific loadings (complex strain paths, near balanced biaxial stretching ...), ductile fracture can be induced without any obvious necking phenomenon. In that case, the fracture rather than the necking characterizes the formability, and the forming limit curve at fracture (FLCF) should be considered.

For identifying FLCN and FLCF under linear and non-linear strain paths, conventional methods require different experimental devices and geometrical specifications of specimen to follow various strain paths. Using the in-plane biaxial tensile test with a cruciform specimen can be an interesting alternative to overcome the drawbacks of conventional methods. The strain path during the test can be directly controlled by the motion of four independent actuators, which is sufficient to cover a wide range of strain paths, just with one shape of cruciform specimen. Besides, changes of strain path are made during the same test, without unloading.

The first objective of this study is to show that the in-plane biaxial tensile test with a single type of cruciform specimen permits to investigate the FLCN and FLCF of sheet metals under different strain paths including linear and non-linear evolutions. Firstly, in-plane biaxial tensile tests have been carried out on AA5086 sheets with an original thickness of 4 mm by testing a dedicated cruciform specimen, already optimized in the laboratory. The forming limit strains at fracture of AA5086 sheet under linear and non-linear strain paths (uniaxial tension followed by equi-biaxial stretching) have been characterized. Thinner sheet metals are often used in industry, so a new shape of cruciform specimen with an

original thickness of 2 mm was proposed and optimized step by step. This new cruciform specimen is successfully used to investigate the formability of DP600 sheet under linear and two types of non-linear strain paths.

The second objective is to discuss the validity of commonly used ductile fracture criteria to predict the onset of fracture for sheet metal by means of a finite element simulation of the in-plane biaxial tensile test. Some ductile fracture criteria from literature were selected (Cockroft and Latham, Ayada, Oyane ...) and calibrated with experimental results to produce numerical FLCFs for AA5086 and DP600 sheet. Depending on the fracture criterion, numerical results can give very different predictions. Finally, for the two tested materials, it is possible to find a criterion that can predict well the experimental FLCFs for either linear or non-linear strain paths.

Résumé

Les procédés de mise en forme des tôles minces sont largement utilisés dans l'industrie pour la production de pièces très diverses. L'utilisation optimale des matériaux constitutifs de ces tôles, comme les alliages légers ou les aciers à haute résistance, propices à des économies d'énergie dans le domaine des transports, nécessite une connaissance approfondie de leurs limites de formabilité. Classiquement, la formabilité d'une tôle est caractérisée par son aptitude à se déformer sans apparition d'une striction localisée. L'outil associé est la courbe limite de formage à striction (CLFS) qui est généralement caractérisée pour des chemins de déformation linéaires. Cependant, pour des chargements spécifiques (chemins de déformation complexes, traction équi-biaxiale, ...), une rupture ductile peut être induite avant apparition d'une forme de striction. Dans ce cas, la rupture plutôt que la striction caractérise la formabilité du matériau, la courbe limite de formage à la rupture (CLFR) doit alors être considérée.

Pour identifier la CLFS et la CLFR pour des chemins de déformation linéaires et non-linéaires, les méthodes conventionnelles requièrent différents dispositifs expérimentaux et différentes formes d'éprouvette pour atteindre une large gamme de chemins de déformation. L'essai de traction biaxiale, associé à une éprouvette cruciforme, est une alternative intéressante à ces méthodes. Le chemin de déformation suivi durant l'essai est directement contrôlé par le mouvement de quatre vérins indépendants. Ce dispositif permet de couvrir une large gamme de chemin, à partir d'une forme unique d'éprouvette cruciforme. De plus, le changement de chemin est activé au cours de l'essai, sans déchargement.

Le premier objectif de cette étude est de montrer que l'essai de traction biaxiale, associé à une forme unique d'éprouvette cruciforme, permet de tracer des CLFS et des CLFR pour plusieurs chemins de déformation, qu'ils soient linéaires ou non-linéaires. En premier lieu, des essais ont été réalisés sur des tôles d'alliage d'aluminium 5086 (épaisseur initiale de 4 mm) à partir d'une forme d'éprouvette déjà proposée au laboratoire. Des déformations limites à rupture pour des chemins de déformation

linéaires et non linéaires (traction uniaxiale suivie d'une traction équi-biaxiale) ont été identifiées. Une nouvelle forme d'éprouvette cruciforme a été proposée pour des tôles moins épaisses (2 mm), plus répandues. L'éprouvette cruciforme optimisée a été validée pour étudier la formabilité d'un acier dual phase DP600 pour deux types de chemin de déformation non-linéaires.

Le deuxième objectif est de discuter la validité de critères classiques de rupture ductile à partir d'une simulation par éléments finis de l'essai de traction biaxiale. Plusieurs critères de rupture existants ont été sélectionnés (Cockroft et Latham, Ayada, Oyane) et calibrés à partir des données expérimentales pour tracer des CLFR numériques pour les deux matériaux étudiés. Les CLFR obtenues peuvent être très différentes mais, pour chaque matériau, un critère a finalement été identifié pour prédire assez précisément les résultats expérimentaux.

Contents

General introduction

Sheet metal forming is a widely used method for producing various components for different fields of application. Great effort has been made for energy economy in transportation by using light alloys or high strength steels. The optimal use of these materials requires in-depth analysis of their formability. Usually, the formability of sheet metal is controlled by the onset of localized necking, and the forming limit curve at necking (FLCN), generally restricted to linear strain paths, is adopted. However, under specific loadings (complex strain paths, near balanced biaxial stretching ...), ductile fracture can be induced without any obvious necking phenomenon. In that case, the fracture rather than the necking characterizes the formability, and the forming limit curve at fracture (FLCF) should be considered.

For identifying the FLCN and FLCF under linear strain paths, conventional methods require different geometrical specifications to produce different strain paths from equibiaxial stretching to uniaxial tension through plane-strain tension. For identifying the FLCN and FLCF under non-linear strain paths, a two-step procedure for controlling the strain paths is adopted. Taking the strain path under uniaxial tension followed by equibiaxial stretching for an example, the prestrains are realized by uniaxial tensile tests in the first step of loading and the Marciniak tests will be performed on the prestrain sheet metals in the second step of loading. There are also some disadvantages for this two-step procedure. Firstly, many experimental devices are required to realize different strain path changes. Secondly, the unloading between two steps of loading for changing the strain path is obligatory and the measure of strain path is not continuous between the two steps. Thirdly, only simplistic prestrains can be applied which makes impossible to study the formability under multiple strain path changes.

Using the in-plane biaxial tensile test with a cruciform specimen to identify the FLCN and FLCF under linear and non-linear strain paths could be an interesting alternative to overcome the drawbacks of conventional methods. The in-plane biaxial tensile test with the cruciform specimen is frictionless, without influence of bending. The strain path during the test can be directly controlled by the motion of four independent actuators, which is sufficient to cover a wide range of linear and non-

linear strain paths, just with one shape of cruciform specimen. However, a dedicated shape for the cruciform specimen must be designed in order to observe the onset of necking and the following fracture in the center of specimen. This condition permits to control the strain path of the necking zone.

In this work, the experimental and predictive forming limits at necking and fracture of AA5086 and Dual Phase Steel DP600 sheets under linear and non-linear strain paths are investigated by using the in-plane biaxial tensile test with two dedicated cruciform specimens.

In Chapter 1, an introduction of sheet metal forming process and mechanical behavior models of sheet metals is performed firstly. Then, the identification of sheet metal formability based on FLCN and FLCF is reviewed. Lastly, a review for the investigation of fracture locus based on stress triaxiality is presented.

In Chapter 2, an existed cruciform specimen is used to identify the forming limits at fracture of AA5086 sheet with an original thickness of 4 mm firstly. A method based on the strain evolution and the surface images of specimen is proposed for identifying the onset of fracture firstly. Then, different ductile fracture criteria are used to predict the experimental results by means of finite element method. Lastly, this cruciform specimen is used to identify the fracture locus in equivalent strain and stress triaxiality space. Because thinner sheet metals are often used in the automotive industry, a new shape of cruciform specimen should be designed for them.

In Chapter 3, a bibliographical review of designs of cruciform specimen for in-plane biaxial tension test is presented. Some useful rules have been concluded for designing the cruciform specimen. Four cruciform specimens in previous studies are selected and redesigned for obtaining the fracture in the center of specimen with an original thickness of 2 mm. Lastly, a new shape is proposed based on the comparison of those four specimens and then optimized step by step to obtain the fracture in the center. Experimental validation for the optimized shape of cruciform specimen needs to be performed.

In Chapter 4, the optimized cruciform specimen is used to identify the experimental forming limits at necking and fracture of DP600 sheet with a thickness of 2 mm under linear and non-linear strain paths. Two types of non-linear strain paths without unloading are considered. Different ductile fracture criteria are compared in the numerical simulations to predict the experimental results.

Introduction générale

Les procédés de mise en forme des tôles minces sont largement utilisés pour la production de composants divers, dans différents secteurs industriels. Afin de réduire la consommation d'énergie dans le domaine des transports, en allégeant notamment les structures, l'utilisation d'alliages légers ou d'aciers à haute résistance peut s'avérer très intéressante. L'utilisation optimale de ces matériaux nécessite une connaissance approfondie de leur formabilité. Classiquement, la formabilité d'une tôle est caractérisée par sa capacité à subir une déformation sans développer de striction localisée. L'outil associé à la caractérisation de la formabilité des tôles est la courbe limite de formage à striction (CLFS), généralement tracée pour des chemins de déformation linéaires. Cependant, pour des chargements spécifiques (chemins de déformation complexes, traction équi-biaxiale, ...), une rupture ductile peut se produire avant l'apparition d'une forme de striction. Dans ce cas, la rupture plutôt que la striction doit caractériser la formabilité du matériau, la courbe limite de formage à la rupture (CLFR) doit alors être établie.

Pour identifier la CLFS ou la CLFR pour des chemins de déformation linéaires, les méthodes conventionnelles nécessitent plusieurs formes d'éprouvette afin de suivre différents chemins de déformation (traction équi-biaxiale, traction uniaxiale, déformation plane, ...). Pour tracer une CLFS ou une CLFR pour des chemins de déformation non-linéaires, une procédure en deux étapes est classiquement adoptée. Pour obtenir un chemin de déformation sous traction uniaxiale suivi d'une traction équi-biaxiale par exemple, une pré-déformation est appliquée sur une tôle à partir d'un essai de traction uniaxiale. Des éprouvettes d'essais de type Marciniak peuvent ensuite être découpées dans la tôle pré-déformée pour être testées sous chargement équi-biaxial. Cette procédure présente de nombreux inconvénients. Tout d'abord, plusieurs dispositifs expérimentaux sont nécessaires pour effectuer les changements de chemin de déformation. Ensuite, la phase de déchargement entre les deux étapes de chargement est obligatoire, ce qui n'est pas toujours fidèle à l'évolution réelle des déformations dans la pièce formée. La mesure du champ de déformation est discontinue entre

les deux phases d'essai. Enfin, seules des pré-déformations simplistes peuvent être appliquées, ce qui rend impossible l'étude de la formabilité pour des changements multiples de chemin de déformation.

Le recours à l'essai de traction biaxiale sur éprouvette cruciforme pour identifier une CLFS ou une CLFR, pour des chemins de déformation linéaires ou non-linéaires, peut constituer une alternative aux méthodes conventionnelles. L'essai de traction biaxiale sur éprouvette cruciforme est réalisé sans frottement et le chemin de déformation suivi durant l'essai peut être contrôlé par le mouvement de quatre vérins indépendants. Ce dispositif permet de couvrir une large gamme de chemins de déformation linéaires ou non-linéaires, à partir d'une forme unique d'éprouvette cruciforme. Néanmoins, la forme de l'éprouvette cruciforme doit être optimisée afin d'observer l'apparition de la striction et de la rupture au centre de l'éprouvette. Cette condition permet de contrôler le chemin de déformation dans la zone centrale.

Dans ce travail, les limites de formage expérimentales et prédites, à striction et à rupture, seront évaluées et comparées pour des tôles en alliage d'aluminium AA5086 et en acier dual phase DP600. Ces limites seront étudiées pour des chemins de déformation linéaires et non-linéaires grâce à deux formes dédiées d'éprouvette cruciforme.

Dans le premier chapitre, après une brève introduction sur les procédés de formage des tôles minces et des modèles de comportement mécanique des tôles, une revue sur la caractérisation expérimentale et numérique des limites de formage à striction et à rupture est proposée. Cette revue bibliographique concerne également la caractérisation de la formabilité sous chargement linéaire et non-linéaire. L'utilisation du taux de triaxialité des contraintes pour représenter les différents états de chargement est également présentée à la fin de ce chapitre.

Dans le deuxième chapitre, une éprouvette cruciforme existante est utilisée pour identifier les limites de formage à rupture de tôles en alliage d'aluminium AA5086 ayant une épaisseur initiale de 4mm. Une méthode basée sur le suivi temporel des déformations et sur l'analyse des images de la surface de l'éprouvette, permet d'identifier le temps correspondant à l'apparition de la rupture. Ensuite, différents critères de rupture ductile sont évalués pour prédire les limites de formage pour le même matériau, grâce à la méthode des éléments finis. A la fin de ce chapitre, cette éprouvette cruciforme est utilisée pour identifier la courbe limite en fonction de la déformation équivalente et du taux de triaxialité des contraintes. La forme d'éprouvette étudiée ne s'appliquant pas aux tôles moins épaisses, pourtant plus répandues, l'objectif de la suite de la thèse est de proposer une nouvelle forme capable de couvrir une plage d'épaisseur plus large.

Dans le troisième chapitre, une revue bibliographique des formes d'éprouvette

cruciforme déjà utilisées pour des essais de traction biaxiale est tout d'abord présentée. Cette revue permet d'établir quelques règles claires pour la définition de la forme d'une éprouvette cruciforme. Suite à cette étude préliminaire, quatre éprouvettes présentant un potentiel intéressant sont sélectionnées et modifiées pour obtenir une rupture au centre. L'épaisseur initiale de l'éprouvette est fixée à 2mm. Enfin, suite à la comparaison des performances de ces quatre premières éprouvettes, une nouvelle forme est proposée puis optimisée en évaluant l'impact de plusieurs paramètres sur le lieu d'apparition de la rupture. La validation expérimentale de cette nouvelle forme d'éprouvette est notamment réalisée dans le chapitre suivant.

Dans le dernier chapitre, l'éprouvette cruciforme optimisée est utilisée pour identifier les limites expérimentales de formage à striction et à rupture pour des tôles de DP600 d'épaisseur initiale 2mm. Les essais sont réalisés en suivant des chemins de déformation linéaires et non-linéaires. Pour cette dernière configuration, deux types de chemins de déformation non-linéaires, sans phase de déchargement, sont considérés. Les performances de plusieurs critères de rupture ductile sont évaluées en comparant les résultats expérimentaux et numériques.

Chapter 1

Identification of sheet metal formability

Résumé

Dans ce chapitre, les modes de déformation rencontrés dans les procédés de mise en forme, conventionnels (emboutissage, ...) ou non-conventionnels (formage incrémental, ...) des tôles minces sont tout d'abord brièvement rappelés. Par la suite, une revue bibliographique des principaux travaux récents concernant la détermination des limites de formabilité des tôles minces est proposée. Dans cette revue, les principaux moyens expérimentaux et critères de détection de l'apparition de la striction et de la rupture sont présentés à la fois pour des chemins de chargement linéaires et non-linéaires. Les modèles prédictifs d'apparition de la striction et de la rupture ductile les plus généralement utilisés dans la litérature dans le cadre de la mise en forme des tôles métalliques minces sont également succinctement décrits. Finalement, quelques travaux récents traitant de l'influence de la triaxialité des contraintes sur les modes et limites de déformation à rupture des matériaux métalliques sont présentés.

A l'issue de cette étude bibliographique, il apparait que l'essai de traction biaxiale sur éprouvette plane cruciforme peut être une alternative intéressante aux moyens conventionnels (de type Marciniak ou Nakazima) pour caractériser à la fois les courbes limites de formage à striction et à rupture. L'essai de traction biaxiale ne nécessite la définition que d'une seule forme d'éprouvette pour balayer l'ensemble des chemins de déformation allant de l'état équi-biaxial à l'état uniaxial, le chemin de déformation au centre de l'éprouvette étant directement piloté par le déplacement sur les deux axes de l'éprouvette. De plus cet essai permet d'imposer des chemins de déformation linéaires et non-linéaires tout en s'affranchissant des problèmes de frottement rencontrés dans les tests classiques. Enfin, ce dispositif permet d'imposer des chargements complexes (enchaînement de plusieurs chemins de déformation linéaires ou non) sans avoir à décharger l'éprouvette entre chaque chemin impose comme c'est le cas avec les moyens d'essais classiques.

1.1 Introduction

In this chapter, an introduction of sheet metal forming processes, modes of deformation and formability in sheet metal forming is produced firstly in Section 1.1. Then, the mechanical behavior modeling of sheet metal including yield criterion, flow rule and hardening law is presented in Section 1.2. The identifications of sheet metal formability based on the analysis of necking and fracture in previous researches are reviewed in Section 1.3 and Section 1.4, respectively. Lastly, a review of sheet metal formability based on fracture locus in stress triaxiality and equivalent strain is presented in Section 1.5.

1.1.1 Sheet metal forming processes

Sheet metal forming is a widely used method for producing various components for different fields of application, for example automotive and aeronautic industries. The sheet metal forming processes can be classified in two categories: traditional sheet metal froming processes and innovative sheet metal forming processes.

Traditional sheet metal forming processes

Deep drawing is one of the most widely used sheet metal forming process. Figure 1.1 shows an example of deep drawing, in which a punch pushes downward on the sheet metal to force it into a die cavity in the shape of a cup. Deep drawn parts are characterized by a depth equal to more than half of the diameter of part. These parts can have a variety of cross sections with straight, tapered, or even curved walls, but cylindrical or rectangular parts are most common. Examples of part formed by deep drawing include automotive bodies, fuel tanks, cans, cups, kitchen sinks and pots.

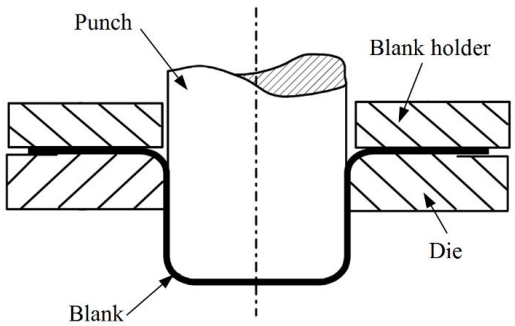

Figure 1.1: Deep drawing of a cylindrical cup

Figure 1.2 shows the stretch forming process, in which a flat sheet metal is stretched and bent simultaneously over a die in order to form large contoured parts.

The sheet metals can be formed varying from a simple curved surface to complex non-uniform cross sections. Typical stretched formed parts are large curved panels such as door panels in cars or wing panels on aircraft.

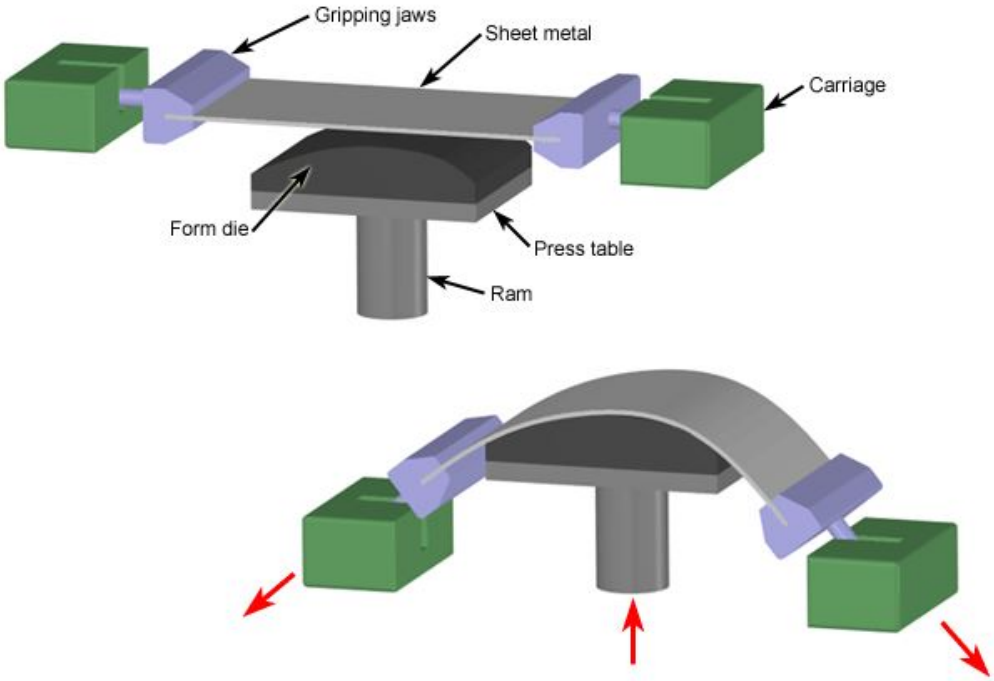

Figure 1.2: Stretch forming process

Innovative sheet metal forming processes

Single point incremental forming (SPIF) is an innovative sheet metal forming process. The representation of SPIF process is shown in Figure 1.3. The blankholder is utilized for clamping and holding the sheet metal in position. The backing plate supports the sheet metal and its opening defines the working area of the single point forming tool. The tool is used to progressively shape the sheet metal into a component and the whole forming process is controlled entirely by computer numerical control processes. The die in traditional sheet metal forming process is not required in the SPIF.

Hydroforming is a cost-effective and specialized type of die molding that utilizes highly pressurized fluid to form sheet metal. Generally there are two classifications used to describe hydroforming: tube hydroforming and sheet hydroforming. As shown in Figure 1.4, tube hydroforming is the expansion of metal tubes into a shape using two forming dies, which contain the raw tube. Sheet hydroforming uses one die and a sheet of metal. The blank sheet is driven into the die by high pressure

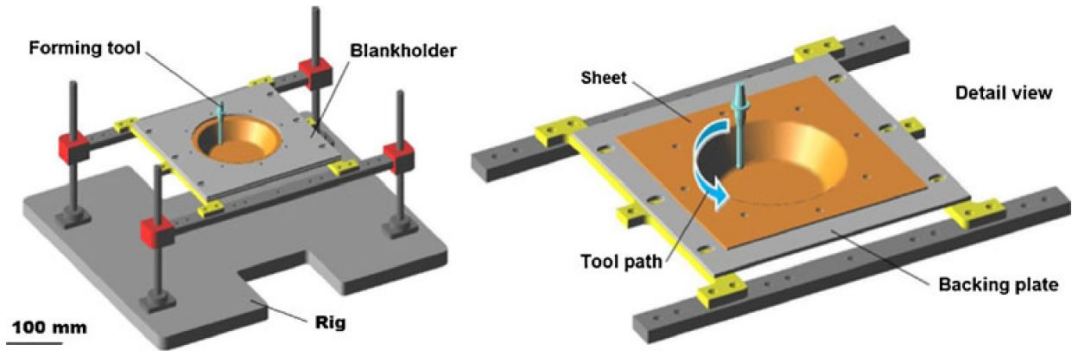

Figure 1.3: Single point incremental forming process [1]

water on one side of the sheet forming the desired shape.

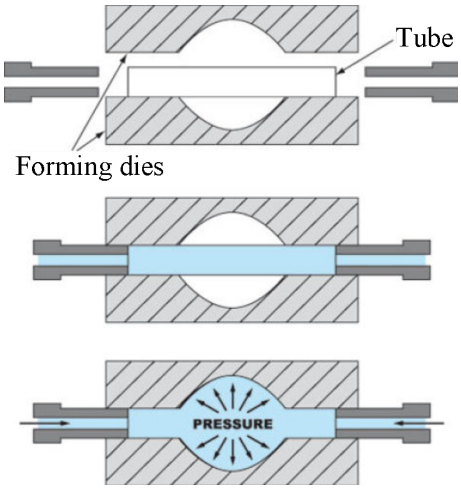

Figure 1.4: Tube hydroforming

1.1.2 Modes of deformation

In the principal strain space (ε_1, ε_2, ε_3) with the assumption of $\varepsilon_1 \geq \varepsilon_2 \geq \varepsilon_3$, ε_1 and ε_2 are named as the major and minor principal strains in the plane of sheet metal. In the principal stress space (σ_1, σ_2, σ_3), because the thickness is much smaller then length and width, the stress along thickness direction is generally neglected (σ_3=0). The sheet metal forming is mainly driven by stretching and plane stress condition exists [2].

Strain path is defined by the ratio of minor and major principal strains $\varepsilon_2/\varepsilon_1$. Due to the geometrical constraints and boundary conditions during sheet metal forming, different regions of the blank are deformed under various strain paths [3]. Deep drawing of a cylindrical cup is taken as an example in Figure 1.5. Different loading conditions: uniaxial tension, plane-strain tension and equibiaxial stretching

can be found in different regions of the blank.

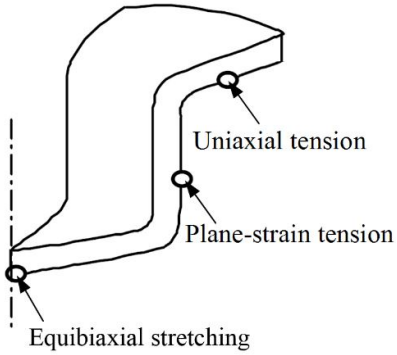

Figure 1.5: Different loading conditions in a deep drawing cylindrical cup

As shown in Figure 1.6, the path 0A indicates equibiaxial stretching ($\varepsilon_2/\varepsilon_1$=1). The strains are equal in all directions and a grid circle expands uniformly. The plane-strain tension ($\varepsilon_2/\varepsilon_1$=0) is illustrated by 0B. The sheet extends only in one direction and a circle becomes an ellipse in which the minor strain is unchanged. The path 0C shows the uniaxial tension ($\varepsilon_2/\varepsilon_1$=-0.5).

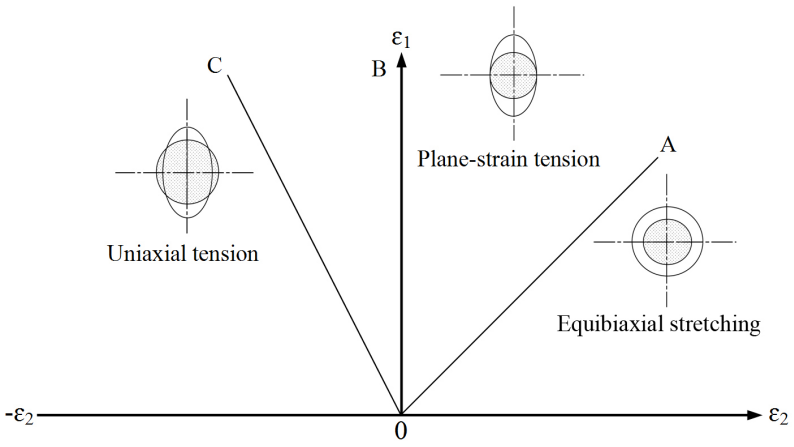

Figure 1.6: Schematic diagram of strain paths

As described in previous study [4], the mode of deformation during the SPIF process is complex, which has been demonstrated by using finit element method and optical strain measurements. Figure 1.7 shows the strain path during SPIF for an AA3003-O sheet metal in numerical simulation.

1.1.3 Formability in sheet metal forming

In sheet metal forming operations, the material can be deformed only up to a certain limit. The ability of sheet metal to deform into a desired shape without local necking

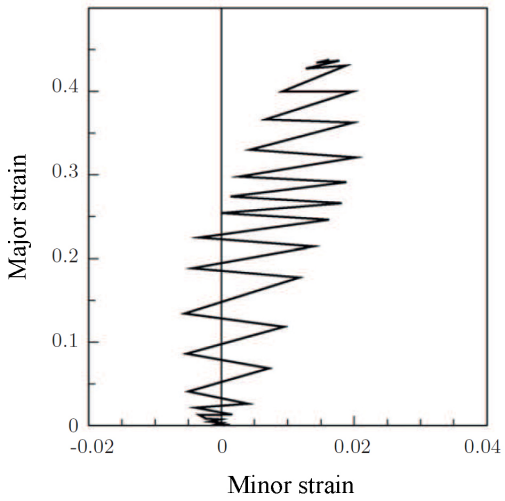

Figure 1.7: Strain path during SPIF

or fracture is defined as its formability. The most popular method to evaluate the formability of sheet metals is the forming limit diagram (FLD). A FLD is a major/minor strain diagram which can distinguish between safe points and necked or fractured points. The transition from safe to necked points is defined by the forming limit curve at necking (FLCN) or called forming limit curve (FLC), while the transition from safe to fractured points is defined by the forming limit curve at fracture (FLCF) or called fracture forming limit line (FFL) [5]. Figure 1.8 shows the schematic diagram of FLCN and FLCF. For a given initial strain path, after the onset of strain localization, the material forms a necking and continues to deform under an almost plane-strain path up to fracture. For the whole FLCN or FLCF, different strain paths from equibiaxial stretching to uniaxial tension across plane-strain tension are considered. In addition, the pure shear is also an interesting strain path to be investigated.

Formability of sheet metal may depend on many factors like material properties or process parameters (strain path, strain rate, temperature, etc). The design and optimization of forming operations with numerical tools need more and more accurate prediction of material formability in order to fully exploit its forming abilities. Thus, understanding and characterizing the formability of sheet metal are essential for controlling final product quality and then evaluating the success of sheet forming operation.

1.2 Mechanical behavior modeling of metallic sheets

The reliability of simulation process greatly depends on the material constitutive models. Three elements are needed to describe the plastic behavior of a material: a

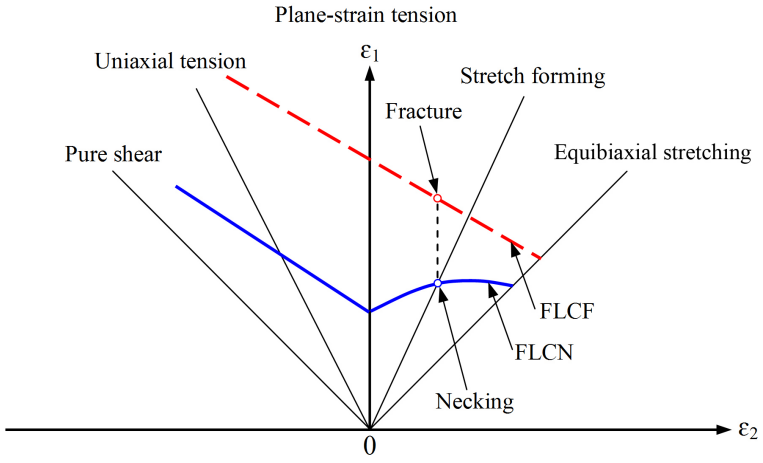

Figure 1.8: Schematic diagram of the FLCN and FLCF

yield criterion, a flow rule and a hardening law.

1.2.1 Yield criterion

The yield point defines the beginning of plastic deformation. When the stress passes the yield point, non-reversible plastic deformation occurs. The condition under which the plastic flow happens is known as the yield criterion. The yield criterion surface is usually described by an implicit equation with the form:

$$f(\bar{\sigma}, \sigma_0) = \bar{\sigma} - \sigma_0 \tag{1.1}$$

where $\bar{\sigma}$ is the equivalent stress and σ_0 is the yield stress from a simple test (tension, compression or shear). The yield criterion is a mathematical description of a three-dimension surface in the principal stress space. The plane stress condition is usually considered in sheet metal forming process, so the yield surface is reduced to a curve in the stress space (σ_1, σ_2). Figure 1.9 presents a typical yield contour and strain states.

Mises yield criterion

Von Mises has proposed a circle equation for isotropy materials in 1913, which is known as von Mises criterion. The material passes from elastic state to plastic state when a critical value of the elastic energy of distortion is reached. The equivalent stress $\bar{\sigma}$ can be obtained in terms of the general stress state from the relation:

$$2\bar{\sigma}^2 = (\sigma_{xx} - \sigma_{yy})^2 + (\sigma_{xx} - \sigma_{zz})^2 + (\sigma_{yy} - \sigma_{zz})^2 + 6(\sigma_{xy}^2 + \sigma_{xz}^2 + \sigma_{yz}^2) \tag{1.2}$$

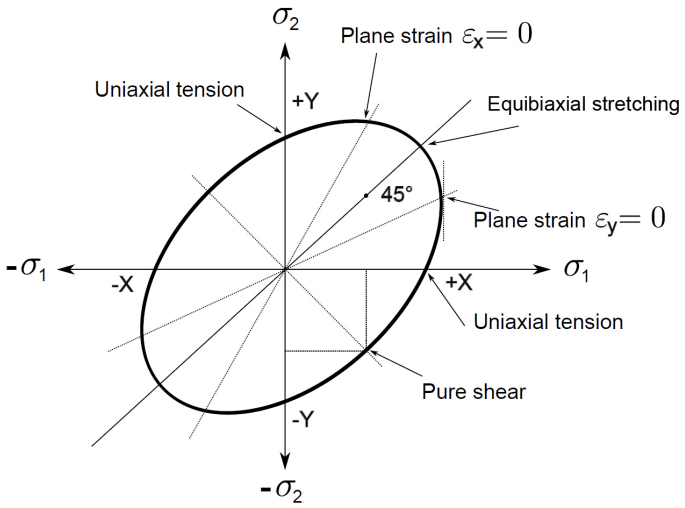

Figure 1.9: Yield contour and strain states

where σ_{xx}, σ_{yy}, σ_{zz} are three normal components of stresses along the coordinate directions in an arbitrary orthogonal coordinate set, and σ_{xy}, σ_{xz} and σ_{yx} are shear stresses.

In principal stress space, it is reduced to:

$$2\bar{\sigma}^2 = (\sigma_1 - \sigma_2)^2 + (\sigma_1 - \sigma_3)^2 + (\sigma_2 - \sigma_3)^2 \tag{1.3}$$

For the plane stress case of sheet metal $\sigma_3 = 0$:

$$\bar{\sigma}^2 = \sigma_1^2 - \sigma_1\sigma_2 + \sigma_2^2 \tag{1.4}$$

where σ_1, σ_2 and σ_3 are principal stresses.

Hill 48 yield criterion

Due to the crystallographic structure and the characteristics of rolling process, the sheet metal usually exhibits anisotropic behavior. Hill has proposed the anisotropic yield criterion in 1948. In the Hill 48 yield criterion, the equivalent stress is expressed by a quadratic function of the following type:

$$2\bar{\sigma}^2 = F(\sigma_{yy} - \sigma_{zz})^2 + G(\sigma_{zz} - \sigma_{xx})^2 + H(\sigma_{xx} - \sigma_{yy})^2 + 2L\sigma_{yz}^2 + 2M\sigma_{zx}^2 + 2N\sigma_{xy}^2 \tag{1.5}$$

For the plane stress case of sheet metal:

$$2\bar{\sigma}^2 = (G+H)\sigma_1^2 + (H+F)\sigma_2^2 - 2H\sigma_1\sigma_2 + 2N\sigma_{12}^2 \tag{1.6}$$

The parameters F, G, H, N of Hill 48 yield criterion for sheet metals can be determined by three anisotropic coefficients r_0, r_{45} and r_{90} as follows:

$$F = \frac{r_0}{r_{90}(1+r_0)} \tag{1.7}$$

$$G = \frac{1}{1+r_0} \tag{1.8}$$

$$H = \frac{r_0}{1+r_0} \tag{1.9}$$

$$N = \frac{(1+2r_{45})(r_0+r_{90})}{2r_{90}(1+r_0)} \tag{1.10}$$

When $F = G = H = 0.5$ and $N = 1.5$, Hill 48 yield criterion becomes Mises criterion.

There are also some other yield criteria, for example advanced anisotropic yield criteria of Yld2000-2d, Yld2004-18p, Yld2004-13P, BBC2005, and Bron and Besson 2004 et al..

1.2.2 Flow rule

The flow rule governs the plastic flow and the determination of plastic strain increment $d\varepsilon_{ij}^p$. A classical associated flow rule is often used for many cases of metal plasticity:

$$d\varepsilon_{ij}^p = d\lambda \frac{\partial f}{\partial \sigma_{ij}} \tag{1.11}$$

where the plastic flow is assumed to occur along the normal direction of the yield surface and the scale is defined by the increment of plastic multiplier $d\lambda$.

1.2.3 Hardening law

The hardening law of material represents the stress evolution with plastic strain, temperature or strain rate, after the initial yield. As shown in Figure 1.10, there are two main models to describe the strain hardening: isotropic hardening and kinematic hardening. For isotropic hardening, the yield surface remains centered about its initial centerline and expands in size as the plastic strain develops. For the kinematic hardening, the yield surface remains constant in size and the surface translates in stress space with progressive yielding. Most of materials need the two types of hardening at the same time to fully describle their mechanical behavior,

which is called combined hardening.

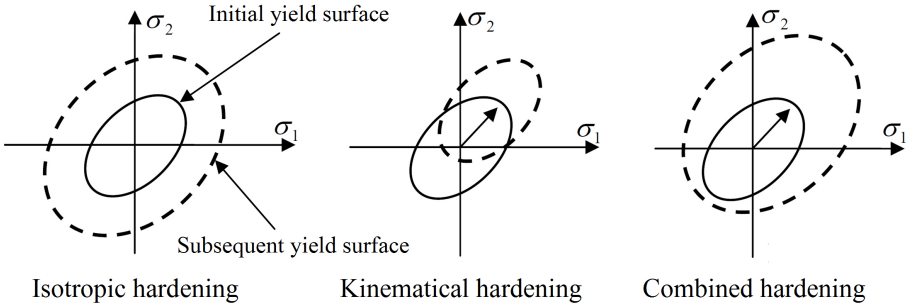

Figure 1.10: Hardening models

From the micro-scale point of view, when the material is deformed, dislocations will be generated and annihilated and then the texture evolution will occur. It is usually assumed that the concept of dislocation density links the flow stress to the underlying microstructure evolution. The flow stress σ can be calculated as follows [6]:

$$\sigma = \sigma_0 + \alpha G b(\delta - \delta_0) \tag{1.12}$$

where σ_0 is initial yield stress corresponding to the initial density δ_0 of dislocation, α is a material coefficient, G is the transversal elastic modulus, b is the Burgers vector and δ is the current dislocation density.

If the material is deformed under monotonic strain path without the thermal and strain-rate effect, the equivalent plastic strain $\bar{\varepsilon}_p$ is usually chosen to represent the dislocation density δ. In the similar way of Eq. 1.12, the hardening law can be expressed by a one-internal-variable model as following:

$$\bar{\sigma} = \sigma_0 + H(\bar{\epsilon}_p) \tag{1.13}$$

Where σ_0 is initial yield stress and $H(\bar{\epsilon}_p)$ represents the strain hardening effect.

Some widely used mathematical formulas of hardening laws are briefly introduced.

The unsaturated Ludwick law:

$$\bar{\sigma} = \sigma_0 + K(\bar{\epsilon}_p)^n \tag{1.14}$$

The saturated Voce law:

$$\bar{\sigma} = \sigma_0 + K(1 - exp(-n\bar{\epsilon}_p)) \tag{1.15}$$

Because it is found to become saturated too fast sometimes, the Voce law has

been modified to decrease the saturating effect, such as Hockett-Sherby law:

$$\bar{\sigma} = \sigma_0 + K(1 - exp(-n\bar{\epsilon}_p^m)) \tag{1.16}$$

A generalized Voce law [7] has also been suggested as follows:

$$\bar{\sigma} = \sigma_0 + K(1 - exp(-n\bar{\epsilon}_p))^{1/a} \tag{1.17}$$

The value of a varies with the type of crystallographic system: a=1/2 for a HCP structure, a=1 for a BBC structure and a=2 for a FCC one.

In the Section 1.2, the yield criteria including Mises yield criterion and Hill48 yield criterion, the flow rule, and the hardening law including Ludwick law, Voce law and modifed Voce law are presented. Those mechanical behavior models will be considered for the simulation in this study.

1.3 Identification of sheet metal formability based on FLCN

Necking is an undesirable surface defect in components made from sheet metals, so limits in sheet metal forming are most often controlled by localized necking rather than fracture [8]. In this section, different types of FLCN are introduced firstly. Then, the traditional and new experimental methods for identifying the FLCN and the criteria to detect the onset of necking are presented. Lastly, a review of experimental and predictive identification of FLCN under linear and non-linear strain paths is produced.

1.3.1 Forming limit curve at necking

Because the strain path change significantly affects the shape and location of the FLCN, there is no unified curve in strain space, which represents the forming limits of sheet metal [9]. Usually, the strain paths in sheet metal forming can be divided into two types: linear strain path and non-linear strain path. Traditionally, the strain-based FLCN concept is limited to the sheet metal undergoing linear strain path.

As shown in Figure 1.11, three types of experimental FLCN are identified by Barata et al. [10], which are commonly used to assess the effect of strain path on the level of limit strain.

For type 1, the FLCN is determined under proportional loading. Each point of the FLCN is defined by the limit strain at which localized necking occurs for

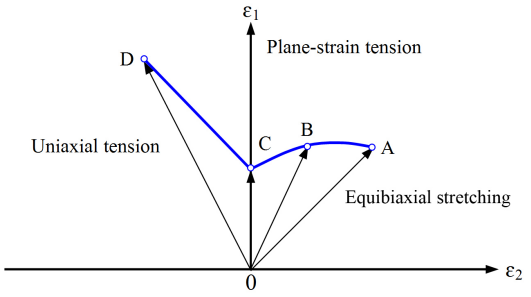

(a) Type 1 (linear strain path)

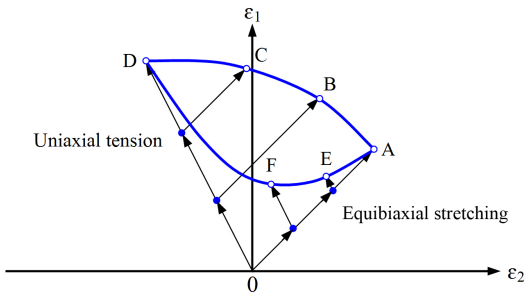

(b) Type 2 (non-linear strain path)

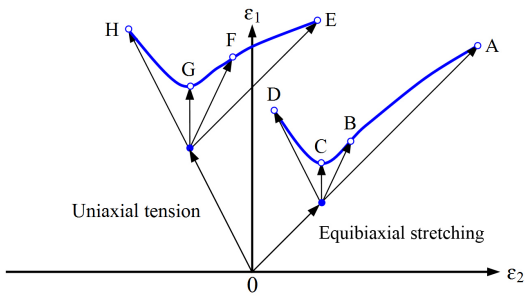

(c) Type 3 (non-linear strain path)

Figure 1.11: Three types of experimental FLCN

a constant imposed strain ratio. As shown in Figure 1.11 (a), the whole FLCN (ABCD) is therefore produced by varying the strain ratio from equibiaxial stretching (OA) to uniaxial tension (OD) through plane-strain tension (OC). For type 2, the FLCN is determined under non-proportional loading by using a sequence of two linear strain ratios. Different prestrain levels under a constant strain ratio P1 are used, and then an abrupt change is produced towards the strain ratio P2 for every prestrain level under strain ratio P1. As shown in Figure 1.11 (b), the curve ABCD is for the sequence consisting of uniaxial prestrain followed by equibiaxial stretching, and the curve AEFD is produced by different levels of equibiaxial prestrain followed by uniaxial tension. For type 3, the FLCN is determined under non-proportional loading by using a sequence of two linear strain ratios in which the preliminary strain ratio P1 and the prestrain level are kept constant. Different strain ratios are used after the prestrain. As shown in Figure 1.11 (c), for the curve ABCD the equibiaxial stretching is followed by different linear strain ratios, while for the curve EFGH the uniaxial tension is followed by different linear strain ratios.

1.3.2 Experimental methods for identifying FLCN

Traditional experimental methods

For experimental identification of FLCN, two main types of forming methods have been developed, the so-called out-of-plane stretching (Nakajima test in Figure 1.12 (a)) and the in-plane stretching (Marciniak test in Figure 1.12 (b)). In those tests, the sheet metal is clamped by a blank holder, and the center of sheet metal is deformed until fracture by applying a load with a punch. Different strain paths are realized by varying the widths of specimen. For out-of-plane stretching, the blank is deformed under triaxial stress while during in-plane-stretching, the sheet is under plane stress conditions in the central part.

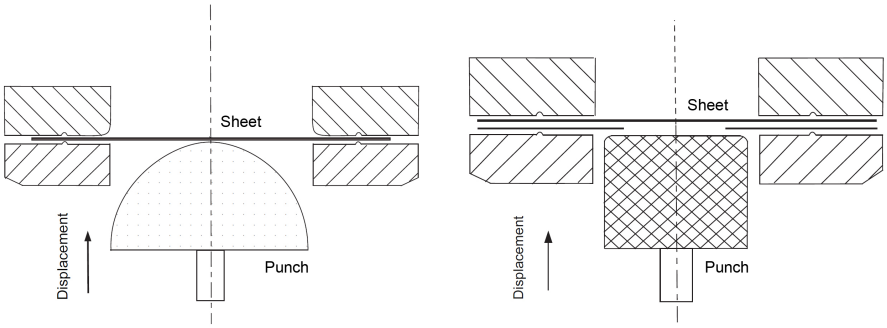

(a) Out-of-plane stretching (b) In-plane stretching

Figure 1.12: Two experimental methods for identifying the FLCN

Figure 1.13 shows an example of FLCN identified by the Marciniak's method. A number of sheet specimens with different shapes are used to produce different linear strain paths to cover the whole FLCN.

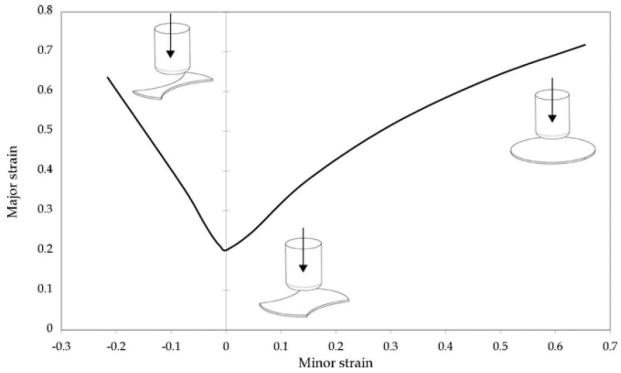

Figure 1.13: An example of FLCN for AA5086 sheet identified by the Marciniak's method with different shapes of specimen [11]

The main drawbacks of those traditional tests are the use of a high number of specimens with different geometrical properties to reach different strain paths, the influence of friction and the description of forming limit curves for simplistic linear strain paths.

New experimental method for identifying FLCN

The in-plane biaxial tensile test with a cruciform specimen is a new experimental method for identifying the FLCN [12]. The strain path in the center of cruciform specimen is directly imposed by the control of four actuators, independently on the specimen geometry. As shown in Figure 1.14, a unique shape of cruciform specimen is sufficient to cover the whole FLCN by using different loading conditions from equibiaxial stretching to uniaxial tension across plane-strain tension.

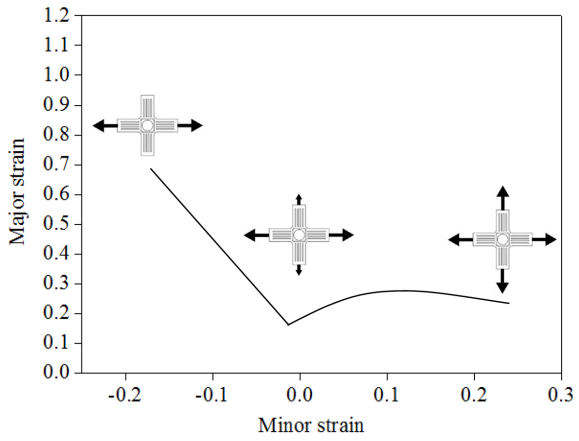

Figure 1.14: An example of FLCN for AA5086 sheet identified by the in-plane biaxial tensile test with a cruciform specimen [13]

1.3.3 Criteria to identify onset of necking

The main difficulty in identifying the experimental forming limit strains at necking lies in the choice of an appropriate criterion. Previous publications have provided a number of methods to idenfity the onset of necking, which can be divided into three types: position-dependent method, time-dependent method and time-position-dependent method.

All these criteria are analyzed based on strain measurement. Classically, the strains are obtained by the circle-grid method. A grid of circles (usually a diameter between 2 and 5 mm) is printed on the surface of sheet metal before forming. The forming limit major and minor strains are calculated by measuring the dimensions of the deformed circles near or at the fracture site, after the test. Such method suffers

from sensitivity to the initial size of the circles in the neighbourhood of the crack and the evolution of strain field is not followed during the test. Recently, the Digital image correlation (DIC) technique has been used for strain measurement. Using such optical measuring technique it is possible to get time dependent information on the strain distribution and the development of strain localizations, necking and failure. Details about the DIC method will be presented in the next chapter.

Position-dependent method

The standard ISO 12004-2: 2008 provides a position-dependent methodology to estimate the forming limit strains in Nakazima and Marciniak tests. This criterion is based on the strain distributions in the specimen before the occurence of a crack. The position values and strains (ε_1, ε_2) for each section point on the surface of the specimen can be obtained with the DIC method. The principle of ISO 12004-2 [14] is that, with a fit window on both sides of the necked area for a necked but not cracked specimen, a second order inverse polynomial function ($f(x) = 1/(ax^2 + bx + c)$) is fitted to determine the values of forming limit strain at the onset of necking. The crack position can be determined by the maximum value of the parabola. As shown in Figure 1.15, three sections (1, 2 and 3) are selected to obtain a reproducible evalution and the sections should be perpendicular to the crack. The average value of the forming limit strains in three sections is taken as one point of the FLCN.

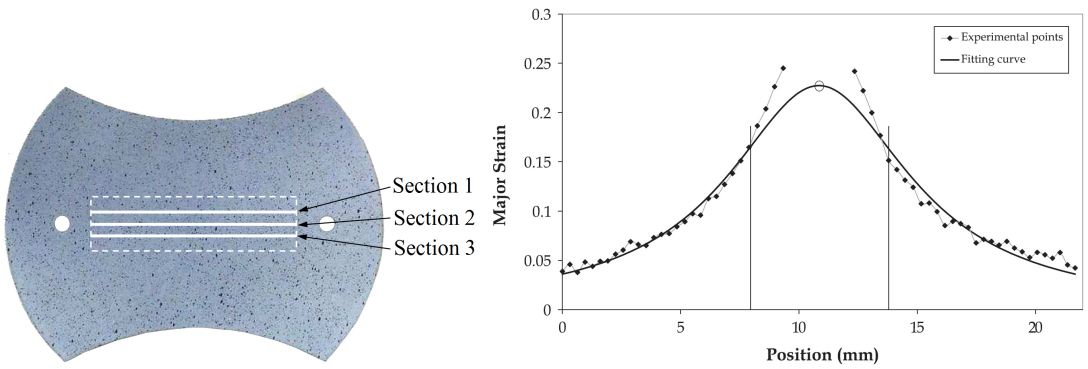

(a) Cross sections (b) Major strain distribution along section

Figure 1.15: ISO 12004-2 standard method

Chu [15] has proposed a modified method based on the ISO 12004-2. Different from the ISO 12004-2 standard, the value of forming limit strain ε_2 is directly calculated from the measured strain path β_{exp} through the expression $\varepsilon_2^{limit} = \beta_{exp}\varepsilon_1^{limit}$. This method limits data scatter on the FLCN especially near the plane strain condition.

The disadvantages of the standard cross-section analysis method are seen in the handling of samples with multiple necking zones and the analysis of failure behavior of high and ultra high strength steels, which may fail without showing an explicit necking zone before cracking. Moreover, when using small punch radii or in stretch-bending operations, this criterion is not applicable due to significant strain gradients across the sheet thickness.

Time-dependent method

The time dependent evaluation method is based upon a trend analysis of strain rate in the area of necking and subsequent cracking [16].

The strain rate values are calculated through all stages of the forming process. With the onset of necking the strain rate rises in the necking zone, whereas it decreases outside the necking zone. Figure 1.16 shows the different progress of strain rates inside and outside the necking zone. A detail analysis of the time derivate of strain rate is shown in Figure 1.17. A linear characteristic of the time derivative of strain rate is presented at the beginning of test and then it increases. A linear regression coefficient of the time derivative of strain rate is calculated. With an ongoing homogeneous plastic deformation, the linear regression coefficient starts to increase, reaching a maximum value at the onset of necking. After necking, the time derivative of strain rate decreases drastically and the linear regression coefficient increases. The maximum value of linear regression coefficient curve indicates the onset of necking, and the corresponding major and minor strain values represent the data point for the FLCN.

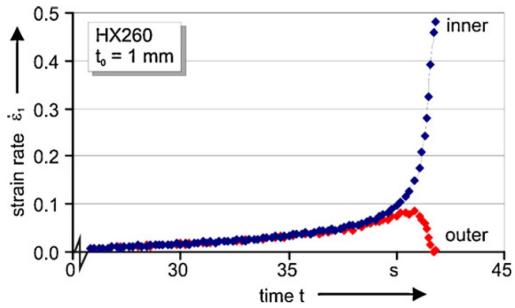

Figure 1.16: Comparison of strain rate progress inside and outside the necking zone [16]

The critical ratio method is a type of time-dependent method, which is based on different strain evolutions in the necking and adjacent zones. As shown in Figure 1.18, when the necking occurs in zone 1, a sharp change of equivalent strain is observed due to the onset of a plastic instability. In zone 2 (out of the necking zone), the level of equivalent strain remains stable and constant. When the equivalent

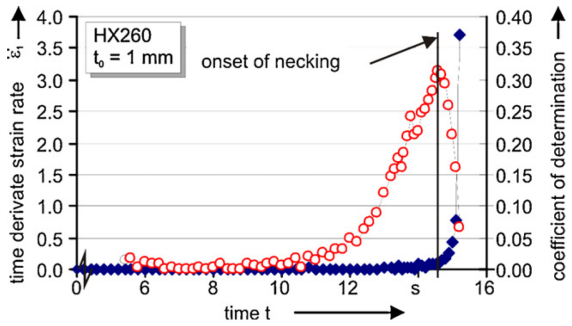

Figure 1.17: Determination of onset of necking using the time dependent analysis method [16]

strain increment ratio of the zone 1 and the zone 2 reaches a critical value, the corresponding major and minor strains of zone 1 define the forming limit strains at necking.

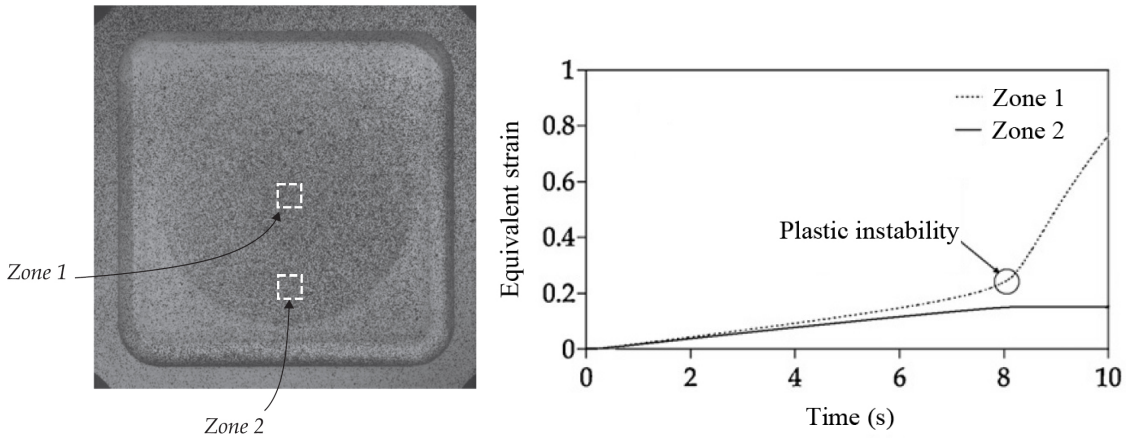

(a) Positioning of reference zones

(b) Evolution of equivalent strain

Figure 1.18: Critical ratio method

However, the critical value of strain incremental ratio depends on the position of reference zone. The choice of the time increment to calculate the strain increment has an influence on the value of the critical ratio.

Time-position-dependent method (flat-valley method)

The time-postion-dependent method or called flat-valley method [17] can be classified as a hybrid method that depends on both time and position. Figure 1.19 shows the vertical displacement of the outer surface of specimen along a section perpendicular to the failure region at different times until fracture in the conventional Nakazima test. The plane-strain tension is considered as example. At earlier times

of the forming process, the outer surface of sheet deforms by following to the curvature imposed by the punch. Later, this curve begins to flatten in a certain region, developing a necking valley (stage 222) which progressively deepens until the sheet fractures. At the moment of the beginning of necking, the profiles are approximately flat and the sheet is not able to deform with the curvature imposed by the punch and pointing, which shows the beginning of the plastic instability.

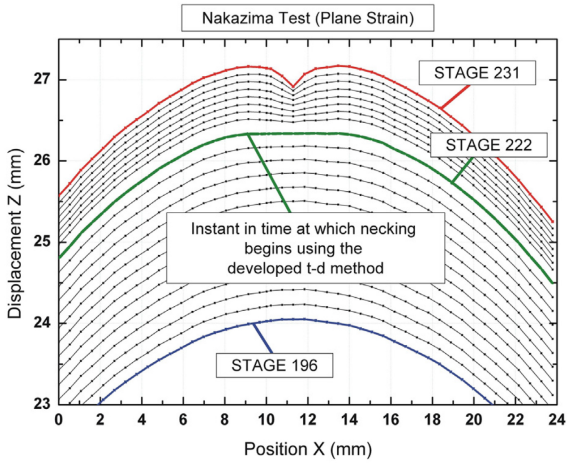

Figure 1.19: Time-position-dependent method [17]

1.3.4 Experimental identification of FLCN

Previous researchers have used the above-mentioned tests with different criteria to identify the FLCNs of sheet metals. A review of experimental identification of FLCNs under linear and non-linear strain paths is performed.

Linear strain paths

Chu et al. [18] have used the Marciniak test to investigate the experimental FLCNs of AA5086 sheet (t=2.0 mm) at different temperatures (20, 150 and 200 °C) and strain rates (0.02, 0.2, and 2 s^{-1}). The modified method based on the ISO 12004-2 is used to identify the onset of necking. As shown in Figure 1.20, different strain paths are followed by changing the specimen width (W) and the whole FLCN from uniaxial tension (W=10 mm) over plane-strain tension (W=50 mm) to biaxial stretching (W=100 mm) is built. The FLCNs of AA5086 sheet identified by different temperatures and strain rates are shown in Figure 1.21. It can be found that the forming limit strains at necking of AA5086 sheet increases with temperature and decreases with forming speed.

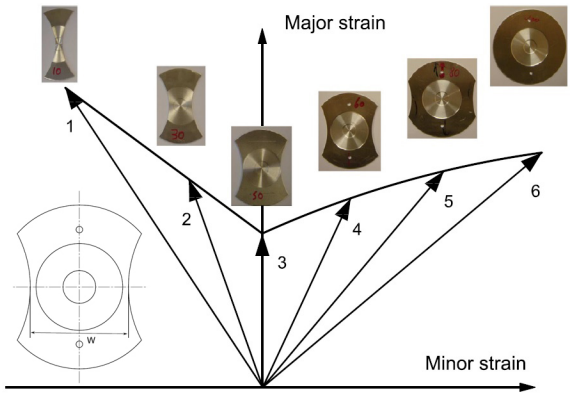

Figure 1.20: Specimen widths and strain paths

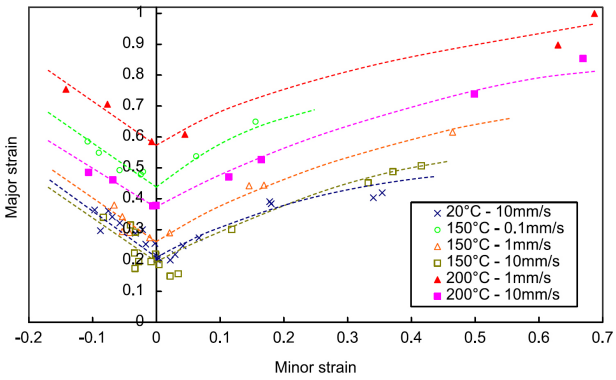

Figure 1.21: The FLCNs of AA5086 sheet under different temperatures and strain rates [18]

Silva et al. [19] have used the Nakazima test to identify the FLCNs of AA7075 sheet (t=1.6 mm) with different necking criteria. Different shapes of specimen are used to produce different strain paths to obtain the whole FLCN. Figure 1.22 shows the FLCNs identified by ISO 12004-2:2008 method, time-dependent method and flat-valley method. The results obtained by these three methods are similar. The maximum differences between the three approaches are in the range of 5% to 7%.

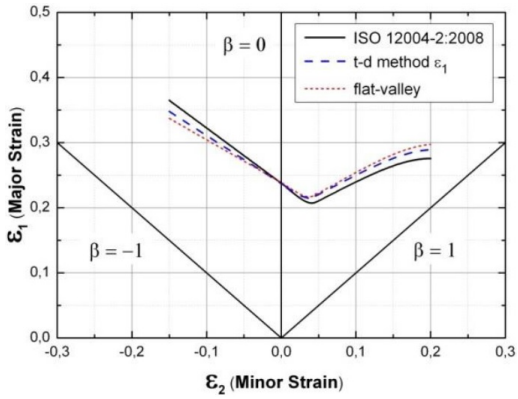

Figure 1.22: The FLCNs of AA7075 sheet identified by different failure criteria [19]

Zidane et al. [12] have used the in-plane biaxial tensile test with a cruciform specimen to determine the FLCN of AA5086 sheet (4 mm). A dedicated cruciform specimen is proposed through a numerical and experimental validation procedure. Because the necking is located in the central zone of the cruciform specimen, the speed ratio between the two axes of testing machine controls the strain path in this zone and a whole FLCN can be covered. The critical ratio method is adopted to identify the onset of necking under different linear strain paths. As shown in Figure 1.23, the solid points show the experimental forming limit strains at necking of AA5086 sheet. The Marciniak test has also been used to identify the forming limit strains at necking for this sheet and the results are shown in the figure. The FLCN identified by in-plane biaxial tensile test is slightly shifted compared to the minimum value of the major strain measured with the Marciniak test, while the average levels of forming limit strain obtained with the two experimental methods are rather comparable.

Non-linear strain paths

Most of the FLCNs have been experimentally determined using tools that produce proportional loading with insignificant changes in strain path. However, in sheet metal forming process, loadings are often non-proportional and strain path may change drastically [20]. Many researchers have demonstrated that the strain path

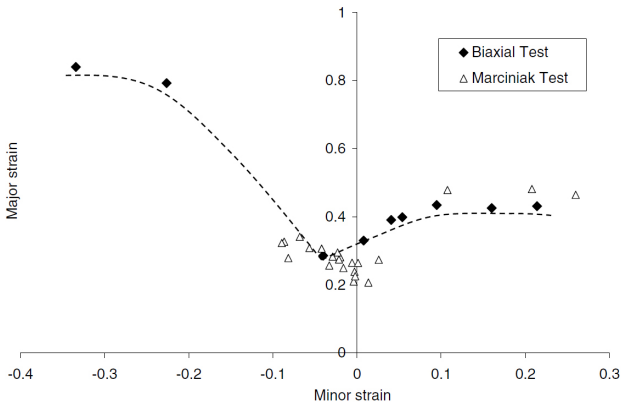

Figure 1.23: The forming limit strains at necking of AA5086 sheet identified by in-plane biaxial tensile test and Marciniak test [12]

change has a great influence on the level and shape of FLCN. An increase in formability can be achieved through careful choice of strain path [10].

For experimental identification of FLCN under non-linear strain path, a two-step procedure is always used to control strain path changes in the traditional experimental tests. Prestrains are generally realized by oversized tensile tests (uniaxial or plane-strain prestrains) and oversized Marciniak or bulge tests (biaxial prestrain). Afterwards, standard tests will be performed on the prestrain sheet metals.

Ishigaki [21] at Toyota Motors Company has applied the strain path change for improving the formability. As shown in Figure 1.24, the initial FLC is denoted by the gray line. The engineers recognized that at the end of stage 4, the gray curve is non valid as the formability limit. They used the prestrain in uniaxial tension to 37%, and then experimentally determine the shape of FLC. The result is shown as the red line in the figure, and it was used as an estimate of the residual formablity of the metal at the end of stage 1-4. Based on the red curve, the deformation process was modified to drive the strain to follow a new biaxial path during stage 5 and 6 to dramatically improve the formability.

Zhalehfar et al. [22] have investigated the effect of strain path change on the FLCN of AA5083 sheet (t=1 mm). Some sheets are pre-strained by uniaxial tension and some others are pre-strained by biaxial stretching over a hemispherical punch. As shown in Figure 1.25 (a), different geometries of specimen are used to complete the FLCN. The ISO 12004-2:2008 method is used to identify the forming limit strains at necking. Figure 1.25 (b) shows the FLCNs of AA5083 sheet under different non-linear strain paths. The prestrain in biaxial stretching generally reduces the FLCN and shifts it to the right-hand side of the FLD, whereas prestrain in uniaxial tension raises the FLCN and shifts it to the left-hand side.

Volt et al. [23] have adopted the two-step procedure to plot experimental FLCN

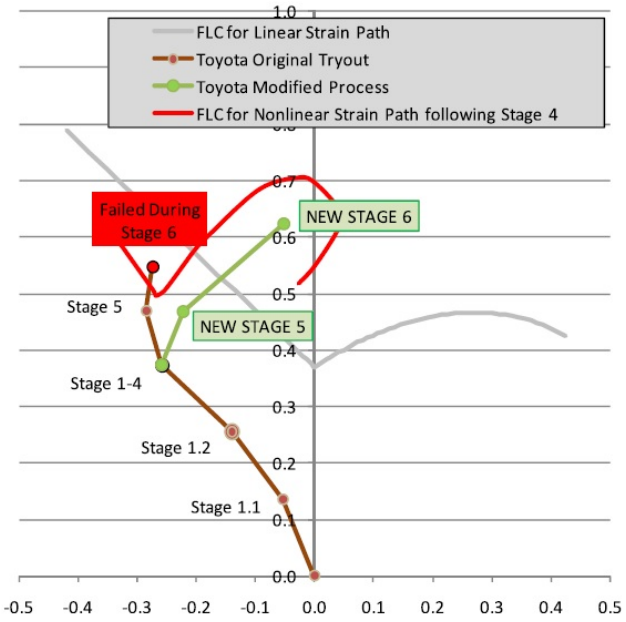

Figure 1.24: Non-linear strain path concept developed by Toyota and applied to tryout of a quarter panel stamped from a deep draw quality steel [21]

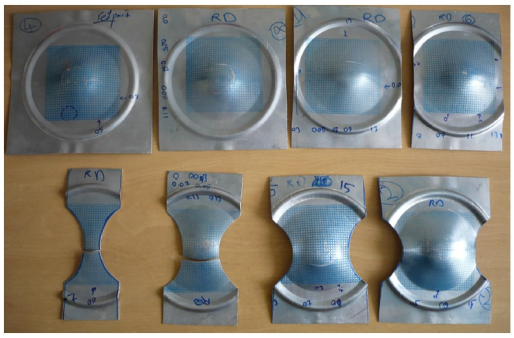

(a) The specimens after two-step tests

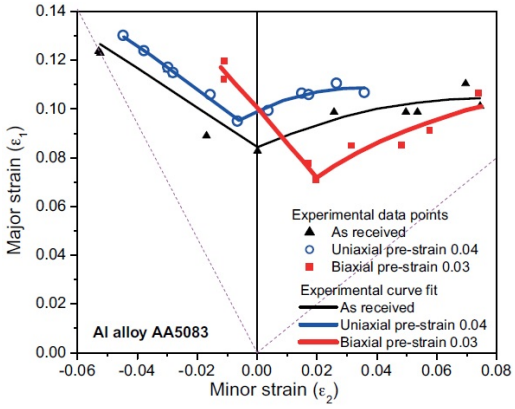

(b) The FLCNs of AA5083 sheet

Figure 1.25: Experimental identification of FLCNs of AA5083 sheet under non-linear strain paths

of a dual phase steel HC300X (t=1 mm) under different non-linear strain paths. For the first step, six prestrains are realized by oversized tensile tests (points 1 and 2) and oversized Marciniak tests (points 3-6), respectively. For the second step, the Nakajima tests are produced on the prestrain specimens. The time-dependent method is used to identify the onset of necking and the FLCNs under different non-linear strain paths are shown in Figure 1.26. It can be found that the prestrains in uniaxial tension increase the FLCN while the prestrains in biaxial stretching decrease it. The level of prestrain under same strain path has also an influence on the FLCN.

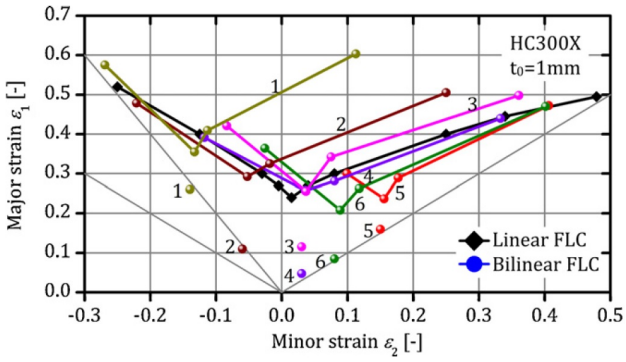

Figure 1.26: The experimental FLCN of HC300X sheet under six different prestrains

Graf and Hosford [24] have investigated the effect of strain path change on the forming limits of aluminum alloy 6111-T4 by determining the FLCN prestrained to several levels in uniaxial tension, plane-strain tension and biaxial stretching, along and perpendicular to the prior rolling direction. The results show that the abrupt changes in strain path during forming can produce significant changes in the forming limits. The prestrain in biaxial stretching decreases the formability if followed by plane-strain tension or biaxial stretching. The prestrain in uniaxial tension increases the forming limits for subsequent plane-strain tension and biaxial stretching, when the direction of principal strain is preserved but decreases them if the direction of principal strain is rotated after the prestrain. The prestrain in plane-strain tension produces a slight increase of the overall level of FLCN without the change of the direction of principal strain, but decreases it substantially with the change of the direction of principal strain.

Stoughton et al. [25] have analyzed the FLCs of 2008-T4 aluminum alloy under different prestrains reported by Graf and Hosford [26] in early years. The prestrains in biaxial, plane strain and uniaxial directions to several levels are considered. As shown in Figure 1.27, the first segment of the dashed lines represents a specific prestrain path. The vertical segment of the dashed line connects the prestrain condition with the associated FLC. Figure 1.28 (a) and (b) show the FLCs under

prestrain path of uniaxial tension along the transverse direction and the rolling direction, respectively. It is found that the direction of prestrain has an effect on the position of FLC. Moreover, the shapes of FLC under different prestrain paths are different from the shape of original FLC.

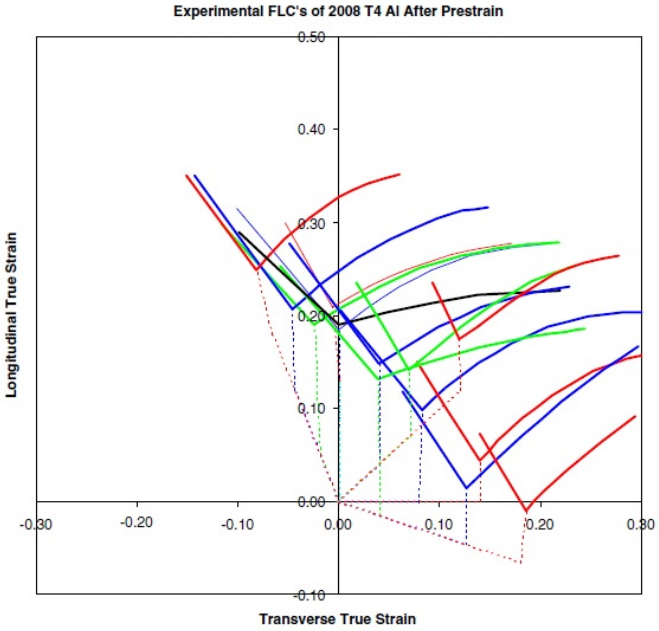

Figure 1.27: The experimental FLCs of 2008-T4 aluminum

For identifying the experimental FLCN of sheet metals under non-linear strain paths, some disadvantages can be found in the two-step procedure for controlling the strain paths. Firstly, this very time consuming procedure requires several experimental devices and the measure of the strain path is not continuous between the two steps. Secondly, the unloading between two steps is obligatory. If the loading procedure really influences the forming limits of the material, the classical two-steps procedure with unloading seems to be inappropriated. Thirdly, the dynamic control of strain path during each step is impossible. Only simplistic prestrains can be applied which makes impossible to study the formability under multiple strain path changes. In actual forming processes, curved loading path can be observed without any unloading.

The potential of the in-plane biaxial tensile test with the cruciform specimen to study the effect of strain path changes on the formability of AA5086 sheets with a one-step procedure was considered by Léotoing et al. [27]. Figure 1.29 (a) shows the forming limit points with different levels of prestrain. Different displacements from 1mm to 3 mm have been tested, corresponding respectivly to levels of prestrain from 5% to 19%. The transition from uniaxial tension to biaxial stretching corresponds to an abrupt strain path change without unloading. Figure 1.29 (b) shows the

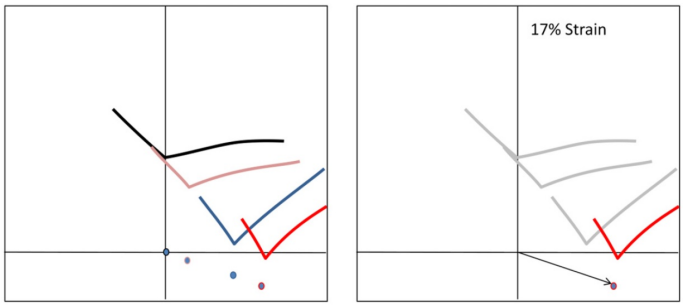

(a) Along the transverse direction

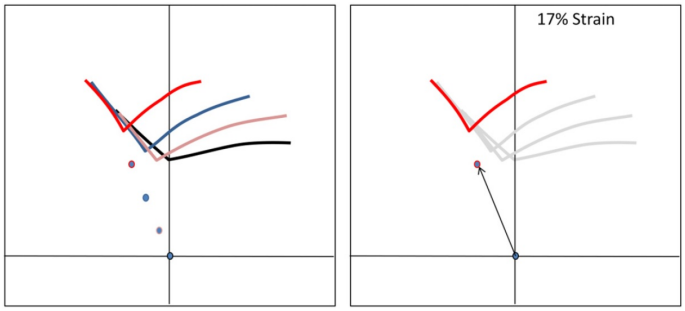

(b) Along the rolling direction

Figure 1.28: Movement of experimental strain FLC under uniaxial tensions

comparison of forming limit points under linear and non-linear strain paths. In the left-side of the FLCN, a high prestrain in uniaxial tension (close to 20%) leads to a premature failure of the specimen when it is followed by equibiaxial tension. However, in the right-side of the FLCN, a small increase of formability is observed with the prestrains from 5% to 13%.

1.3.5 Predictive model of FLCN

The experimental identification of the FLCN of sheet metal under different strain paths is a time consuming procedure and requires specific equipment. Many analytical and numerical predictions have been proposed. Prediction methods allow FLCN trends to be explored over a wide range of strain paths and provide the most efficient way for determining an optimum strain path for a sheet metal forming process [28].

Analytical predictions

Different analytical models have been developed that focus either on diffuse or localized necking. These models can help to understand the necking phenomenon and are also useful tools to predict the formability of sheet metals successfully and rapidly in industry.

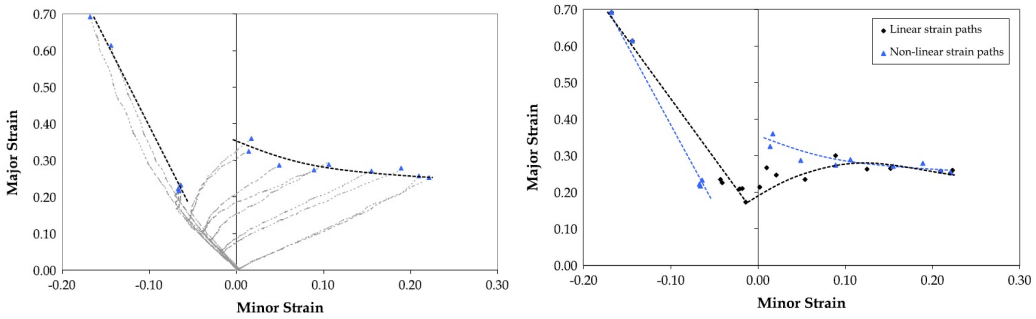

(a) FLCN under non-linear strain paths

(b) Comparison of FLCNs under linear and non-linear strain paths

Figure 1.29: FLCNs of AA5086 sheet identified by in-plane biaxial tensile test

Considère proposed the first necking criterion in 1896 by assuming that the onset of diffuse necking starts when the rate of softening first exceeds the rate of hardening in the case of uniaxial tension. Swift generalized the criterion to biaxial stretching in 1952. In industrial stampings, the maximum allowable strain is identified by localized rather than by diffuse necking. Therefore, Hill proposed a localized necking criterion based on the zero extension assumption, in which the localization band develops along the zero extension direction in the sheet metal. This prediction showed that localized necking would not occur in a uniform sheet subject to biaxial stretching, in which there is no zero extension direction. However, the practical experiences demonstrated that localized necking occurs when the sheet metal is loaded under biaxial stretching. To explain that, Marciniak and Kuczynski introduced inperfections into sheets to allow necking to occur, which is known as M-K model and used widely to predict FLCN of sheet metals [29, 30].

In addition, there are also some other models proposed by the researchers to predict the onset of necking, for example Ramaekers's criterion, Bifurcation theory, Perturbation technique, Modified maximum force criterion (MMFC) and NADDRC model [31]. The Ramaekers's criterion has been proposed to overcome the limitation of Hill's criterion that works only in the negative minor strain region. The Bifurcation theory is a concept based on the principle that localized necking is caused by the vertex/corner developed on a subsequent yield surface. For the Perturbation technique, the sheet metal is assumed to be initially homogeneous which is different from the M-K model. At any stage of the postulated homogeneous deformation process, a perturbation is superimposed on the basic homogeneous flow during deformation. Flow instability or stability is characterized by whether the perturbation is increasing or decreasing. The Modified maximum force criterion (MMFC) has been proposed to improve Swift's criterion by considering that the onset of necking

depends significantly on the strain path. The NADDRG model has been introduced by the North American Deep Drawing Research Group as an empirical equation for predicting FLCN in practice to simplify the determination of FLCN in the press workshop. The equation for calculating the forming limit strain is based on the thickness of sheet metal.

Zhang [31] has compared different analytical models. The predictive FLCNs obtained by different analytical models are presented in Figure 1.30. Some conclusions are obtained: (1) Different analytical models give varying predictions of the FLCN. (2) The forming limit strains determined by Swift's criterion are underestimated than those obtained from other criteria, especially in the left-hand side of FLCN. (3) The predictive results with M-K model depend on the initial imperfection which can be adjusted to fit experimental results. (4) The NADDGR model takes sheet thickness into account and provides an empirical equation for predicting FLCN. With increasing the thickness, the FLCN shifts upwards. This model gives a relatively high FLCN compared to other models.

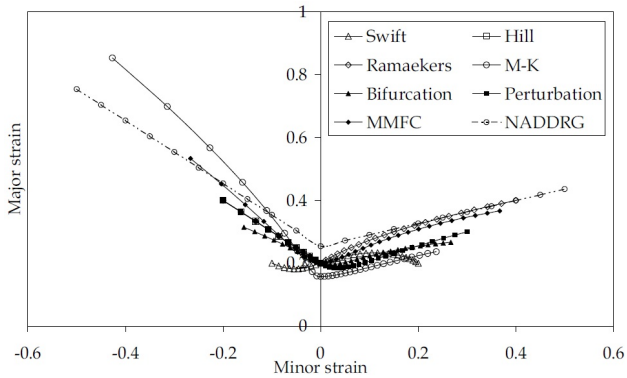

Figure 1.30: Comparison of predictive FLCNs with different analytical models [31]

Recently, Hora et al. [32] have proposed the Modified Maximum Force Criterion to perform the theoretical evaluation of FLCN. The modified maximum force criterion takes the strain rate transformation in diffuse necking into account and improves remarkably the theoretical evaluation of FLCN. Experiments verified this model and showed satisfactory agreement between the calculated FLCN and the experimental data. Furthermore, the simplified formulations can provide explicit judgement directly from the simulation results and are very easily implemented into the finite element code.

Numerical prediction

The numerical prediction of FLCN becomes more attractive due to computational facilities. In the numerical prediction of FLCN, there are two main categories: Finite

element analysis with M-K model and simulation of conventional tests.

Zhang et al. [33] have investigated the formability of AA5086 sheet under linear strain paths by combining the tensile test with the finite element M-K model. The quasi-static tensile test is conducted to identify an appropriate constitutive law and calibrate the initial imperfection factor in the M-K model. As shown in Figure 1.31, compared with the M-K model, the strain states with experimental procedure are located in a narrow range, especially at the left-hand side. The levels of the numerical and experimental FLCNs are almost the same. It can be concluded that the numerical method gives a reasonable prediction of FLCN.

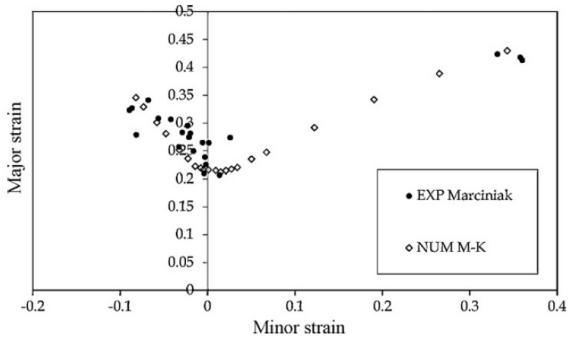

Figure 1.31: Comparison of numerical and experimental FLCNs of AA5086 sheet

Léotoing et al. [11] have used the cruciform specimen to identify the numerical FLCN of AA5086 sheet (4mm). The comparison between experimental and numerical FLCNs for Ludwick's law with Hill48 and Mises criterion is shown in Figure 1.32. The correlation between experimental and numerical results is very good for the right-hand side of the FLCN, especially for the Hill48 criterion. It is concluded that taking an anisotropic yield criterion into consideration improves considerably the accuracy of numerical predictions.

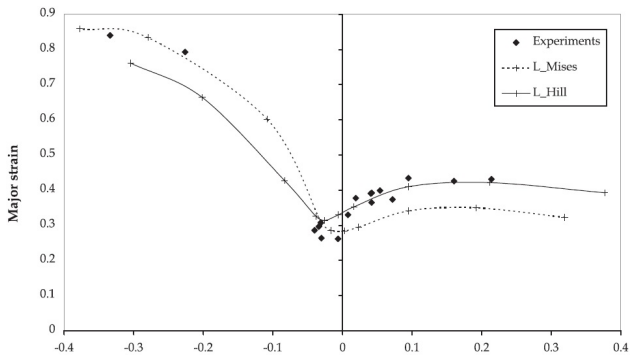

Figure 1.32: Comparison between experimental results and numerical FLCNs [11]

In the literature, most of the studies for prediction of FLCN under non-linear strain paths are investigated by using M-K model. Graf and Hosford [34] have

analyzed the effect of changing the strain paths on an aluminum alloy 2008-T4 by using the M-K model. Calculations incorporating abrupt path changes agreed with the general trends found experimentally. The results show that if the first step corresponds to biaxial stretching, the FLCN shifts to the right and down with respect to the original FLCN, whereas it shifts to the left and up when the first step is uniaxial tension. Kuroda and Tvergaard [35] have analyzed the effect of non-proportional strain paths prior to the occurence of flow localization on the FLCN by using the M-K model. The predicted FLCN shows strong dependence on whether or not the load on the sheet is removed between two loads on a non-proportional strain path.

1.3.6 Forming limit stress curve

The stress-based forming limit concept was proposed in the early 1980s [36]. It is found that the forming limit stress curve (FLSC) is almost path-independent. If path-independence of the FLSC can be established, then the limits to formability will be predicted accurately using a combination of the FLSC and finite element simulation, not only for proportional loading but also in cases where a sheet element has a complex strain history [9].

Many authors [37, 38, 39] have investigated the FLSC even if a stress state can not be measured experimentally. The FLSC is calculated from the measured forming limit strains using postulated constitutive assumptions, i.e. yield function and hardening rule. Yoshida et al. [9] have investigated the effect of changing strain paths on the forming limit stresses of sheet metals by using the M-K model. Two types of combined loading are considered: one type includes unloading between the first and the second steps of loadings while the other type does not include unloading. The results show that the forming limit curves in stress space depend on the strain path for the second type of combined loading.

Furthermore, an accurate yield function and hardening rule must be considered in the FE simulation for calculating stresses.

1.4 Identification of sheet metal formability based on FLCF

Under strain path near balanced biaxial stretching or for some specific circumstances (e.g. stretched parts with complex geometries and high strain gradients in SPIF [40]), ductile fracture can be induced without onset of localized necking. Besides, in case of materials with low ductility, fracture often occurs without any obvious

necking phenomenon [41, 42]. In that case, the forming limit strains controlled by fracture rather than by necking characterize the formability of sheet metals. For describing the forming limits at fracture under different strain paths, the traditional FLCN is inapplicable and the FLCF (see Figure 1.6) should be employed [43].

In this section, a review of experimental identification of FLCF is performed firstly. Then, different ductile fracture criteria defined in previous studies for predicting the onset of fracture are introduced. Lastly, a review of predictive identification of FLCF based on the commonly used ductile fracture criteria is presented.

1.4.1 Experimental identification of FLCF

Isik et al. [5] have used several conventional tests (Tensile test, Circular bulge test, Elliptical bulge test, Nakazima test and Hemispherical dome test) to produce different strain paths to construct the FLCF of AA1050-H111 sheet. As shown in Figure 1.33, the forming limit strains at fracture can be fitted by a straight line. Furthermore, the FLCF has been also determined by the SPIF with the truncated conical and pyramidal parts, as shown in Figure 1.34. The forming limit strains at fracture produced by SPIF can also be fitted by a line which is in excellent agreement with the previous estimated FLCF from conventional tests.

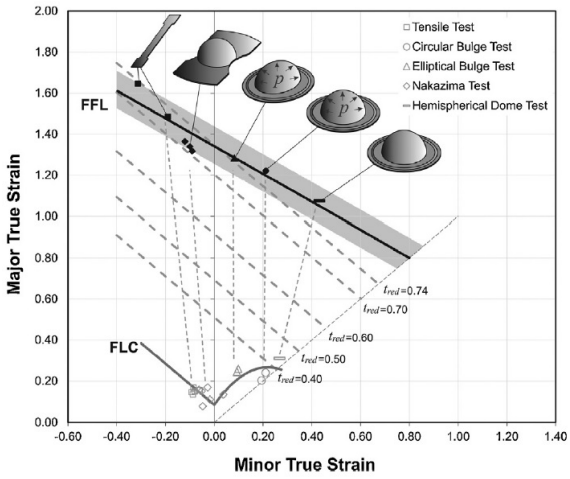

Figure 1.33: Forming limits of AA1050-H111 sheet constructed by traditional tests [5]

Based on the same experiments, Martins et al. [44] have plotted the FLCF of AISI 304L stainless steel sheet with 0.5 mm thickness. As shown in Figure 1.35, the open markers refer to the experimental forming limit strains at necking and the solid markers refer to the experimental forming limit strains at fracture. As observed for the AA1050 sheet, a straight line can also be used to fit the experimental limit strains at fracture of the AISI 304L stainless steel sheet.

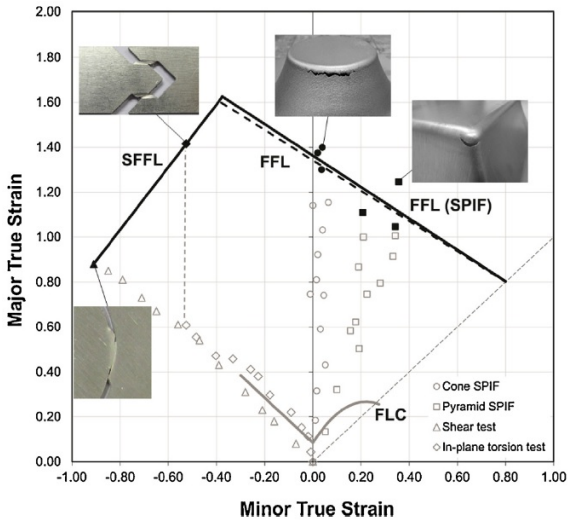

Figure 1.34: Forming limits of AA1050-H111 sheet constructed by SPIF and shear test [5]

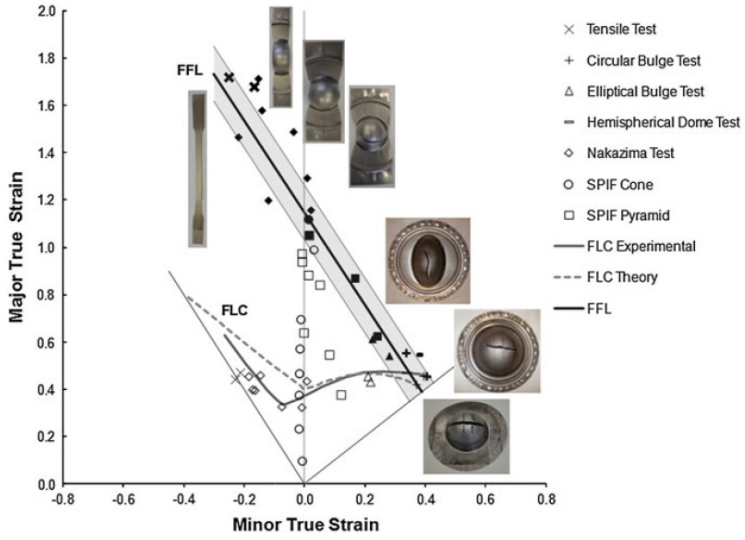

Figure 1.35: Forming limits of AISI 304L stainless steel sheet constructed by several formability tests [44]

Gorji et al. [45] have used the Nakazima test to determine the FLCF of AA6016 sheet. Different strain paths are produced by various widths of specimen (from 20 mm to 200 mm). The DIC method and the thinning method are used to measure the critical fracture strain. For the DIC method, the last detected values before rupture are considered as the fracture strains. For the thinning method, the measurement of strain considers the fracture thickness. Figure 1.36 shows the comparison of forming limit strains at fracture under different strain paths produced by the two methods of strain measurement. As observed, the forming limit strains at fracture estimated by thinning method are higher than those obtained by the DIC method.

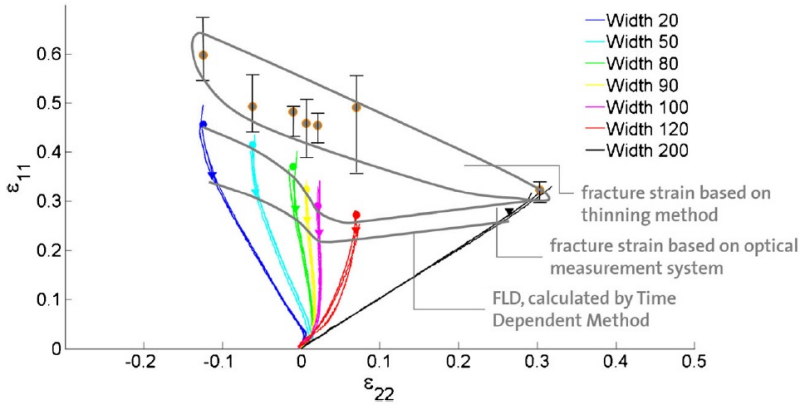

Figure 1.36: Comparison of the fracture strains of AA6016 sheet estimated by different methods [45]

Recently, a biaxial tensile testing machine with the cruciform specimen was proposed by Xiao et al. [46] for high temperature testing. This method was used to evaluate the thermal limit strains at fracture of a TA1 titanium alloy at different temperatures (20°C, 400°C and 600°C) [47]. As shown in Figure 1.37, the forming limit strains along the rolling direction are on the horizontal coordinate, whereas those along the transverse direction are on the vertical coordinate. In this figure, β=1, β=-0.5 and β=-2 indicate the equibiaxial stretching, uniaxial tension along the transverse direction and uniaxial tension along the rolling direction, respectively.

The above-mentioned traditional experimental methods for obtaining the FLCF of sheet metal require many formability tests and various shapes of specimen to produce different strain paths from equiabiaxial stretching to uniaxial tension. Using the in-plane biaxial tensile test with a cruciform specimen to determine the FLCF is an interesting alternative to overcome the drawbacks of traditional methods. Two advantages can be concluded: (1) The in-plane biaxial tensile test with a cruciform specimen is frictionless, without influence of bending; (2) The strain path during the test can be directly controlled by the motion of four independent actuators, which is sufficient to cover the whole FLCF with just one shape of cruciform specimen,

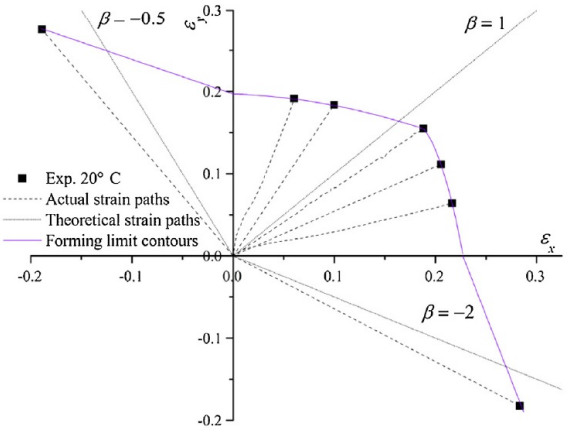

Figure 1.37: FLCF of TA1 titanium alloy sheet [47]

under linear strain paths [12, 11] and non-linear strain paths without any unloading [27].

1.4.2 Ductile fracture criteria

Failure in metalworking usually occurs as ductile fracture, rarely as brittle fracture [48]. Physical observation and micromechanical analysis have led to the development of a number of phenomenological or micro/meso-mechanical motivated ductile fracture criteria. These criteria are classified into coupled (which incorporate damage accumulation into the constitutive equations) and uncoupled (which neglect the effects of damage on the yield surface of materials) approaches [49]. The coupled ductile fracture criteria are based on micro-based damage mechanics built upon the macroscopic yield surface for porous materials [50] or based on continuum damage mechanics [51]. The uncoupled ductile fracture criteria are formulated empirically or semi-empirically by a general function g in terms of macroscopic variables such as the equivalent plastic strain $\bar{\varepsilon}_p$, equivalent stress $\bar{\sigma}$ or hydrostatic pressure σ_h, that are most relevant to fracture initiation and propagation. Such criteria are expressed as follows [52]:

$$\int_0^{\bar{\varepsilon}_g} g(\bar{\varepsilon}_p, \bar{\sigma}, \sigma_h) d\bar{\varepsilon}_p = C \tag{1.18}$$

where $\bar{\varepsilon}_g$ and C are the equivalent strain and the critical values at fracture. The fracture is assumed to occur when the internal damage reaches a critical value, which results in a sudden loss of load capability of the structure [53, 54].

In order to predict the FLCF, five existing ductile fracture criteria from literatures are briefly presented hereafter: Cockroft and Latham, Brozzo, Ayada, Rice and Tracey, Oyane.

The classical Cockroft and Latham criterion [55] is a phenomenological model in which the critical value C_1 at fracture depends on the maximum principal stress σ_{max}.

$$\int_0^{\bar{\varepsilon}_g} \frac{\sigma_{max}}{\bar{\sigma}}\, d\bar{\varepsilon}_p = C_1 \tag{1.19}$$

The Cockroft and Latham criterion was modified by Brozzo et al. [56] and the effect of hydrostatic stress σ_h in an explicit form was introduced as follows:

$$\int_0^{\bar{\varepsilon}_g} \frac{2}{3}(1 - \frac{\sigma_h}{\sigma_{max}})^{-1}\, d\bar{\varepsilon}_p = C_2 \tag{1.20}$$

The fundamentals of Ayada criterion are based on the work of McClintock [57], in which a relation between the inter-hole spacing, the diameter of the hole (particle/inclusion) and stress triaxiality at the onset of fracture under tension loading is established. This criterion includes the effect of hydrostatic stress and has proved its efficiency for some forming operations [58].

$$\int_0^{\bar{\varepsilon}_g} \frac{\sigma_h}{\bar{\sigma}}\, d\bar{\varepsilon}_p = C_3 \tag{1.21}$$

The Rice and Tracey criterion [59], established from void growth observations is expressed by:

$$\int_0^{\bar{\varepsilon}_g} exp\,(\frac{3}{2}\frac{\sigma_h}{\bar{\sigma}})\, d\bar{\varepsilon}_p = C_4 \tag{1.22}$$

The Oyane criterion [60] is derived from the equations of plasticity theory for porous materials as follows:

$$\int_0^{\bar{\varepsilon}_g} (1 + \frac{\sigma_h}{C_{5a}\bar{\sigma}})\, d\bar{\varepsilon}_p = C_{5b} \tag{1.23}$$

One can noted that two parameters need to be identified for this last criterion.

1.4.3 Predictive FLCF

Various ductile fracture criteria have been proposed to predict both the fracture initiation sites and the forming limits at fracture.

Four ductile fracture criteria (Cockcroft and Latham, Brozzo, Oyane criteria) are compared by Takuda et al. [61] to predict the forming limits for the axisymmetric deep drawing of various aluminium alloy sheets (A1100, A2024 and A5052) and mild steel sheet (SPCC). Takuda et al. [62] have also applied the Oyane ductile fracture criterion in the deep drawing processes of laminates composed of mild steel (SPCC)

and various aluminium alloy sheets (A1100, A2024 and A5052). The forming limits due to various types of fractures of the laminated composite sheets are successfully predicted. Takuda et al. [63] also introduced the Oyane ductile fracture criterion into the finite element similation to predict the initiation of fracture in the axisymmetric bore-expanding process. Calculations are carried out for mild steel and high strength steel sheets, using flat-, hemispherical- and conical-headed punches. As shown in Figure 1.38, the comparison with the experimental results shows that the forming limits due to various types of fracture initiations in the bore-expanding processes are successfully predicted.

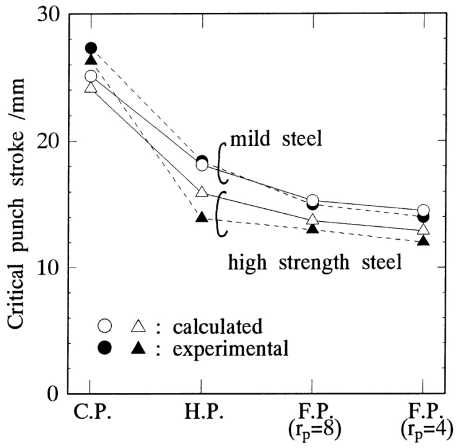

Figure 1.38: Comparison between calculated and experimental results [63]

Clift et al. [64] have reviewed commonly used ductile fracture criteria (Cockroft and Latham, Brozzo, Oyane criteria) to predict fracture initiation in a range of simple metal forming operations. Three types of metal forming operation are considered: simple upsetting, axisymmetric extrusion, and strip compression and tension, allowing to examine the fracture initiation under different loading conditions.

Mishra et al. [58] have investigated the characterization and numerical prediction of the onset of rupture in bending of DP980 steel sheet. Four fracture criteria (Cockcroft and Latham, Brozzo, Ayada, Rice and Tracey criteria) are used to predict the onset of fracture. The critical values are identified by uniaxial tensile test. The critical bending tool displacement and limit strain are well predicted by using Ayada criterion.

The above-mentioned ductile fracture criteria have not only been used for prediction of fracture initiation sites and forming limits at fracture, but also have been used to predict the FLCFs of sheet metals in numerical simulation.

Ozturk et al. [65] have used several criteria (Cockroft and Latham, Brozzo and et al. criteria) to predict the FLCF for the aluminum killed drawing quality electrogalvanized (AKDQ) steel sheets. Different sample geometries and lubrication

conditions are used to generate all possible strain paths in the Nakajima test. The prediction results for the left side of the FLCF are quite successful, but not acceptable for the right side. It is concluded that these criteria could not be directly used to determine the FLCF alone and further modifications are needed.

Takuda et al. [42] has used the Oyane ductile fracture criterion to predict the FLCF for biaxial stretching of aluminium alloy sheets with the finite element simulation. Material constants for the criterion are obtained from the fracture strains measured in the biaxial stretching tests. Various strain paths from uniaxial tension to balanced biaxial stretching are considered. The results show that the FLCF of A1100 sheet is found to be approximately linear and can be successfully predicted by the approach. However, the FLCF of AA6111 measured by Jain et al. [66] has a rather complex shape approaching the FLCN towards the equibiaxial strain path. The various ductile fracture criteria with the integral form could not completely predict the shape of the experimental FCLF, while the maximum shear stress criterion by Tresca predicts reasonably well the fracture limits for a range of strain ratios, as shown in Figure 1.39.

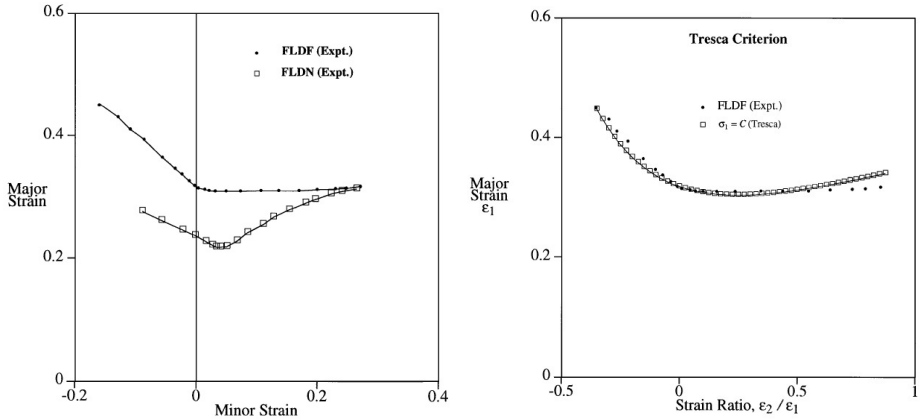

(a) Experimentally determined FLCN and FLCF

(b) Experimental and predictive results by Tresca criterion

Figure 1.39: Forming limit strains and prediction results with Tresca Criterion

Xiao et al. [47] have used the Oyane ductile criterion to predict the forming limit strains at fracture for titanium alloys. The experimental results obtained from the biaxial tensile test with a cruciform specimen are in good agreement with the predicted values obtained from the finite element analysis with the Oyane criterion.

Some conclusions can be obtained from the previous predictions of fracture: (1) The ductile fracture criteria are efficient for predicting the onset of fracture and FLCFs of sheet metals under different strain paths; (2) There is no universal ductile fracture criterion to predict all types of material; (3) It could be interesting to use

the ductile fracture criteria to predict the FLCF of sheet metal when a change of strain path during the forming process is adopted.

1.5 Identification of sheet metal formability based on fracture locus

The stress triaxiality is an important parameter for controlling the fracture. The fracture locus in strain and stress space is also a method to describe the forming limits at fracture. In this section, the stress triaxiality is introduced and previous investigations of fracture locus are discussed.

1.5.1 Stress triaxiality

In order to quantify the influence of stress state on fracture strain, the stress state of the isotropic material is geometrically characterized by the three-dimensional principal stress (σ_1, σ_2, σ_3). The Lode coordinates can be defined from the scaled version of three stress invariants (p, q, r):

$$p = -\sigma_m = -\frac{1}{3}I_1 = -\frac{1}{3}(\sigma_1 + \sigma_2 + \sigma_3) \tag{1.24}$$

$$q = \bar{\sigma} = \sqrt{3J_2} = \sqrt{\frac{1}{2}[(\sigma_1 - \sigma_2)^2 + (\sigma_2 - \sigma_3)^2] + (\sigma_3 - \sigma_1)^2} \tag{1.25}$$

$$r = (\frac{27}{2}J_3)^{\frac{1}{3}} = [\frac{27}{2}(\sigma_1 - \sigma_m)(\sigma_2 - \sigma_m)(\sigma_3 - \sigma_m)]^{\frac{1}{3}} \tag{1.26}$$

σ_m and $\bar{\sigma}$ are the hydrostatic stress and equivalent stress, I_1 is the first invariant of the stress tensor, while J_2 and J_3 are the second and third invariants of deviatoric stress.

The stress triaxiality η is defined by:

$$\eta = \frac{-p}{q} = \frac{\sigma_m}{\bar{\sigma}} \tag{1.27}$$

Figure 1.40 shows different damage mechanisms depending on stress triaxiality. Under tension dominated stress conditions (high positive stress triaxialities), damage in ductile metals is mainly caused by nucleation, growth and coalescence of voids. Under shear and compression dominated stress states (small positive or negative stress triaxialities), evolution of micro-shear-cracks is the predominant damage mechanism. Furthermore, combination of both basic mechanisms occurs for moderate positive stress triaxialities. [67].

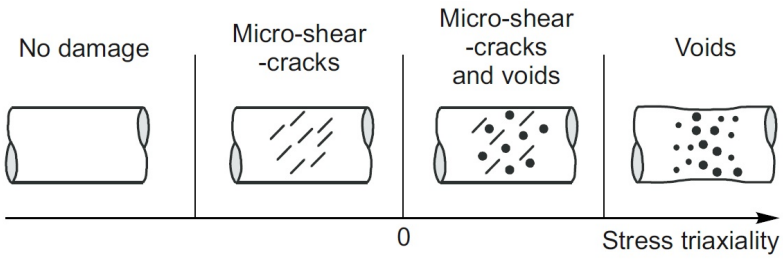

Figure 1.40: Different damage mechanisms depending on value of stress triaxiality

1.5.2 Investigation of fracture locus

Bao et al. [68] have investigated the fracture locus based on the equivalent strain and stress triaxiality for 2024-T351 aluminum alloy. A series of tests including upsetting tests (Figure 1.41), shear tests (Figure 1.42), combined shear and tension tests (Figure 1.43) and tensile tests (Figure 1.44) with different shapes of specimens are used to produce a wide range of stress triaxiality. Numerical simulations of all the tests are performed by using ABAQUS for obtaining individual components of stress and strain tensors at fracture location. The results show that fracture ductility is strongly dependent on the stress triaxiality. Figure 1.45 shows equivalent strain to fracture in function of the average stress triaxiality.

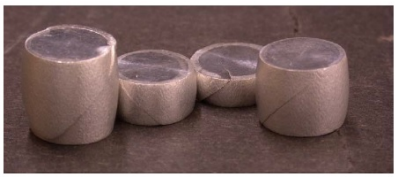

Figure 1.41: Deformed specimens with different ratio of diameter and height (η= -0.33 to -0.05) [68]

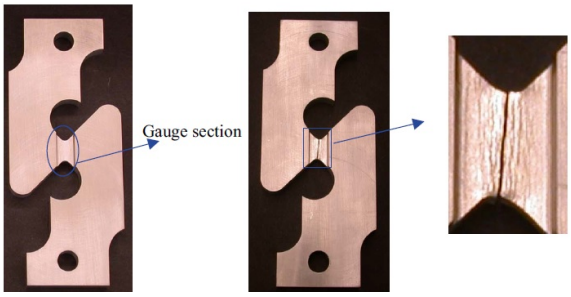

Figure 1.42: Pure shear tests (η= 0 to 0.02) [68]

To better understand the in-service mechanical behavior of advanced high-strength steels, Anderson et al. [69] have investigated the effect of stress triaxiality and strain

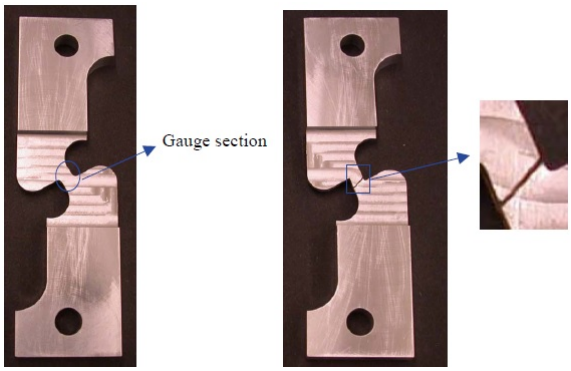

Figure 1.43: Combined shear and tension test (η= 0.04 to 0.15) [68]

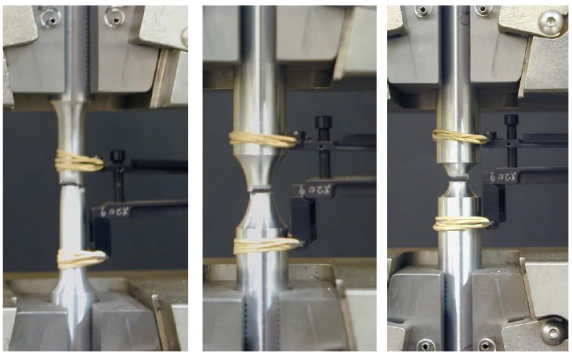

Figure 1.44: Fracture tensile specimes with different geometries (η= 0.33 to 1) [68]

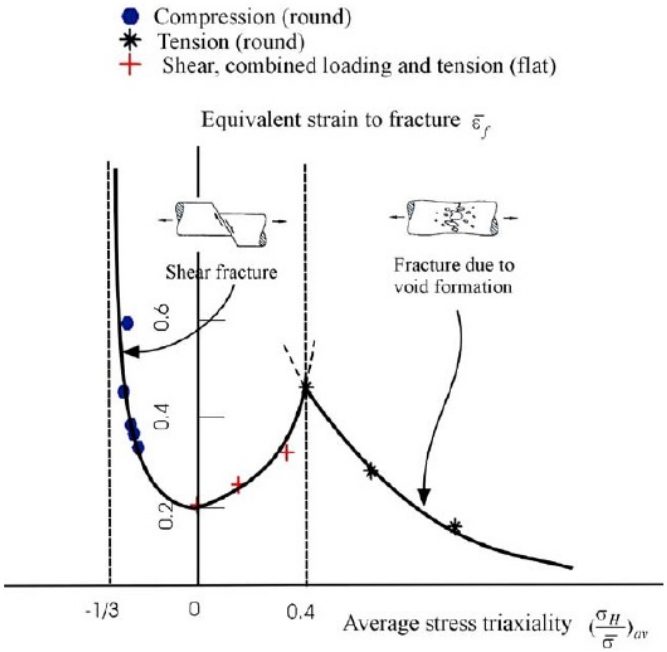

Figure 1.45: Dependence of the equivalent strain to fracture on the stress triaxiality [68]

rate on the failure behavior of the dual-phase DP780 steel. Three flat, notched mini-tensile geometries with varying notch severities and initial stress triaxialities of 0.36, 0.45 and 0.74 were considered in the experiments. The strain rates of 0.001, 0.01, 0.1, 1, 10 and $100s^{-1}$ for all three notched geometries were considered in the tensile tests. The results show that the DP780 steel is sensitive to both strain rate and initial triaxiality for the range of conditions tested.

Li et al. [70] have investigated the effect of stress triaxiality η on the fracture mechanism and ductility of Chinese Q460 high strength structural steel. Four types of notched specimens are adopted and corresponding numerical simulations are conducted. The results show that different fracture mechanisms are observed in different stress triaxialities.

Previous experiments with un-notched and differently notched flat specimens covered stress triaxialities η between 0.33 and 0.6 which is only a small region in the positive range of stress triaxiality. Larger values of stress triaxiality can be obtained in the tension tests with cylindrical specimens (see Figure 1.44)). However, it is impossible to manufacture the cylindrical specimen when the behavior of thin sheets is investigated. Therefore, it is necessary to develop new series of experiments with different geometries of flat specimens to analyze the effect of stress states over a wide range.

Motivated by the above reason, Brünig et al. [71] have proposed a flat cruciform specimen to produce a wide range of stress triaxialities. Figure 1.46 shows the finite element mesh of the cruciform specimen. In the center of the specimen a notch in thickness direction has been milled leading here to high stresses and localization of inelastic deformations. Figure 1.47 shows stress triaxialities covered by different geometries of flat specimens which are uniaxially or biaxially loaded. The proposed cruciform specimen is able to cover a much larger range of stress states in the shear and tension regime as well as respective combinations. Brünig et al. [72] also used this cruciform specimen to discuss a phenomenological continuum model taking into account the effect of stress state on damage and fracture mechanisms.

Rencently, Gerke et al. [67] have designed different cruciform specimens (Figure 1.48) to study the effect of damage and fracture processes under different biaxial loadings for sheet metals. The Square-specimen (Figure 1.48 (a)) is valuable to study the onset of plastic deformations but not the damage and failure behavior at more elevant strain levels. The X1-specimen and X2-specimen (Figure 1.48 (b) and (c)) have two crosswise arranged notches, while at the XO1-specimen and XO2-specimen (Figure 1.48 (d) and (e)) a central hole is added by what four separated notched regions occur. The notches have been arranged parallel to one of the loading axis for the H-speicmen (Figure 1.48 (f)). Biaxial tensile experiments with these

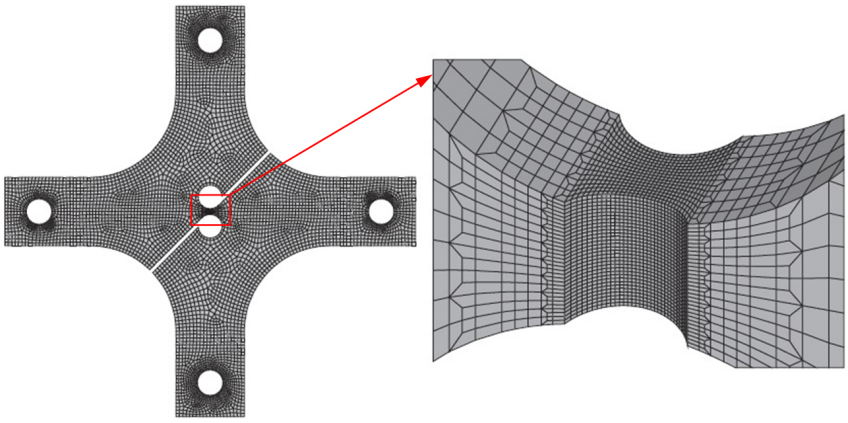

Figure 1.46: Finite element mesh of the cruciform specimen [71]

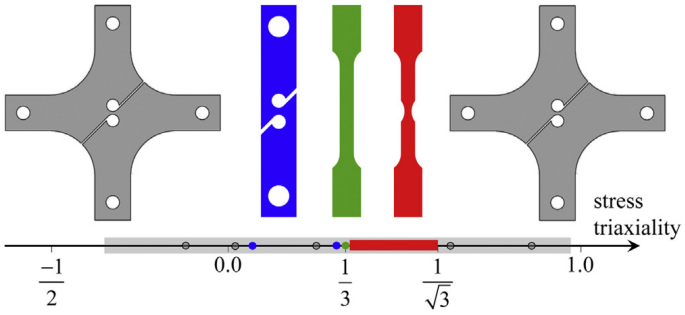

Figure 1.47: Stress triaxialities covered by different specimens [71]

cruciform specimens taken from sheet metals are performed. The results show that the XO2-specimen and H-specimen (Figure 1.49) can produce a wide range of stress triaxiality.

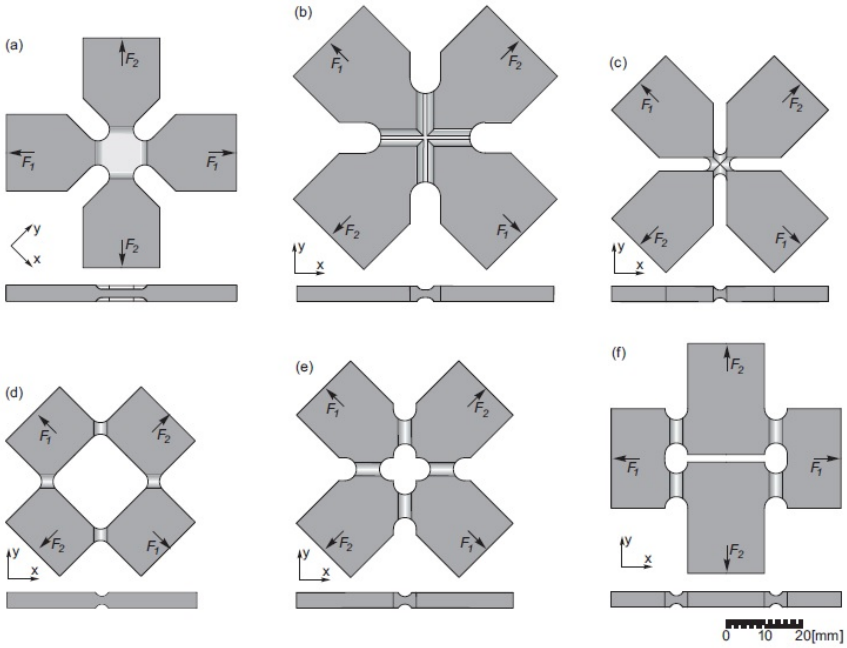

Figure 1.48: Different cruciform specimens designed by Gerke et al.: (a) Square-, (b) X1-, (c) X2-, (d) XO1-, (e) XO2-, (f) H-specimen [67]

However, it can be concluded that those cruciform specimens are special for investigating the fracture locus in equivalent strain and stress triaxiality space. It is hard to obtain the FLCN and FLCF with just one shape of those cruciform specimens.

1.6 Conclusion

For identifying the FLCN and FLCF under linear strain paths, conventional methods require various geometrical specifications to produce different linear strain paths from equibiaxial stretching to uniaxial tension through plane-strain tension. In addition, the effect of friction between the forming tool and the sheet is difficult to evaluate. For identifying the FLCN and FLCF under non-linear strain paths, there are also some disadvantages in the conventional two-step procedure for controlling the strain paths. Firstly, this very time consuming procedure requires several experimental devices and the measure of the strain path is not continuous between the two steps. Secondly, the unloading between two steps is obligatory. Thirdly, the dynamic control of strain path during each step is impossible. Only simplistic

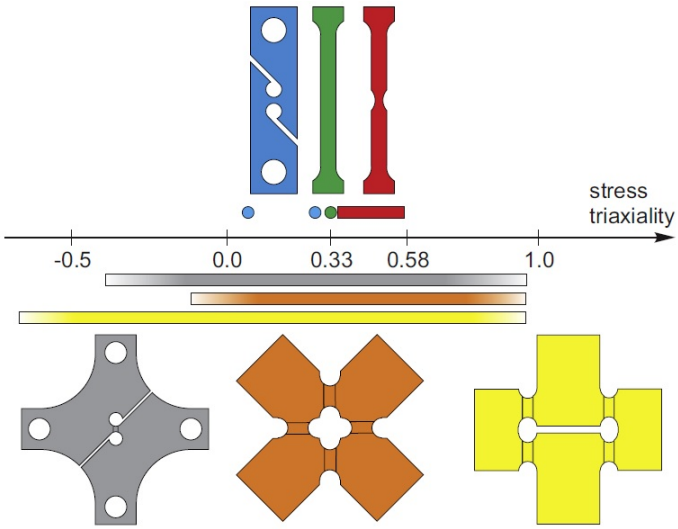

Figure 1.49: Stress triaxiality range of different specimens [67]

prestrains can be applied which makes impossible to study the formability under multiple strain path changes. In actual forming processes, curved loading path can be observed without any unloading.

Using the in-plane biaxial tensile test with the cruciform specimen to identify the FLCN and FLCF under linear and non-linear strain paths could be an interesting alternative to overcome the drawbacks of conventional methods. The in-plane biaxial tensile test with the cruciform specimen is frictionless, without influence of bending. Furthermore, the strain path during the test can be directly controlled by the motion of four independent actuators, which is sufficient to cover the whole forming limit diagram under linear and non-linear strain paths, just with one shape of cruciform specimen.

The ductile fracture criteria are efficient for predicting the onset of fracture and FLCFs of sheet metals under different strain paths. However, there is no universal ductile fracture criterion to predict all types of material.

The aim of this study is twofold. The first objective is to show that the in-plane biaxial tensile test associated with a single type of cruciform specimen permits to investigate the forming limit strains at necking and fracture of sheet metals under a wide range of strain path including linear and non-linear strain paths. The second objective is to discuss the validity of commonly used classical ductile fracture criteria to predict the onset of fracture for sheet metal by means of a finite element simulation of the in-plane biaxial tensile test.

Chapter 2

Identification of forming limits of AA5086 sheet with an existed shape of cruciform specimen

Résumé

Dans ce chapitre, le dispositif expérimental d'essai de traction biaxiale, la forme d'éprouvette cruciforme utilisée ainsi que la méthode de calcul par corrélation d'images des déformations de surface de l'éprouvette sont tout d'abord présentés. Une méthode temporelle basée sur l'évolution de la déformation majeure et l'observation de l'image macroscopique de la surface de l'éprouvette est ensuite proposée pour identifier le début de la rupture et déterminer ainsi les déformations limites à rupture.

Par application de la méthode ainsi proposée, les CLFRs d'une tôle d'aluminium (AA5086) de 4mm d'épaisseur sont déterminées pour des chemins linéaires et non-linéaires. Pour cette campagne expérimentale, une forme d'éprouvette cruciforme déjà validée pour la détermination de la CLFS de ce même matériau, est utilisée. Une comparaison de déformations limites à striction et à rupture pour cet alliage d'aluminium est ainsi discutée.

Pour des chemins de déformation linéaires, les déformations expérimentales limites à rupture peuvent être approximées par une droite. Ces résultats expérimentaux sont prédits correctement par le critère de rupture ductile d'Ayada calibré à l'aide des déformations limites expérimentales à rupture obtenues pour un chemin de déformation de traction équibiaxiale.

Pour les chemins non-linéaires testés, une pré-déformation en traction uniaxiale allant de 5% à 19% est tout d'abord appliquée avant une phase de traction equibiaxiale, sans déchargement entre les deux phases. Jusqu'à une pré-déformation de 13%, on peut considérer que le changement de chemin n'a pas d'influence notable sur les déformations limites à rupture. Pour des pré-déformations supérieures, la localisation de la déformation apparue pendant la phase de pré-déformation conduit à une rupture prématurée peu après le changement de chemin.

2.1 Introduction

In this chapter, the in-plane biaxial tensile testing device is introduced firstly in Section 2.2. Then, a method for identifying onset of fracture is proposed in Section 2.3. A dedicated cruciform specimen is used to identify the experimental and numerical FLCFs of AA5086 sheet with an original thickness of 4 mm under linear and non-linear strain paths from Section 2.4 to Section 2.7. Lastly, this cruciform specimen is used to identify the fracture locus in equivalent strain and stress triaxiality space in Section 2.8.

2.2 In-plane biaxial tensile testing device

2.2.1 In-plane biaxial tensile testing machine

As shown in Figure 2.1, a dynamic in-plane biaxial tensile testing machine was proposed by the laboratory LGCGM of INSA-Rennes. Four independent servohydraulic actuators are used and the loading capacity of each actuator is 50 kN. For quasi-static biaxial tensile tests, the machine is controlled by close-loop with displacement sensors. For dynamic biaxial tensile tests, the machine is controlled by open-loop and the loading speed can reach 2 m/s. An additional mass of 100 kg is adopted on each actuator to maintain loading speed by inertia effect. A camera is used to capture the consecutive images at the specimen surface.

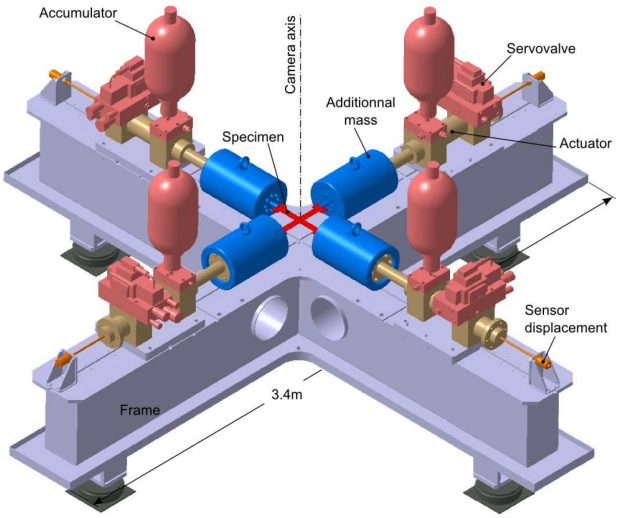

Figure 2.1: In-plane biaxial tensile testing machine

As shown in Figure 2.2, a dedicated cruciform specimen for obtaining large strains in the center of specimen was proposed by the laboratory to plot FLCN

[12]. This geometry permits a direct control of the strain path in the fracture zone (center of specimen) thanks to the control of the displacements of four independent actuators acting on the four arms of the specimen. For this specimen, two steps of thickness reduction are adopted in the central region. The first thickness reduction is a circle with an arc profile in the sheet thickness. The second thickness reduction is a square with edges parallelled to the arms. Four slots are added in each arm to reduce their transverse rigidity and eliminate geometric constraints.

The 5xxx series of aluminium alloys are used due to the high-strength to weight ratio, corrosion resistance, good workability and weldability characteristics. AA5086 sheet is a type of the 5xxx series and is widely used in automotive, aircraft and naval industries [18]. All the cruciform specimens are made from AA5086H111 sheet blanks with a 4 mm initial thickness. The central region of the specimen is manufactured by using a digital numerical turning-lathe, with a precision of 0.02 mm for the central thickness. The effect of machining process on the determination of the forming limit strains at necking was evaluated and it was shown that this effect was included in the intrinsic scattering [73]. Different strain paths (from uniaxial tension to equibiaxial stretching through plane-strain tension) are tested by means of a velocity of $1mm/s$ for one axis (rolling direction of the sheet), and a velocity varying from free to $1mm/s$ for the other one.

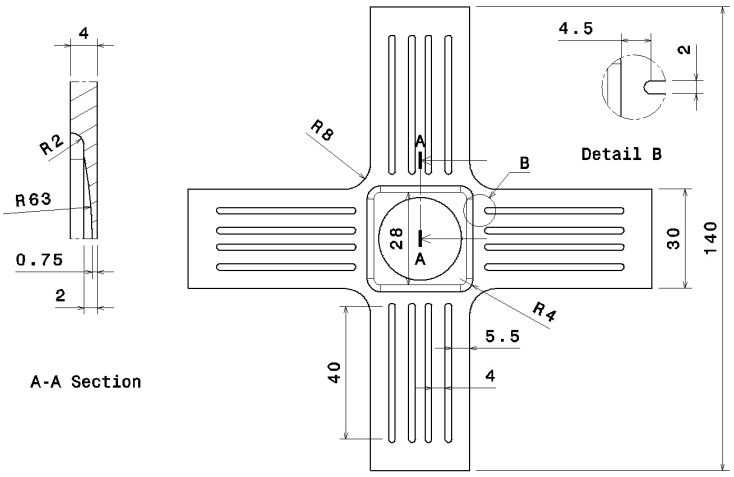

Figure 2.2: Geometry of the proposed cruciform specimen [12]

2.2.2 Strain measurement

Digital Image Correlation (DIC) technique is one of the current most used optical technologies for deformation measurement in the field of experimental mechanics [74]. In this without contact technique, a camera is used to capture images of

specimen surface. The strain measurement by DIC can be divided into three steps: (1) pre-treatment: generation of speckle pattern on specimen surface, (2) image recording by camera during the test, (3) post-treatment: displacement and strain calculation.

Generation of speckle pattern on specimen surface

Figure.2.3 shows the speckle pattern, which is obtained by a white background followed by a spray of black points on the surface of the cruciform specimen. The pattern adheres to the surface and deforms with it.

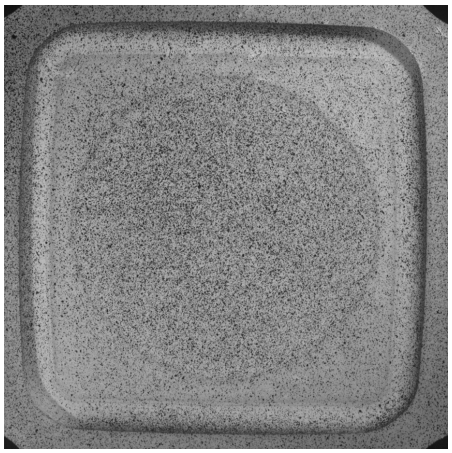

Figure 2.3: Speckle pattern on the surface of the cruciform specimen

Image record by camera

A high-speed camera (Fastcam ultima APX-RS digital CMOS camera) associated with a macro lens is used to capture the consecutive images and an acquisition of 250 images/s is adopted. The digital imaging program CORRELA2006, developed by the LMS at University of Poitiers, is employed to evaluate the surface strains of the specimen.

Displacement and strain calculation

After the test, based on image recording, the DIC technique calculates the full-field surface displacements by matching the subsets in the grayscale digital images of the specimen surface before and after deformation. As shown in Figure 2.4, some subsets are chosen and used to determine its corresponding location in the deformed image. To evaluate the similarity degree between the reference subset and the deformed subset, a cross-correlation (CC) criterion or sum-squared difference (SSD) correlation criterion must be predefined. The matching procedure is completed through

searching the peak position of the distribution of correlation coefficient. Once the correlation coefficient extremum is detected, the position of the deformed subset is determined. The differences in the position of the reference subset center and the target subset center yield the in-plane displacement vector [75].

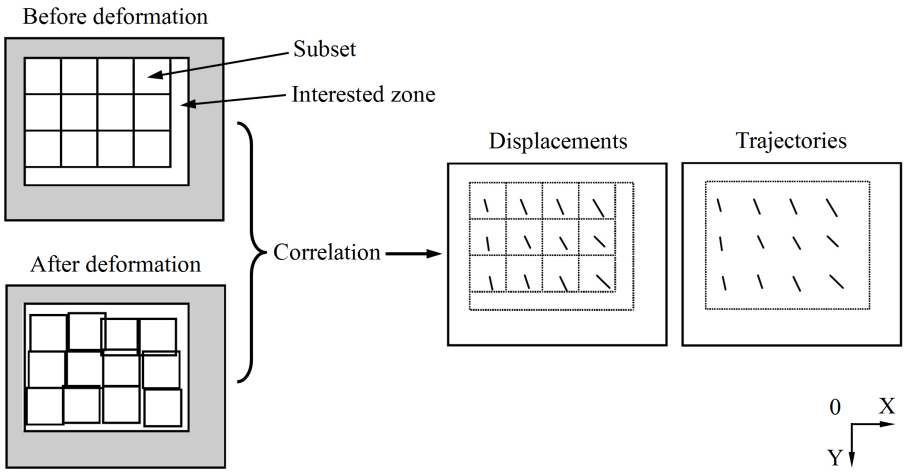

Figure 2.4: Principle of DIC [76]

The reason why a square subset, rather than an individual pixel, is selected for correlation is that the subset comprising a wider variation in gray levels will distinguish itself from other subsets, and can therefore be more uniquely identified in the deformed image.

2.2.3 Parameters of DIC

For the calculation of strain, the subset dimensions should be defined firstly. As shown in Figure 2.5, the length and width ($L_1 \times L_2$) of subset and the horizontal and vertical distances ($D_1 \times D_2$) are defined. The accuracy of strain calculation is dependent on the quality of speckle pattern, digital image and correlation algorithm [74]. Different sets of DIC parameters in CORRELA 2006 are compared to choose the best one for strain calculation. The main parameters are shown in Table 2.1.

2.3 A method for identifying onset of fracture

A method based on the evolution of major strain and the observation of the macroscopic image of specimen surface is proposed to identify the onset of fracture and the forming limit strains at fracture.

As shown in Figure 2.6, a square with a side length of 2.4 mm (64 × 64 pixels) is chosen around the central point of the specimen.

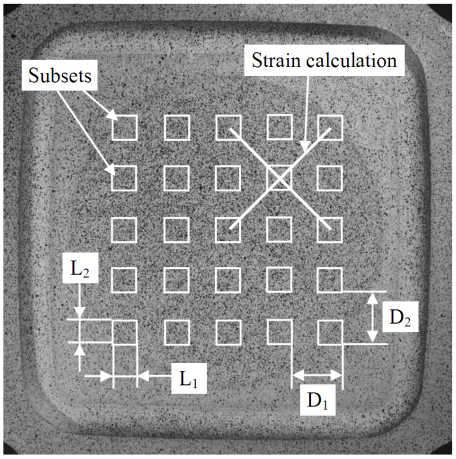

Figure 2.5: Subset dimensions used for DIC calculation

Table 2.1: Main parameters of DIC in CORRELA 2006

Subset	Size ($L_1 \times L_2$)	32 pixels × 32 pixels
	Distance ($D_1 \times D_2$)	8 pixels × 8 pixels
Correlation	Method	FFT and quadratic polynomial interpolation
	Initial value	By precedent displacement
	Displacement	Between precedent and current images
	Iterative accuracy	0.01 pixel
Calculation	Mode	Diagonal intersection
	Constant interval	4

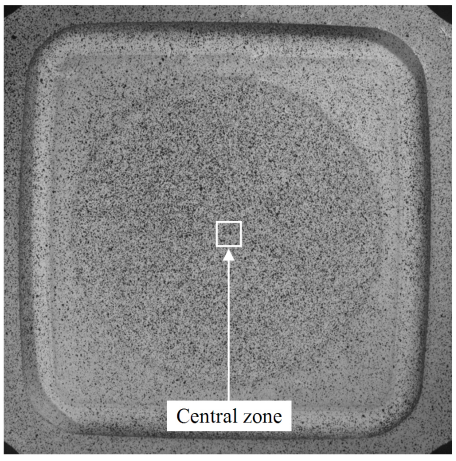

Figure 2.6: The central zone used for measuring the evolution of major strain

The evolution of major strain in the central zone under equibiaxial stretching is plotted in Figure 2.7. The strain versus time curve is typical of Portevin-Le-Chatelier (PLC) effect, which exhibits steps on the strain evolution. This phenomenon is well known for 5000 series aluminium alloys. In the central zone, the level of major strain increases with the time and an abrupt change can be observed at the end. As shown in Figure 2.8, a macroscopic crack appears when the abrupt change of major strain happens, while there is no macroscopic crack before the abrupt change of major strain. It can be concluded that the appearance of macroscopic crack is accompanied with an abrupt increase of major strain in a very short time of 0.004s.

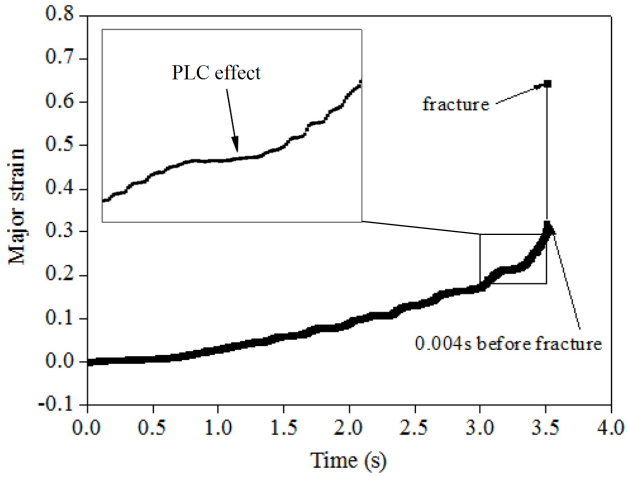

Figure 2.7: Evolution of major strain of AA5086 specimen under equibiaxial stretching

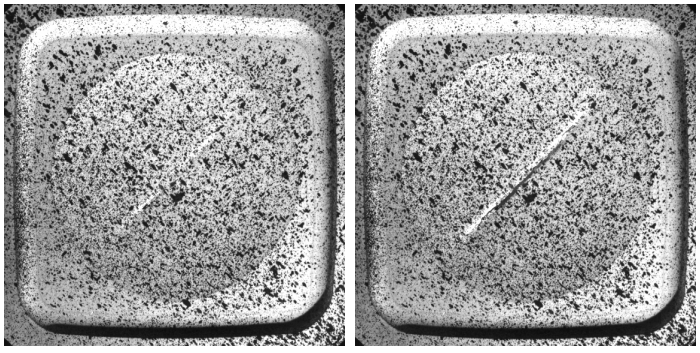

(a) 0.004s before fracture (b) fracture

Figure 2.8: DIC figures of AA5086 specimen under equibiaxial stretching

More strain paths are considered for the proposed method to identify the onset of fracture. Same phenomena are observed in Figure 2.9 under plane-strain tension and in Figure 2.10 under uniaxial tension. In the present research, the major and

minor strains of the central zone at the time just before onset of macroscopic fracture are defined as the forming limit strains at fracture.

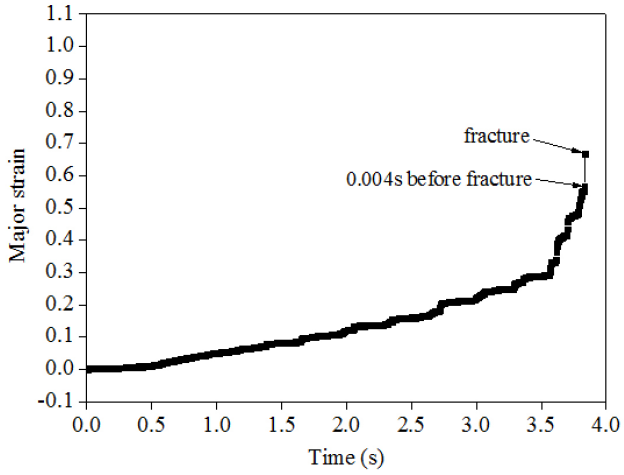

Figure 2.9: Evolution of major strain of AA5086 specimen under plane-strain tension

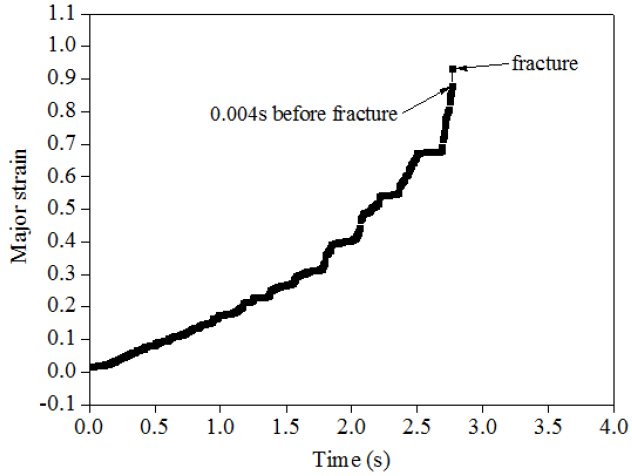

Figure 2.10: Evolution of major strain of AA5086 specimen under uniaxial tension

2.4 Experimental FLCF of AA5086 sheet under linear strain paths

2.4.1 Identification of forming limit strains

For producing the whole FLCF of AA5086 sheet, different linear strain paths must be considered. Table 2.2 shows different velocity ratios of actuators for producing various linear strain paths from equibiaxial stretching to uniaxial tension. The axis X corresponds to the rolling direction of the AA5086 sheet.

Table 2.2: Different velocity ratios of actuators for producing linear strain paths

Velocity ratio R	1	0.75	0.5	0.25	0.1	0.05	uniaxial tension
Velocity in axis X (mm/s)	1	1	1	1	1	2	1
Velocity in axis Y (mm/s)	1	0.75	0.5	0.25	0.1	0.1	free

Actuators remotely act on the central zone of the specimen and strain ratio in the center is not exactly the same as the one imposed by actuator velocities. The small difference may be caused by: (1) anisotropic behavior of the material; (2) heterogeneous shape of the specimen: (3) synchronization of the actuators. As shown in Figure 2.11, experiments are carried out under different strain paths from equibiaxial stretching to uniaxial tension. The dashed lines indicate the strain paths under equibiaxial stretching, plane-strain tension and uniaxial tension. All the strain paths are almost linear for a constant velocity ratio. The solid markers represent the forming limit strains at fracture under different strain paths identified by the method in section 2.3.

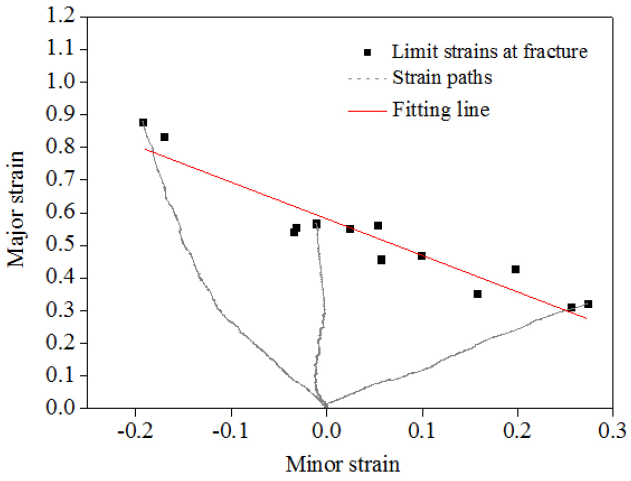

Figure 2.11: Forming limit strains at fracture of AA5086 sheet under different linear strain paths

As described by the Fracture Forming Limit line concept, the forming limit strains at fracture can be fitted by a straight line falling from left to right expressed by [5]:

$$\varepsilon_{major} = k\varepsilon_{minor} + A \tag{2.1}$$

Based on the experimental results presented in Figure 2.11 and a least-square method, it can be obtained that k=-1.13 and A=0.58 (R-square value 0.89).

2.4.2 Comparison of FLCF and FLCN under linear strain paths

For comparison, Figure 2.12 shows forming limit strains at necking and fracture for the same specimen. Forming limit strains at necking have been determined by fulfilling the standard requirements concerning the use of modified position-dependent method, which is described in [27]. As expected, forming limit strains at fracture are higher than those at necking, especially for plane-strain tension. For uniaxial tension and equibiaxial stretching, necking is rapidly followed by a crack onset.

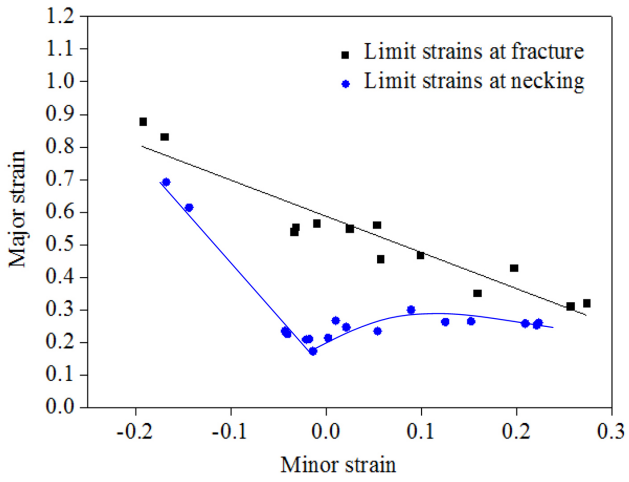

Figure 2.12: Forming limit strains at necking and fracture of AA5086 sheet under different linear strain paths

One can notice the high level of major strain at necking for uniaxial tension (between 60% and 70%). As discussed in [11], due to the specimen geometry, the mechanisms of the necking onset are different in the in-plane biaxial test and in the conventional Marciniak test. This difference can explain the improvement of formability observed with the cruciform specimen shape. For the cruciform shape, the forming limit criterion detects the onset of localized necking whereas for the Marciniak test (not really representative of the complex shape of industriel parts under uniaxial tension), the appearance of diffuse necking probably accelerates the onset of localized necking. For the cruciform shape, the in-plane strain evolutions are relatively stable before localized necking. Therefore, a high level of major strain at necking is obtained by using the cruciform specimen.

Some conclusions are obtained for the Section 2.4 as follows: (1) The in-plane biaxial tensile test with a dedicated cruciform specimen permits to identify the experimental forming limit strains at fracture under different linear strain paths from equibiaxial stretching to uniaxial tension through plane-strain tension; (2)

The forming limit strains at fracture of AA5086 sheet can be identified by a time-dependent method combining the evolution of major strain with the observation of the macroscopic crack at the specimen surface; (3) A straight line (FLCF) can be used to fit the forming limit strains at fracture of AA5086 sheet under different linear strain paths.

2.5 Prediction of FLCF for AA5086 sheet under linear strain paths

2.5.1 Numerical model

As shown in Figure 2.13, a predictive model for forming limit strains at fracture has been built by modeling the cruciform specimen shape with the finite element (FE) method. FE simulations have been carried out with the commercial software ABAQUS (implicit solver). Only one-quarter of the specimen is analyzed for considering the symmetry of the specimen geometry. Tetrahedral elements are used (more than 130,000 elements) and a refined mesh (average mesh size of 0.25mm) is assumed where fracture may appear. Different displacement ratios are imposed on the two orthogonal directions to reproduce the experimental strain paths.

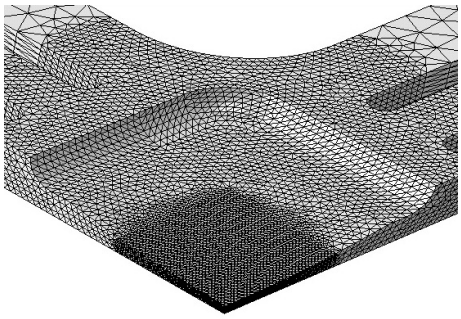

Figure 2.13: 3D Mesh of the AA5086 specimen

To describe the material elasticity, a Young's modulus of 73022 MPa and a Poisson's ratio of 0.33 are considered. The Hill48 yield criterion for plane stress condition is adopted and the equivalent stress $\bar{\sigma}$ is expressed by a quadratic function of the following type:

$$\bar{\sigma}^2 = (G+H)\sigma_{xx}^2 + (F+H)\sigma_{yy}^2 - 2H\sigma_{xx}\sigma_{yy} + 2N\sigma_{xy}^2 \tag{2.2}$$

The parameters of Hill48 yield criterion for AA5086 sheet are identified by the authors in [77]. As shown in Table 2.3, three anisotropic coefficients (r_0, r_{45}, r_{90}) were obtained by the uniaxial tensile tests carried out along the rolling, diagonal

and transverse directions. The constants F, G, H, and N for plane stress conditions are calculated from these three plastic anisotropic coefficients.

Table 2.3: Lankford's coefficient and Hill48 yield parameters

r_0	r_{45}	r_{90}	F	G	H	L	M	N
0.49	0.62	0.52	0.632	0.671	0.329	1.500	1.500	1.460

A modified form of Voce's hardening law [78] has been adopted to limit the saturating behaviour of classical Voce's formulation:

$$\bar{\sigma} = \sigma_0 + K\sqrt{1 - exp(-n\bar{\varepsilon}_p)} \tag{2.3}$$

Using a dedicated cruciform specimen, an experimental biaxial flow stress curve for AA5086 sheet up to 30% of the equivalent plastic strain has been obtained by the authors [79]. The parameters σ_0, K and n were identified (Table 2.4) for Hill48 yield criterion thanks to an inverse procedure.

Table 2.4: Identified parameters of modified Voce's hardening law for Hill48 yield criterion

σ_0 (MPa)	K (MPa)	n
153.62	249.75	3.392

2.5.2 Prediction of FLCF

Three ductile fracture criteria: Cockroft and Latham, Brozzo and Ayada are used to predict the FLCF of AA5086 sheet. As shown in Figure 2.14, the damage value C_i of the three ductile fracture criteria can be calculated at each step of the finite element simulation with the help of user subroutine. For each criterion, the fracture is assumed to happen when a critical damage value is reached at one step of calculation. At this step, the corresponding major and minor strains are used as the forming limits at fracture.

Figure 2.15 shows the numerical strain paths produced by the cruciform specimen. When one ductile fracture criterion is considered, the evolutions of damage value for each strain path are determined. The same critical damage value of the ductile fracture criterion is used for each strain path to find the step of fracture and the corresponding numerical major and minor strains at fracture. As shown in the figure, the black points show the numerical limit strains under different linear strain

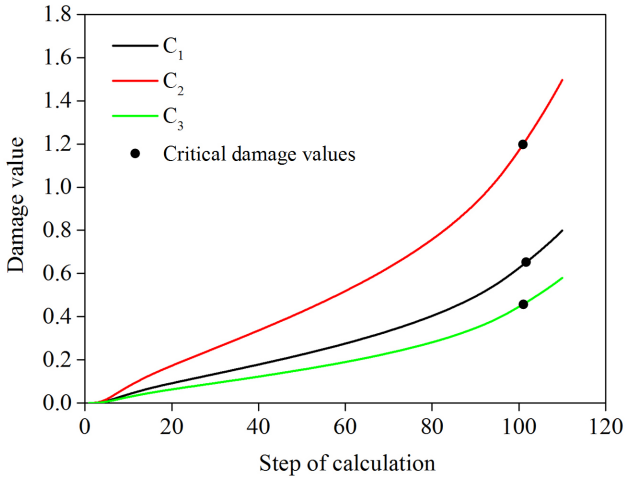

Figure 2.14: Evolution of damage value under equibiaxial stretching

paths identified by the critical damage value. These points are used to produce a numerical FLCF for the considered criterion.

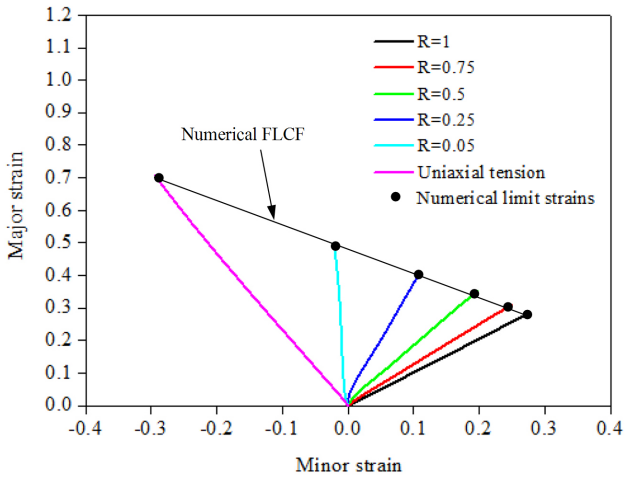

Figure 2.15: Numerical FLCF under different linear strain paths identified by the same critical damage value

The critical damage value in numerical simulation depends on the experimental results. For calibration of the critical damage value, the experimental forming limit strains under uniaxial tension, plane-strain tension and equibiaxial stretching are respectively considered and compared. Figure 2.16 (a) shows the FLCFs calculated with experimental forming limit strains under equibiaxial stretching. The FLCFs from Cockroft and Latham criterion and Ayada criterion are approximately described by a linear shape, while the FLCF identified by Brozzo criterion shows a curve profile. A better correlation is found with Ayada criterion whereas Cockroft and Latham criterion and Brozzo criterion respectively underestimates and over-

estimates the experimental forming limit strains. For the uniaxial tension, Ayada criterion underestimates a little the experimental results. The FLCFs identified by the three criteria for a calibration under plane-strain and uniaxial tensions are shown in Figure 2.16 (b) and (c), respectively. The critical damage values of the criteria under different strain paths are shown in Table 2.5. For the right hand side of the forming limit diagram (positive minor strains), the correlation between the experimental forming limit strains and the ones from Ayada criterion is the best, the calibration of C_3 gives approximately the same results for plane-strain tension (C_3=0.43) or equibiaxial stretching (C_3=0.46). For the three criteria, the prediction is reasonable when the calibration of critical damage value is done under plane-strain tension (Figure 2.16 (b)). But when the calibration is made with experimental forming limit strains under uniaxial tension, which is usually the case when only uniaxial experiments are available, the predictions under the expansion mode are very imprecise and strongly overestimated for the three criteria. Globally, for this aluminium alloy, Ayada criterion gives the best predictions among the three criteria and it is recommended to calibrate the critical damage values under plane-strain condition.

Table 2.5: The critical damage values of the criteria under different strain paths

Loading state	C_1	C_2	C_3
Equibiaxial stretching	0.64	1.20	0.46
Plane-strain tension	0.80	0.93	0.43
Uniaxial tension	1.18	1.29	0.64
Difference in C_i	0.54 (45.8%)	0.36 (27.9%)	0.21 (32.8%)

2.5.3 Effect of yield criterion on prediction of FLCF

In order to evaluate the impact of the choice of yield criterion, the predictions of FLCFs by using the Hill48 criterion and the isotropic Mises criterion are compared. The Cockcroft and Latham, Brozzo and Ayada criteria are used for comparison and the recommended calibration procedure is applied (under plane-strain tension). The modified form of Voce's hardening law identified by the biaxial tensile test with the Hill48 yield criterion is considered (Table 2.4).

Figure 2.17 shows that the shapes of the FLCFs obtained with the two yield criteria are close. As shown in Table 2.6, there is small difference in the critical damage values of two yield criteria for each ductile fracture criterion. It can be concluded that the yield criterion has a small influence on the prediction of FLCF.

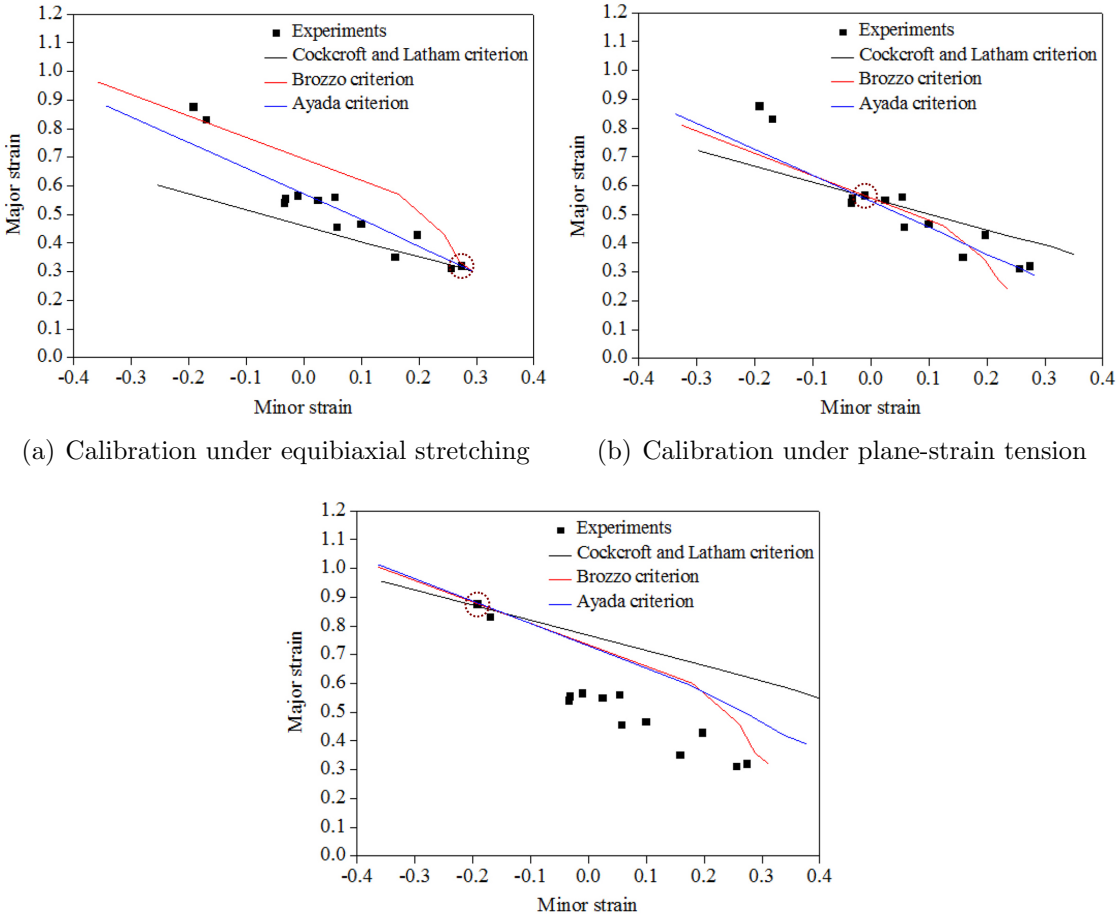

(a) Calibration under equibiaxial stretching

(b) Calibration under plane-strain tension

(c) Calibration under uniaxial tension

Figure 2.16: The numerical FLCFs of AA5086 sheet identified by three criteria under different strain paths

Table 2.6: The critical damage values of the criteria with different yield criteria

Yield criterion	C_1	C_2	C_3
Hill48 yield criterion	0.80	0.93	0.43
Mises's criterion	0.91	1.08	0.50

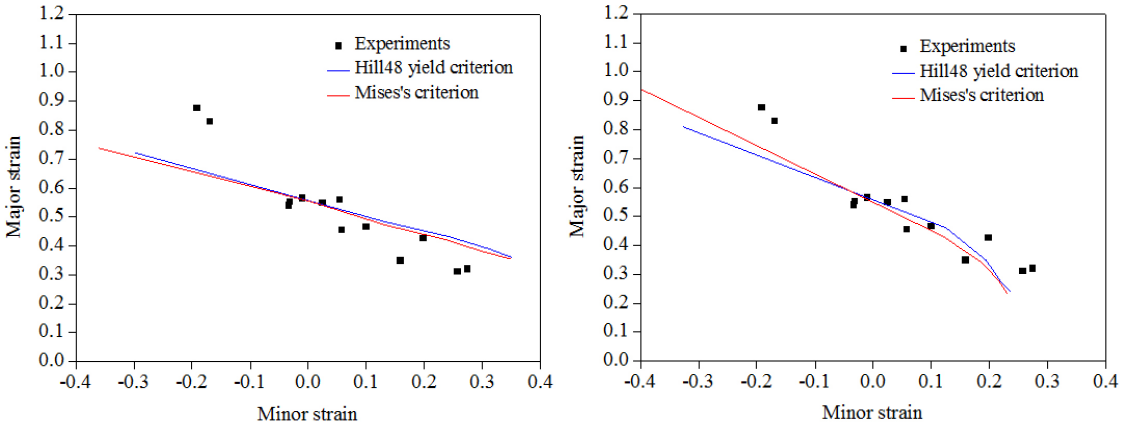

(a) Criterion from Cockcroft and Latham

(b) Criterion from Brozzo

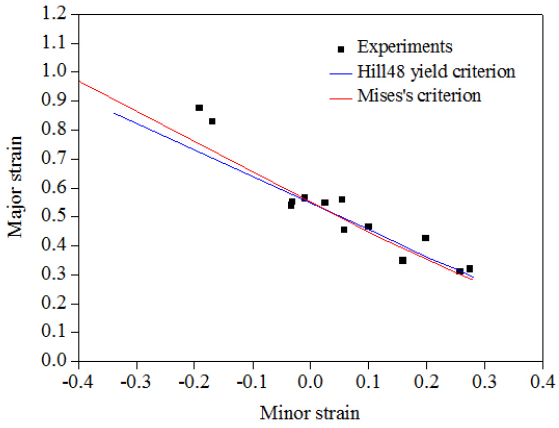

(c) Criterion from Ayada

Figure 2.17: Prediction of FLCFs for AA5086 sheet with different yield criteria and fracture criteria

Some conclusions are obtained for the Section 2.5: (1) The numerical predictions of FCLFs with three ductile fracture criteria (Cockcroft and Latham, Brozzo and Ayada) from literatures can give very different results, depending on the experimental forming limits chosen to calibrate the critical damage value; (2) The Ayada criterion gives the best result and is insensitive to the experimental forming limits used for calibration in the expansion mode; (3) The yield criterion has small influence on the prediction of FLCFs with the three ductile fracture criteria;

2.6 Experimental FLCF of AA5086 sheet under non-linear strain paths

2.6.1 Identification of forming limit strains

As shown in Figure 2.18, two steps of loading are considered in the non-linear strain path. The first step of loading corresponds to uniaxial tension in the rolling direction of the cruciform specimen. As shown in Table 2.7, different levels of displacement are used in the first step for producing different prestrains in uniaxial tension. For the second step of loading, the equibiaxial stretching is acted on the cruciform specimen until fracture. No unloading between the two steps is considered.

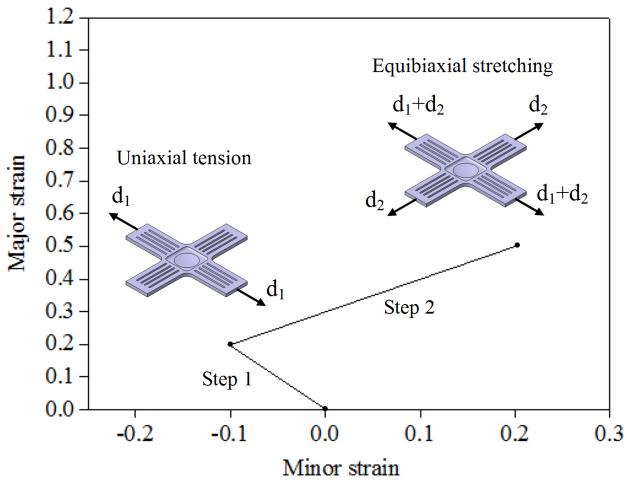

Figure 2.18: Non-linear strain path for AA5086 sheet

Table 2.7: Different prestrains corresponding to different pre-displacements in uniaxial tension

Pre-displacement	1.0 mm	1.5 mm	2.0 mm	2.5mm	3.0 mm
Major strain	5%	8%	10%	13%	19%

The forming limit strains at fracture of AA5086 sheet under the above type of non-linear strain paths are shown in Figure 2.19. As shown in the figure, the non-linear strain paths are presented and the solid markers represent the forming limit strains at fracture. For the first step of loading, different displacements from 1 mm to 3 mm corresponding respectively to prestrain from 5% to 19% are applied. An abrupt strain path change is then imposed between the two steps of loading. For the prestrain from 5% to 13%, the equibiaxial strain paths are obtained until the appearance of fracture. However, the plane-strain path is presented after the first step of loading with a prestrain of 19%, and the fracture happens quickly after the change of strain path.

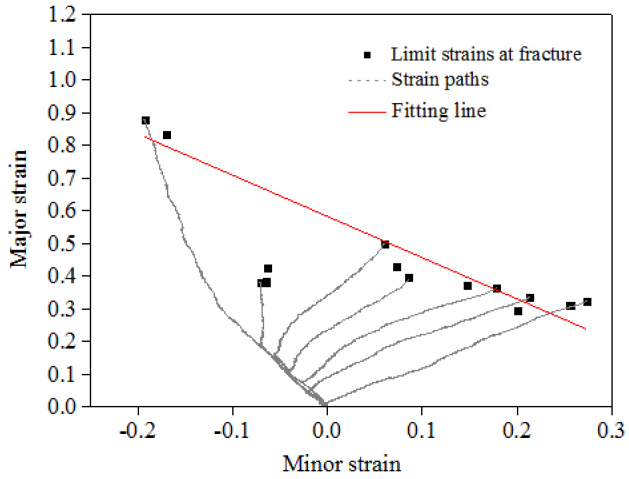

Figure 2.19: Forming limit strains at fracture of AA5086 sheet under non-linear strain paths

The forming limit strains at fracture under non-linear strain paths without the results of prestrain 19% can also be fitted by a straight line (R-square value 0.93):

$$\varepsilon_{major} = -1.26\varepsilon_{minor} + 0.59 \tag{2.4}$$

2.6.2 Comparison of FLCF and FLCN under non-linear strain paths

Figure 2.20 shows the comparison of forming limit strains at necking and fracture under non-linear strain paths for the AA5086 sheet. The position-dependent method has been used for the determination of FLCN under non-linear strain paths. For all strain paths in this figure, the forming limit strains at fracture are higher than those at necking.

Léotoing et al. [27] have compared the modified position-dependent method and the critical ratio method to produce the experimental FLCN for AA5086 sheet.

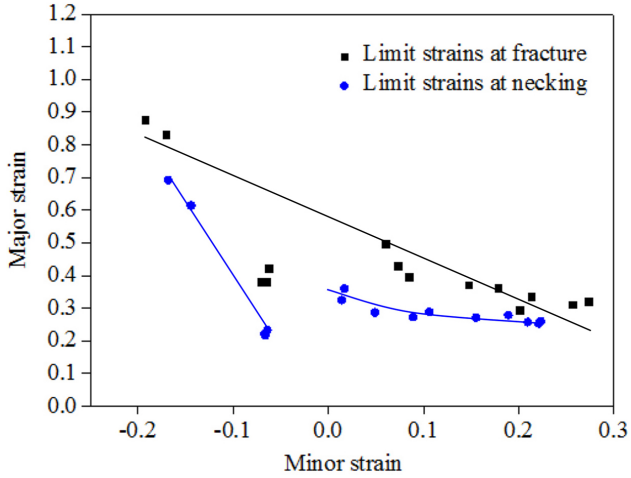

Figure 2.20: Forming limit strains at necking and fracture of AA5086 sheet under non-linear strain paths

The FLCNs identified by the two methods are very close for all strain paths. In the critical ratio method, necking is assumed to happen when the equivalent strain incremental ratio of two selected zones (one inside and the other outside the necking area) reaches a critical value. As described in their study, a systematic increase of equivalent strain increment ratio occurs after the strain path change, which indicates the appearance of "pseudolocalization" in the central area of cruciform specimen. As shown in Figure 2.21, when the prestrain level is under 13%, the pseudolocalization is stabilized after a period of time, then the ratio decreases before a continuous increase until the onset of necking. For the prestrain level of 19%, the increase of the equivalent strain increment ratio is abrupt and exceeds the critical value for detecting the onset of necking, so a premature necking and the following fracture are observed.

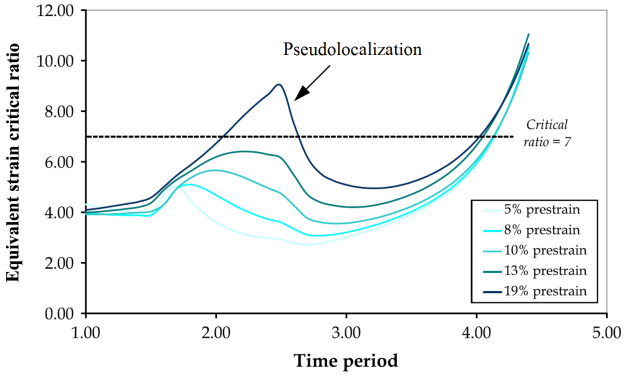

Figure 2.21: Equivalent strain increment ratio for different prestrains [27]

The strain paths after the strain path changes in Figure 2.19 can be analyzed by the appearance of pseudolocalization. For the prestrain level of 19%, the pseudolo-

calization after the strain path change can not be stabilized, so the onset of necking appears and results in a plane-strain path until fracture. For the prestrain level from 5% to 13%, the pseudolocalization is stabilized and the strain path changes from uniaxial tension to equibiaxial stretching. For the prestrain level of 13%, the process of the stabilization of pseudolocalization can be observed from the shape of strain path after the strain path change.

2.6.3 Comparison of FLCF under linear and non-linear strain paths

Figure 2.22 shows the forming limit strains at fracture under linear and non-linear strain paths for the same specimen. As discussed in previous sections, the forming limit strains at fracture under linear and non-linear strain paths can be fitted by two straight lines, respectively. As shown in this figure, the difference between the levels of two fitting lines is small.

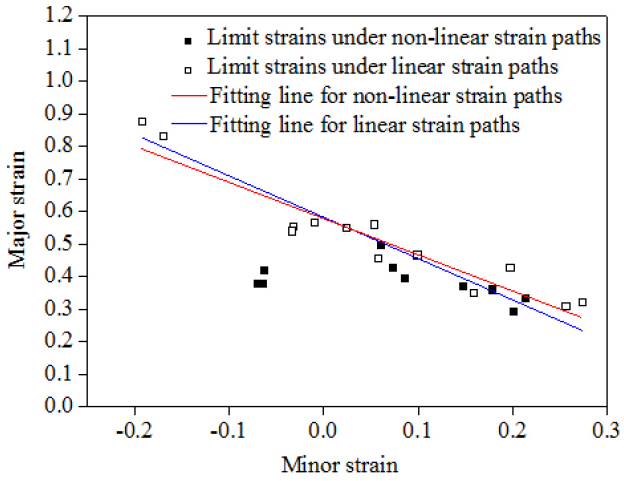

Figure 2.22: Forming limit strains at fracture of AA5086 sheet under linear and non-linear strain paths

For the non-linear strain paths, the forming limit strains at fracture with the prestrain from 5% to 13% can be fitted by this straight fitting line, while the forming limit strains at fracture with the prestrain of 19% are under the fitting line. Clearly, the strain path change has almost no effect on the forming limit strains at fracture when small prestrains (major strain below 19%) under uniaxial tension are used in the first step of loading along the rolling direction.

2.6.4 Comparison of FLCN under linear and non-linear strain paths

Figure 2.23 summarizes the experimental forming limit strains at necking under linear and non-linear strain paths identified by the modified position-dependent method. It can be seen that the FLCN under linear strain paths is continuous while the FLCN under non-linear strain paths is not. For small prestrains in uniaxial tension along the rolling direction (major strain level below 19%), the FLCN shifts upward and then the sheet formability is improved compared with the FLCN under linear strain paths. For the prestrain level higher than 15%, a premature necking appears and the formability is reduced strongly.

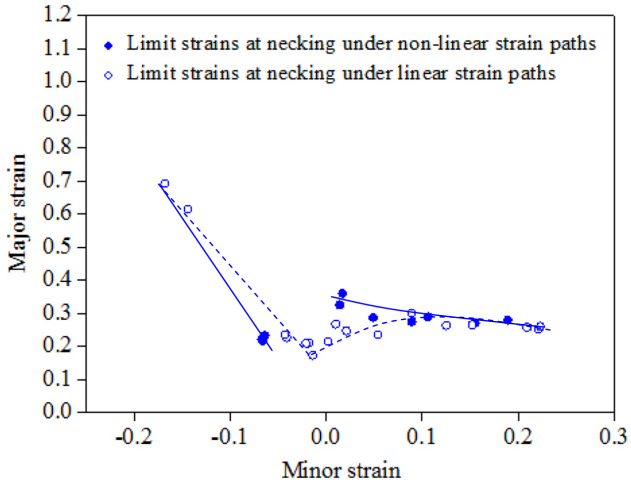

Figure 2.23: Forming limit strains at necking of AA5086 sheet under linear and non-linear strain paths

Some conclusions are obtained for the Section 2.6: (1) The in-plane biaxial tensile test with a dedicated cruciform specimen permits to identify the experimental forming limit strains at fracture under non-linear strain paths (uniaxial tension followed by equibiaxial stretching); (2) For moderate prestrains (less than 19%), the forming limit strains at fracture of AA5086 sheet under non-linear strain paths can be fitted by a straight line; (3) The strain path change has very small effect on the experimental FLCF while it has effect on the experimental FLCN.

2.7 Prediction of FLCF for AA5086 sheet under non-linear strain paths

The numerical non-linear strain paths with different prestrains in uniaxial tension are shown in Figure 2.24. The abrupt strain path change is realized in numerical

simulation for the strain paths with prestrain from 5% to 13%. The critical damage value of Ayada criterion (C_3=0.43) used for identifying the numerical FLCF under linear strain path is adopted here to produce the numerical FLCF under non-linear strain path.

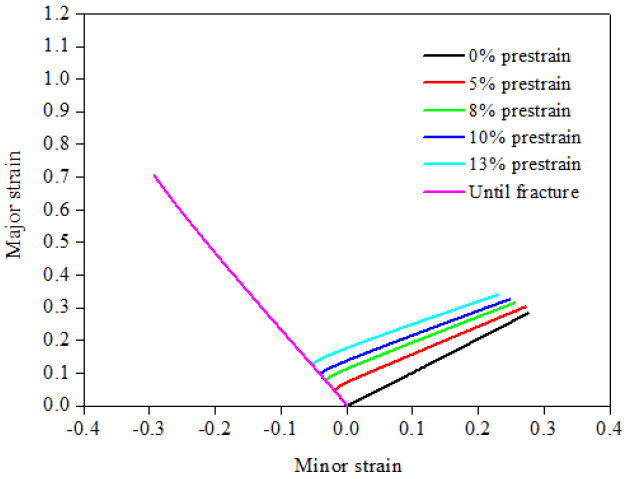

Figure 2.24: Numerical non-linear strain paths produced by cruciform specimen

Figure 2.25 shows the experimental forming limit strains at fracture and the predictive FLCF identified by Ayada criterion under non-linear strain paths. As shown in the Figure 2.25, the numerical FLCF under non-linear strain paths presents a linear shape. For the right side of the forming limit diagram, the numerical FLCF identified by Ayada criterion gives good prediction. However, for the left side it overestimates the experimental forming limit strains at fracture with the prestrain of 19%.

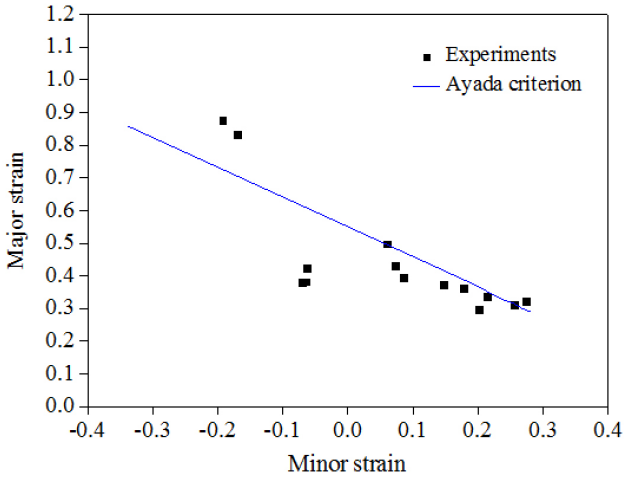

Figure 2.25: Experimental results and prediction of FLCF with Ayada criterion under non-linear strain paths

As shown in Figure 2.26, the numerical FLCFs under linear and non-linear strain paths are almost overlapped for a wide range of strain path from equibiaxial stretching to uniaxial tension. It can be concluded that the strain path change has almost no effect on the numerical FLCF calculated by the Ayada criterion.

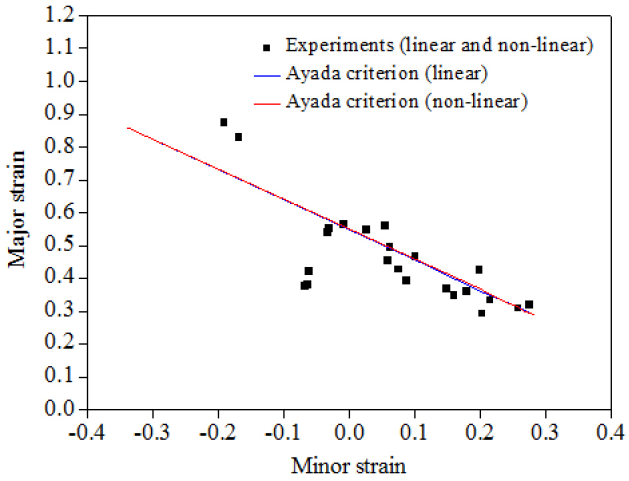

Figure 2.26: Comparison of numerical FLCFs under linear and non-linear strain paths identified by Ayada criterion

2.8 Investigation of fracture locus by using the cruciform specimen

The forming limits at fracture can also be described by using the fracture locus in strain and stress space. Different stress triaxialities are produced by using different loading conditions on the cruciform specimen of AA5086 sheet, and then the fracture locus will be discussed.

The Mises yield criterion is adopted and the experimental FLCF (fitting line in Figure 2.11) is used to identify the onset of fracture in simulation. The evolution of stress triaxiality for linear strain paths is shown in Figure 2.27. The stress triaxiality during the test is not constant, so the average value of stress triaxiality [68] is introduced to construct the fracture locus in stress and strain space:

$$(\frac{\sigma_h}{\bar{\sigma}})_{av} = \frac{1}{\bar{\varepsilon}_f} \int_0^{\bar{\varepsilon}_f} \frac{\sigma_h}{\bar{\sigma}} \, d\bar{\varepsilon} \tag{2.5}$$

where $\bar{\varepsilon}$ is the equivalent strain and $\bar{\varepsilon}_f$ is the equivalent strain at fracture.

The fracture locus is produced based on the equivalent strain at fracture and the average stress triaxiality for each strain path. As shown in Figure 2.28, the equivalent strain at fracture increases with decreasing the average stress triaxiality

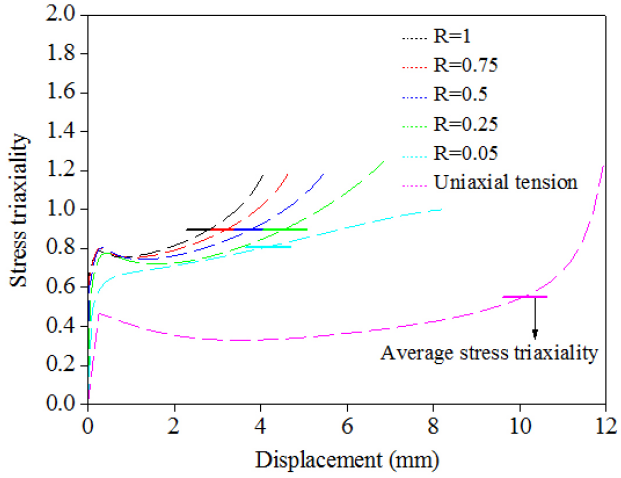

Figure 2.27: Evolution of stress triaxiality for linear strain paths

and the results can be fitted by a polynomial curve. The level of average stress triaxiality decreases when the strain path changes from equibiaxial stretching (R=1) to uniaxial tension across plane-strain tension (R=0.05). A very small decrease of the average stress triaxiality from R=1 to R=0.25 is found.

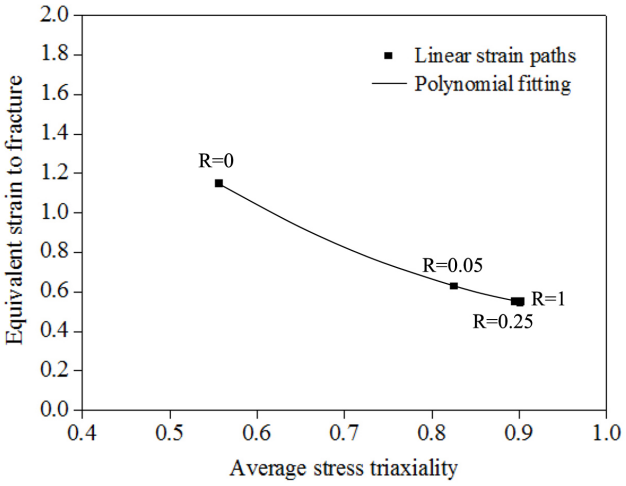

Figure 2.28: Effect of stress triaxiality on equivalent strain at fracture

As shown in Figure 2.29, the cruciform specimen permits to produce the strain path R=−1. For this strain path, the velocity in axis X is fixed at 1 mm/s (tension) and the velocity in axis Y is fixed at -1 mm/s. The Ayada criterion with the critical damage value of 0.43 is used here to predict the onset of fracture and the forming limit strain at fracture of AA5086 sheet under strain path R=−1. However, as shown in Figure 2.30, the values of C_3 during the calculation for the strain path R=−1 are negative which is different from other strain paths.

For the Ayada criterion, the values of C_3 are calculated based on the equivalent

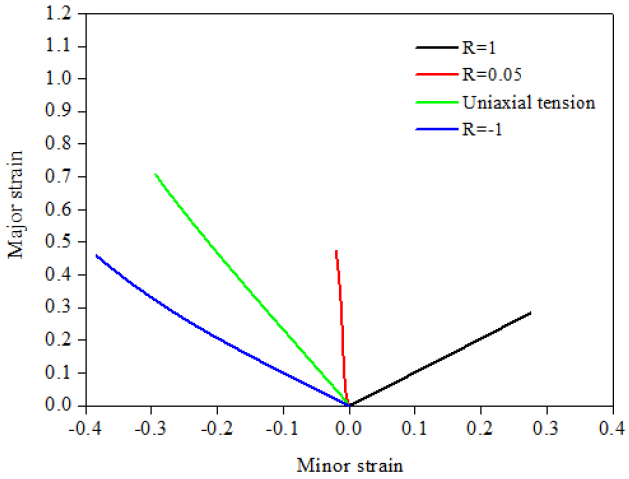

Figure 2.29: Numerical strain paths produced by the cruciform specimen

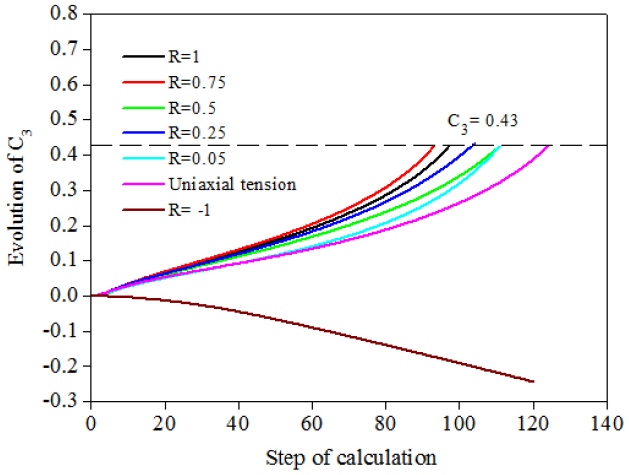

Figure 2.30: Evolution of C_3 under different linear strain paths

stress and hydrostatic stress. The Figure 2.31 (a) presents the positive values of equivalent stress for all strain paths. However, the values of hydrostatic pressure for the strain path R=−1 is negative while those for other strain paths are positive in Figure 2.31 (b). The critical damage value of 0.43 for positive strain paths can not be used for identifying the forming limit strain at fracture under strain path R=−1. It can be concluded that the Ayada criterion is not suitable for the strain path R=−1.

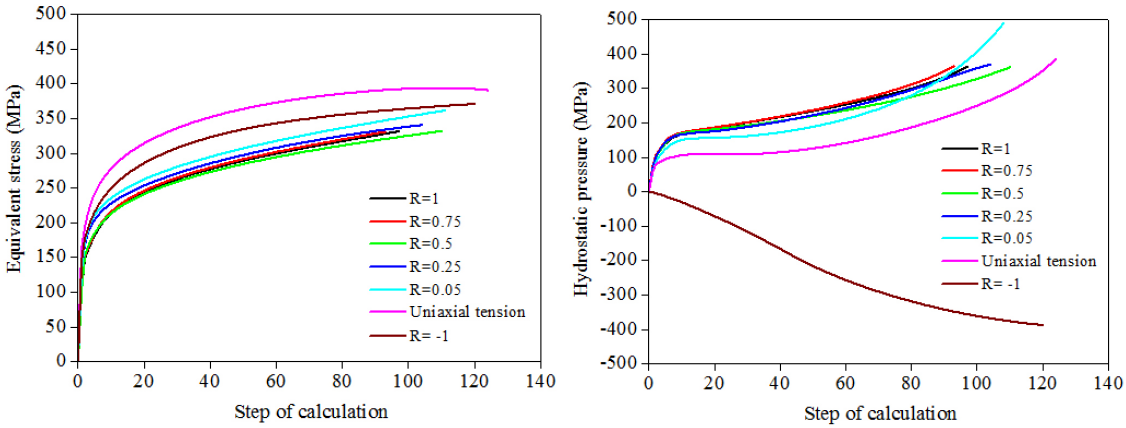

(a) Equivalent stress (b) Hydrostatic pressure

Figure 2.31: Evolution of stresses in the calculation with Ayada criterion

For the strain path R=-1, a negative stress triaxiality can be obtained, as shown in Figure 2.32. In this study, the experimental results for R=-1 is absent, so it is hard to identify the onset of fracture in simulation and calculate the average stress triaxiality. However, it is sure that the cruciform specimen permits to produce a wide range of stress triaxiality from negative value to high positive value.

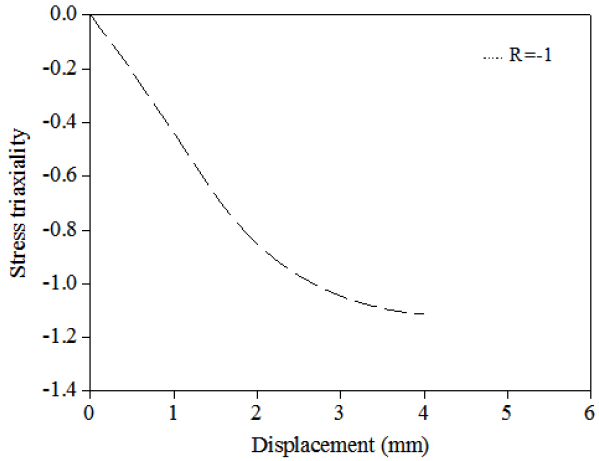

Figure 2.32: Evolution of stress triaxiality for strain path R=-1

2.9 Conclusion

In this chapter, the in-plane biaxial tensile test with a dedicated cruciform specimen has been used to investigate the forming limit strains at fracture of AA5086 sheet with an original thickness of 4 mm. The experimental results show that only one shape of specimen permits to reach strain paths from uniaxial tension to equibiaxial stretching, by piloting the velocity of actuators on the two perpendicular axes of the experimental device. The forming limit strains at fracture of AA5086 sheet can be identified by a time-dependent method combining the evolution of major strain with the observation of the macroscopic crack at the specimen surface.

In accordance with the Fracture Forming Limit Line concept, the forming limit strains at fracture under linear strain paths can be fitted by a straight line. The numerical predictions of FLCFs with three ductile fracture criteria from literatures can give very different results, depending on the experimental forming limit strains chosen to calibrate the critical damage value. The Ayada criterion gives the best predictive result.

Two steps of loading without unloading (uniaxial tension followed by biaxial stretching) are used to investigate the FLCF of AA5086 sheet under non-linear strain paths. The forming limit strains at fracture with the prestrain from 5% to 13% in uniaxial tension can be fitted by a straight fitting line, while the ones with the prestrain of 19% are lower than it. The pseudolocalization in the prestrain of 19% generates the premature necking and the following fracture, which leads to the lower limit strains at fracture. The numerical FLCFs under linear and non-linear strain paths calculated by the Ayada criterion are almost overlapped, which shows that the strain path change has almost no effect on the prediction of FLCF.

The cruciform specimen is also used to identify the fracture locus in equivalent strain and stress triaxiality space. Different linear strain paths are used to produce a wide range of stress triaxiality. The average stress triaxiality decreases when the strain path changes from equibiaxial stretching to uniaxial tension through plane-strain tension. The equivalent strain at fracture increases with decreasing the average stress triaxiality. Furthermore, this cruciform specimen permits to produce the numerical strain path R=−1, which can result in a negative stress triaxiality.

Results presented in this chapter have been performed on a 4 mm initial thickness sheet metal. In practical applications, thinner sheet metals are often used, so in the next two chapters, a new shape of cruciform specimen will be designed for a sheet metal with a smaller thickness.

Chapter 3

Optimization of cruciform specimen for sheet metal with a thickness of 2 mm

Résumé

Au chapitre précédent, la géométrie de l'éprouvette cruciforme utilisée, issue de travaux antérieurs, avait été déterminée dans une tôle d'épaisseur 4mm. Cette éprouvette comportait deux réductions successives d'épaisseur dans la zone centrale avec une épaisseur finale de 0.75mm au centre de l'éprouvette. Pour la caractérisation de tôles d'épaisseur plus faibles, comme c'est couramment le cas en mise en forme, il n'est pas envisageable d'appliquer un simple rapport de réduction aux différentes dimensions, notamment dans l'épaisseur, de l'éprouvette définie précédemment. Afin de pouvoir évaluer les déformations limites à striction et à rupture pour des tôles d'épaisseur plus faibles, la définition d'une nouvelle géométrie d'éprouvette est donc envisagée dans ce chapitre. On s'intéresse ici à la caractérisat-ion des limites à rupture de tôle de DP600 de 2mm d'épaisseur utilisées dans l'industrie automobile.

Après une revue bibliographique des principales formes d'éprouvette proposées dans la litérature, il apparait clairement que: (i) la présence de rainures dans les branches de l'éprouvette permet d'assurer une meilleure homogénéité de la déformation dans la zone centrale; (ii) une réduction d'épaisseur de la zone centrale est essentielle pour assurer la localisation de la déformation dans cette zone et uniquement dans celle-ci. Sur cette base, quatre formes d'éprouvette de la litérature ont été sélectionnées, re-dimensionnées en intégrant les contraintes d'encombrement ainsi que les capacités du banc de traction biaxiale et en imposant une épaisseur minimale de 0.75mm à la zone centrale. Le comportement de ces éprouvettes a été simulé numériquement à partir d'une modélisation EF de l'essai de traction equi-biaxiale. Après analyse des résultats de ces simulations, une étude paramétrique de la position des rainures et de la forme des bras a été menée. La forme optimale obtenue a ensuite été validée numériquement en imposant différents chemins de déformation (de la traction uniaxiale à l'état biaxial) afin de s'assurer que la localisation de la déformation apparaissait a priori bien au centre de l'éprouvette.

Enfin, l'effet de la réduction d'épaisseur par usinage sur les limites de formabilité de tôles de DP600 de 2mm d'épaisseur est analysé. Les résultats obtenus montrent qu'une réduction d'épaisseur par usinage n'a que peu d'influence sur les déformations limites à striction et qu'un effet relativement limité sur les limites à rupture.

3.1 Introduction

For the cruciform specimen in Chapter 2, the thickness in the reduced central zone is 0.75 mm while the original thickness of sheet metal is 4 mm. If this shape is scaled down for identifying the forming limits of sheet metal with an original thickness of 2mm, the final thickness of reduced zone will be 0.375 mm, which is very thin to achieve precisely due to the limit conditions of manufacturing. Therefore, a new shape of cruciform specimen should be proposed to investigate the forming limits at fracture for the sheet metal with a thickness of 2 mm.

In this chapter, a review of the cruciform specimen designing is presented in Section 3.2. Four cruciform specimens reported in previous literatures are redesigned for DP600 sheet with a thickness of 2 mm. Their efficiencies for investigating the forming limit strains at fracture under equibiaxial stretching are numerically compared through FE software ABAQUS in Section 3.3. Based on the numerical results of the four specimens, a new shape is proposed and optimized step by step for obtaining the fracture in the central point of specimen in Section 3.4. Lastly, the effect of thickness reduction on forming limits of DP600 sheet is investigated in Section 3.5.

3.2 A review of cruciform specimen designs

Many researches were presented in the area of in-plane biaxial tensile tests and various shapes of cruciform specimen were proposed for different applications: (1) characterization of yield locus; (2) determination of hardening model; (3) identification of forming limit curves.

The critical point for in-plane biaxial tensile test is the design of cruciform specimen [81]. Classically, three sensitive zones (Figure 3.1) can be identified in the cruciform specimen geometry: (1) the arms, (2) the transition zone between arms, and (3) the central zone. When designing a cruciform specimen it is important to ensure a large amount of deformation in the central zone of cruciform specimen, without stress concentrations in other zones, particularly when large strains are required [82].

3.2.1 Characterization of yield locus

By means of FE numerical simulation, Müller et al. [83] have optimized the cruciform specimen by varying the parameters R_1 and R_2 of notch to determine yield locus of sheet metal. Figure 3.2 shows the optimal cruciform specimen with notches at the corners. A large zone of homogeneous deformation before onset of strain

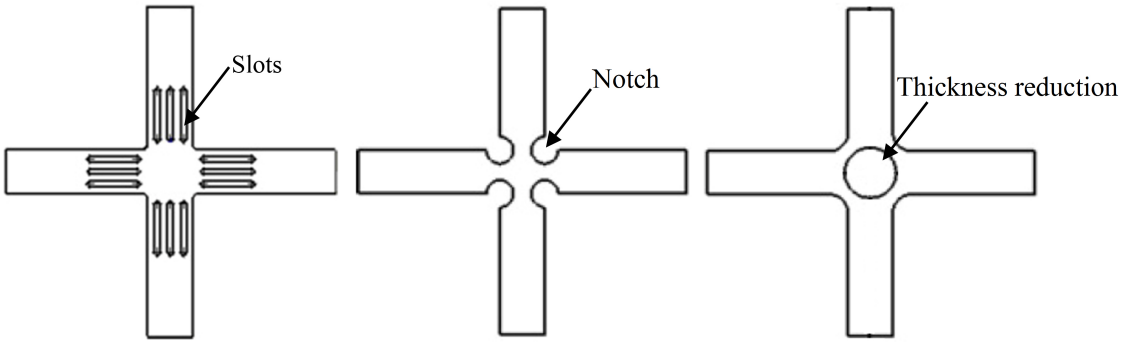

(a) Arm (b) Transition zone (c) Central zone

Figure 3.1: Design of cruciform specimen

localization is obtained. Banabic et al. [84] have also used this cruciform specimen to investigate a modified yield criterion.

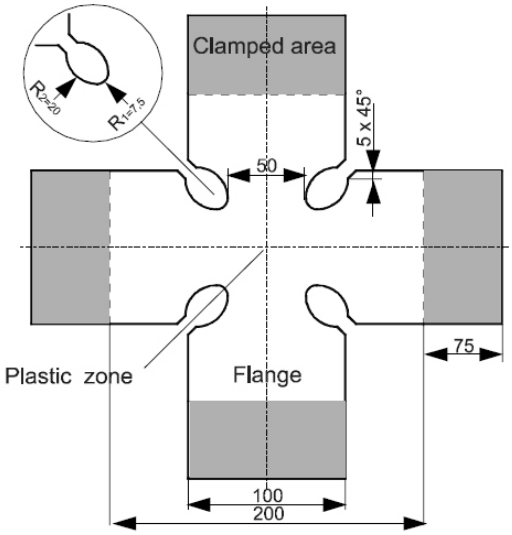

Figure 3.2: The cruciform specimen proposed by Müller et al. [83]

Naka et al. [85] have proposed a cruciform specimen to perform biaxial tensile tests at various temperatures for determining the initial yield surface. As shown in Figure 3.3, each arm of the specimen has two slots of 0.4 mm wide. The effects of temperature on the yield locus and plastic deformation of 5083-O Al-Mg alloy sheet have been experimentally investigated. The maximum plastic strain is about 6% at room temperature.

Kuwabara et al. [86, 87] have proposed a cruciform specimen with slots in the arms to obtain homogeneous deformation field in the central zone. As shown in Figure 3.4, there are seven slots in each arm and these slots are made by laser. The results show that the maximum equivalent strain reaches 4%.

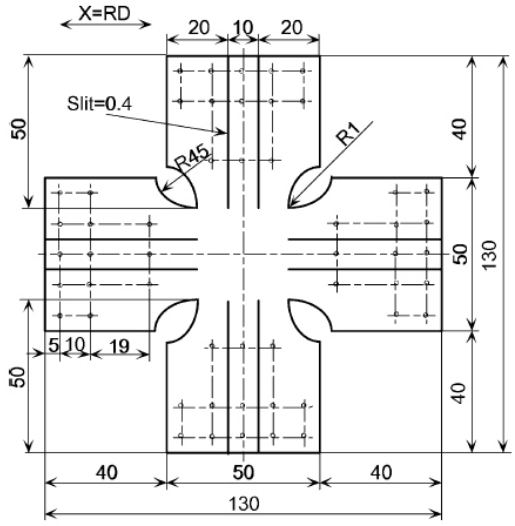

Figure 3.3: The cruciform specimen proposed by Naka et al. [85]

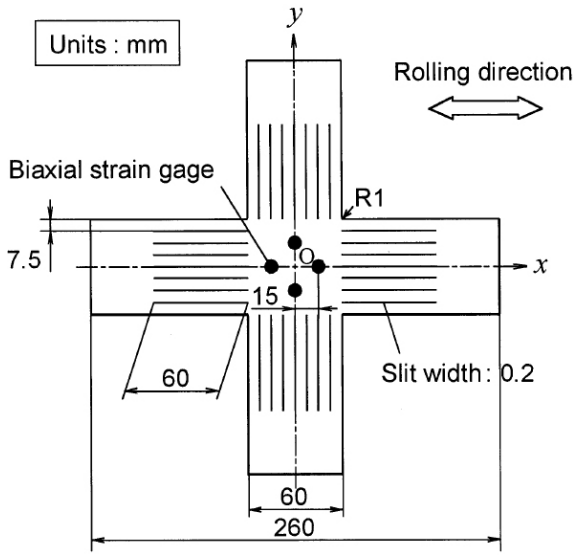

Figure 3.4: The cruciform specimen proposed by Kuwabara et al. [86]

Due to the existence of slots, the material in the central zone could flow with less constraint during the contraction or expansion, thus eliminating the shear force on the edge of central zone [88, 89]. However, the introduction of slots results in a reduction of the cross-section so that the arms are more compliant than the central zone. As a result, the arms deform excessively under load and limit the amount of useful strain in the central zone before fracture. To overcome this problem, either the thickness of central zone should be reduced or multiple layers of the arm should be stacked together so that the comparative rigidity of arm is increased [90].

3.2.2 Determination of hardening model

Figure 3.5 shows two different cruciform specimens proposed by Makinde et al. [91, 92] to investigate the mechanical behaviour of sheet metals and composite materials. The first has a thickness reduced circular central zone for small strains (3.5 (a)). The other one has a square central zone and slots in the arms for large strains (3.5 (b)).

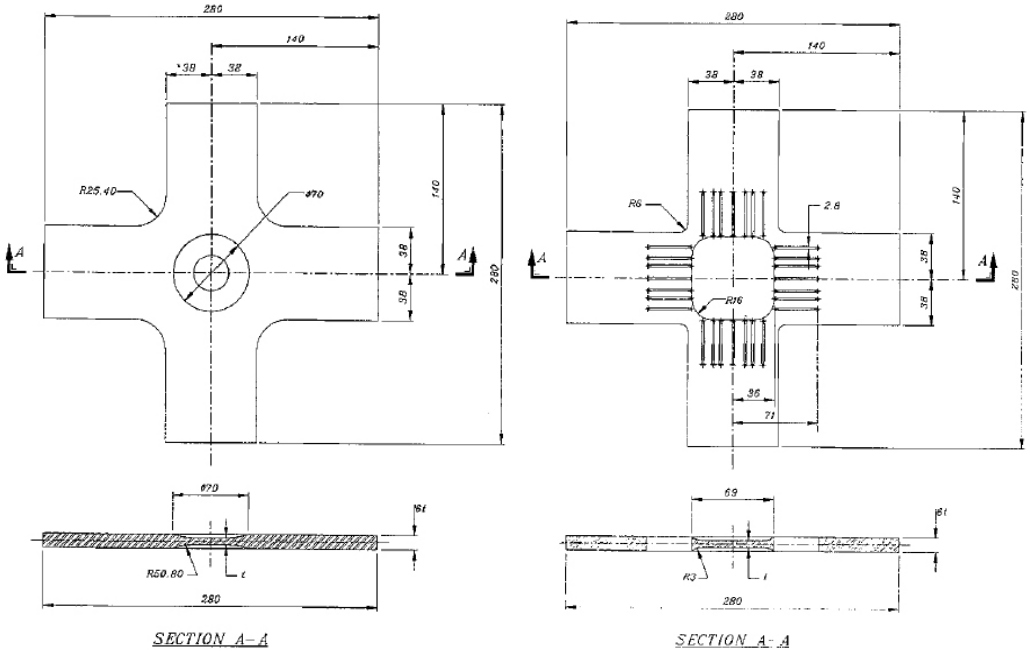

(a) A circular reduced central zone (b) A square central zone

Figure 3.5: Two crucifom specimens proposed by Makinde et al. [91, 92]

As shown in Figure 3.6, the cruciform specimen designed by Deng et al. [93] has four features: slots in the arms, reduced thickness, sharp radii and step transition between the arms and the central zone. The results of FE numerical simulation show that these features result in a uniform stress field in the central zone, except for a

thin boundary layer between the arms and the central zone. It is found that narrow, multiple, equally-spaced slots are preferable for creating homogeneous stress/strain. The specimen can be used for investigating the hardening behavior and the yield surface of the material for strains exceeding 15% for a dual-phase (DP590). However, the specimen cannot be used to assess the forming limits of sheet metal as failure initiates at the thin boundary layer at the periphery of the central zone.

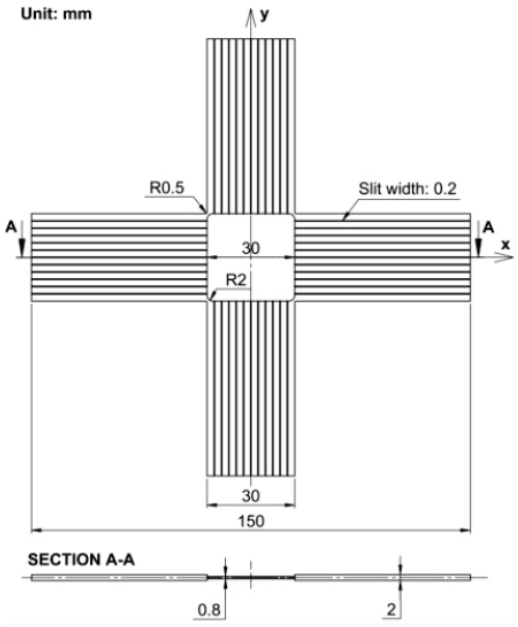

Figure 3.6: The cruciform specimen proposed by Deng et al. [93]

Liu et al. [79] have proposed a cruciform specimen (Figure 3.7) to identify the hardening behaviour of metallic sheet. One step of thickness reduction has been adopted. The arrangement of slots has been optimized to obtain the necking in the central zone of specimen. The equivalent strain can reach 30% for aluminium alloys. However, the maximum value of deformation is located on the edge of central zone, but not in the center.

For the aboved-mentioned cruciform specimens, the reduction of thickness is to make the central zone become weaker. However, a new idea to design the cruciform specimen for the cold-rolled DC5 steel sheet was proposed by Mitukiewicz et al. [94] recently. As shown in Figure 3.8, a rib is added in each corner between two arms to vary material properties locally in the specimen, which makes the area around the central zone become stronger. It means that the central zone is the weakest part of the specimen. However, only 8% plastic strain before fracture is reached in the central zone after the biaxial tensile test.

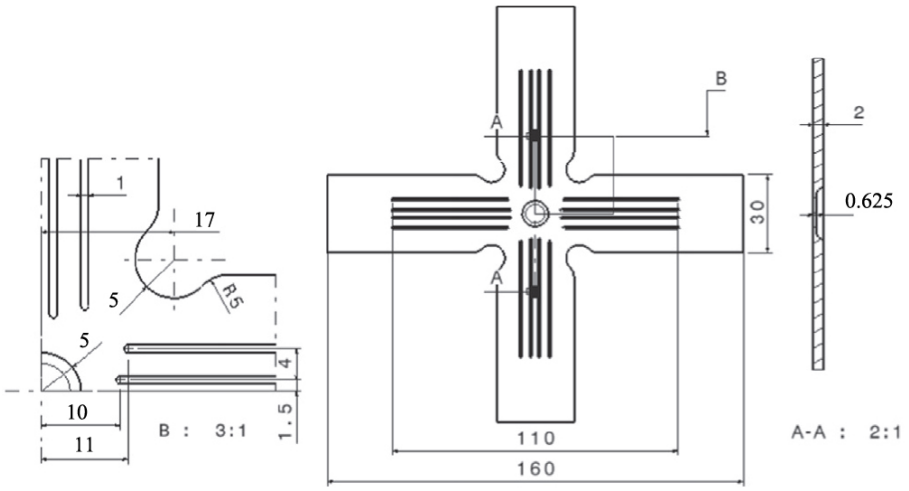

Figure 3.7: The cruciform specimen proposed by Liu et al. [79]

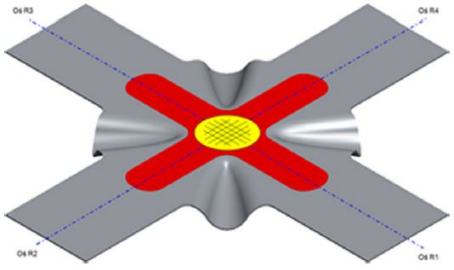

Figure 3.8: The cruciform specimen with 4 ribs [94]

3.2.3 Identification of forming limit curves

Tasan et al. [95] considered that it is not possible to achieve the fracture in the central zone by only adjusting the in-plane geometry of cruciform specimen. Based on the finite element simulations, the authors have proposed three important factors determining whether thickness reduction is successful in bringing localization to the center of cruciform specimen. Firstly, an optimum value for the radius of central zone has to be determined. When the zone is too large, stress localization may start between the corner of thickness reduced area and the corner of central zone. When it is too small, the localization tends to occur in the arms. Secondly, the final thickness of reduced central zone is important. If the thickness reduction is not enough, the localization still occurs in the arms. On the other hand, making the thickness reduction too severe may introduce size effects to the observed material behavior. Thirdly, the thickness reduction has to be carried out in such a way that the exact in-plane center of the specimen has the smallest thickness (as shown in Figure 3.9 (b)) to obtain localization in the center point. When the whole reduced central zone has the same reduced thickness (as in Figure 3.9 (a)), the localization initiates at the corner of reduced central zone. The final optimized geometry is shown in Figure 3.9 (c). Biaxial tensile tests for this cruciform specimen revealed that failure was obtained as predicted in the FE numerical simulation.

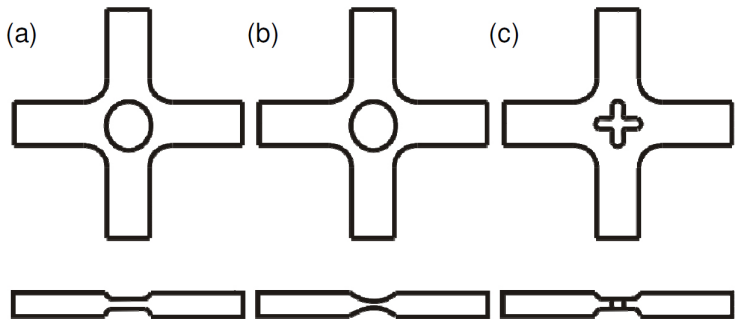

Figure 3.9: Three possible reduced-thickness cruciform geometries [95]

Abu-Farha et al. [96] have proposed two shapes of cruciform specimen for the biaxial tensile tests at elevated temperature (300°C) and quasi-static state until facture. One of the cruciform specimens is shown in Figure 3.10, and the arm is tapered at an angle (donated as T) with a smoothly varying thickness profile. The results show that the increasing of T value helps to shift plastic deformation closer to the central zone, but not into it. The other cruciform specimen for investigating fracture is shown in Figure 3.11. It has corner notches with a depth (donated as N) and a circular (flat-bottomed) recess in the gauge area of a diameter (donated as D). It is found that the value of N is a promotion of plastic deformation closer to

the central zone, but not within it.

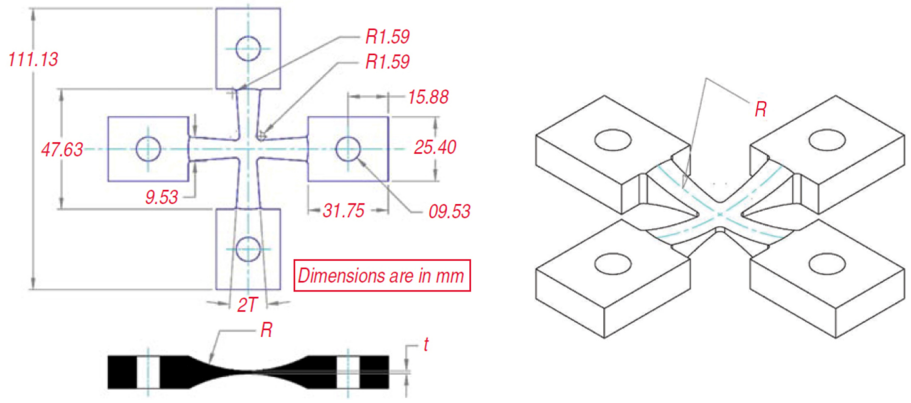

Figure 3.10: The first cruciform specimen proposed by Abu-Farha et al. [96]

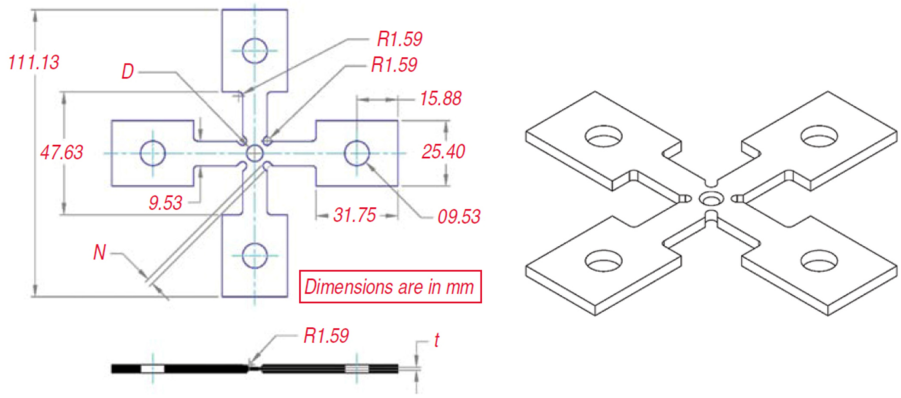

Figure 3.11: The second cruciform specimen proposed by Abu-Farha et al. [96]

Two different specimens have been compared by Makris et al. [97]: a cruciform specimen with constant arm width and one with a spline corner fillet. The optimization of the geometry was performed for the equibiaxial loading. The results of the numerical optimization show that the latter enables to achieve higher damage concentration in the central zone.

Abbassi et al. [98] have used a cruciform specimen to perform an analysis of fracture and instability during complex load testing. The cruciform specimen with a large radius of notch is shown in Figure 3.12. A good correlation between the numerical and experimental results of strain distribution is observed.

To ensure the fracture occurs within the central zone, Tiernan et al. [99] have used a process of optimization with FE simulation to optimize the cruciform specimen. The final optimal cruciform specimen is shown in Figure 3.13. The numerical results show very uniform stress distribution in the central zone of the specimen and the experimental results from this specimen are in good agreement with numerical

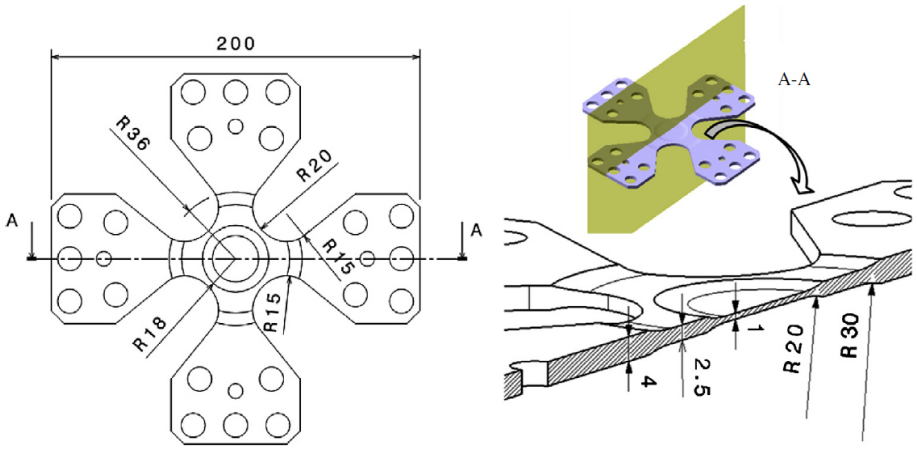

Figure 3.12: The cruciform specimen proposed by Abbassi et al. [98]

results. The use of slots in the arms for these specimens is found to be very effective in making uniform distribution of stress in the central zone. It is concluded that the cruciform specimen with no reduction in the central zone with either slot or radii at the intersection is fractured outside the central zone.

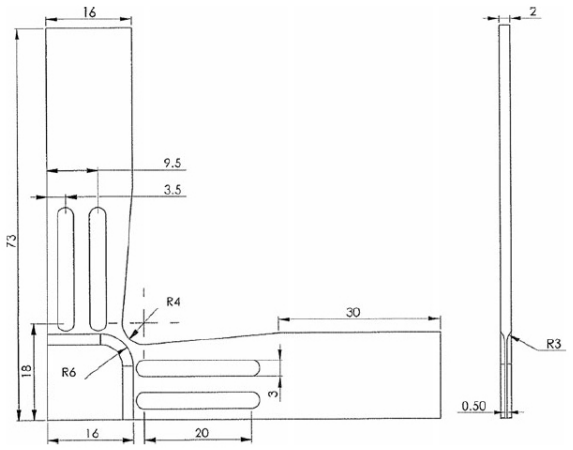

Figure 3.13: The cruciform specimen proposed by Tiernan et al. [99]

Lee et al. [100] have proposed a cruciform specimen to establish the right-hand side of FLD. As shown in Figure 3.14, a two-step thickness-reduced section is produced in the central zone. The first section is a circle and the second section is a square with rounded corner and with edges rotated by 45° relative to the axes of arms. The FLD was established by the modified Cockcroft criterion together with the limit strains obtained from simple tensile test and notched tensile test.

As shown in Figure 3.15, Abu-Farha et al. [101] have investigated these cruciform specimens to obtain the fracture in the central zone for elevated-temperature biaxial tensile tests. The center recess shape, the center recess orientation and the side taper angle were investigated for optimization. The results show that rotating the

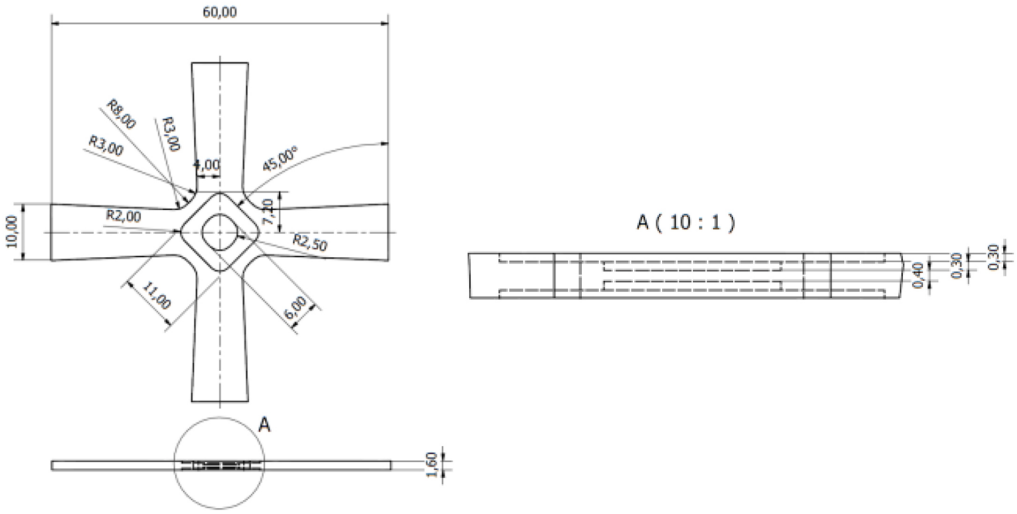

Figure 3.14: The cruciform specimen (mm) designed by Lee et al. [100]

square recess at 45° relative to the axes of the spokes minimizes the influence of the specimens corners and hence alleviates the stress concentration problem at the corners. The side taper angle is not likely to be advantageous for specimens with a center recess since the later feature inherently shifts deformation closer to the center of the specimen. Nearly uniform strain accumulation is achieved in some specimens, particularly a cruciform specimen with a square recess with edges rotated through 45° relative to the axes of the arm.

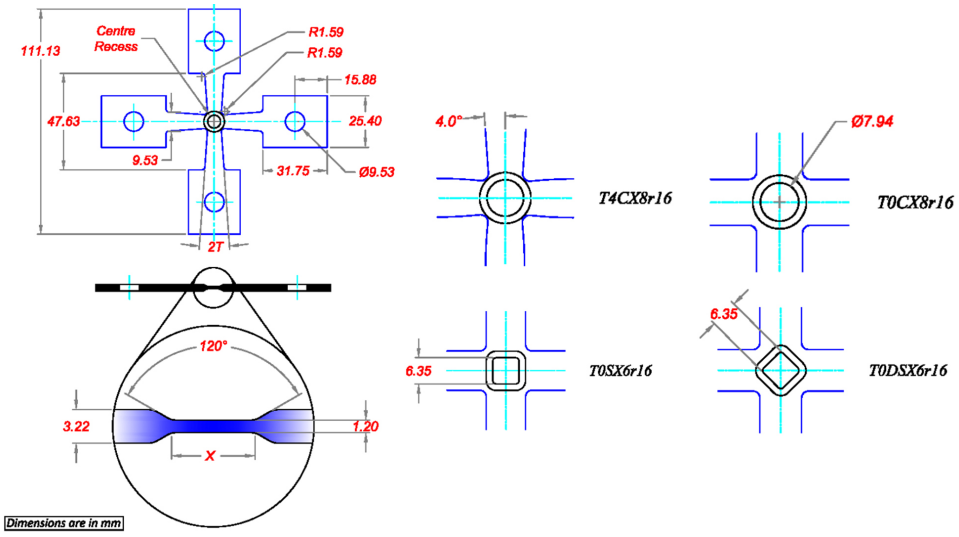

Figure 3.15: Different central zones designed by Abbassi et al. [101]

Zidane [73] has proposed a dedicated cruciform shape (Figure 3.16) and two steps of thickness reduction have been adopted. It is indicated that the use of a cruciform shape can be an interesting alternative method to plot experimental or numerical

forming limit curves. For linear strain paths, the comparison of experimental results with the ones from a classical Marciniak test shows a very good correlation.

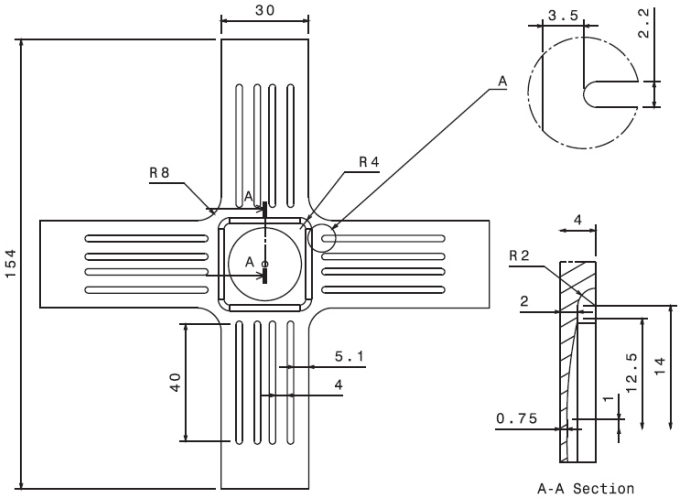

Figure 3.16: The cruciform specimen designed by Zidane [73]

Zidane [73] has investigated the influence of thickness and shape of reduced zone on the forming limits at necking for the AA5086 sheet metal with an original sheet thickness of 4mm. Different thickness of reduced zone (X=0.75mm, 2mm and 3mm) in the uniaxial tensile specimens are considered and the effect of thickness of reduced zone on the forming limit strain are compared. The results show that there is a small decrease in the forming limits at necking with the reduced specimens. The difference of major strain between the non-reduced specimen (4mm) and reduced specimens is 5%. The thickness reduction on two sides and on one side of the specimen are compared with the same thickness of reduced zone (0.75mm). It is shown that there is no effect of the location of thickness reduction on the forming limts at necking. The plane surface and curved surface of reduced zone with the same thickness (0.75mm) are compared. The results show that there is no influence in the forming limits at necking with these shapes.

Xiao et al. [47] have compared two shapes of cruciform specimen (Figure 3.17) for investigating the thermal limit strains of a TA1 titanium alloy. A flat reduced zone is used in the model A while a circular reduced zone is adopted in the model B. The results show that the semispherical thickness reduction design plays a key role in producing the localized neck and fracture in the center.

3.2.4 Some conclusions for designing cruciform specimen

Based on the analysis of previous researches, the following rules have to be considered to design a cruciform specimen shape for investigating fracture: (1) the tapered arm

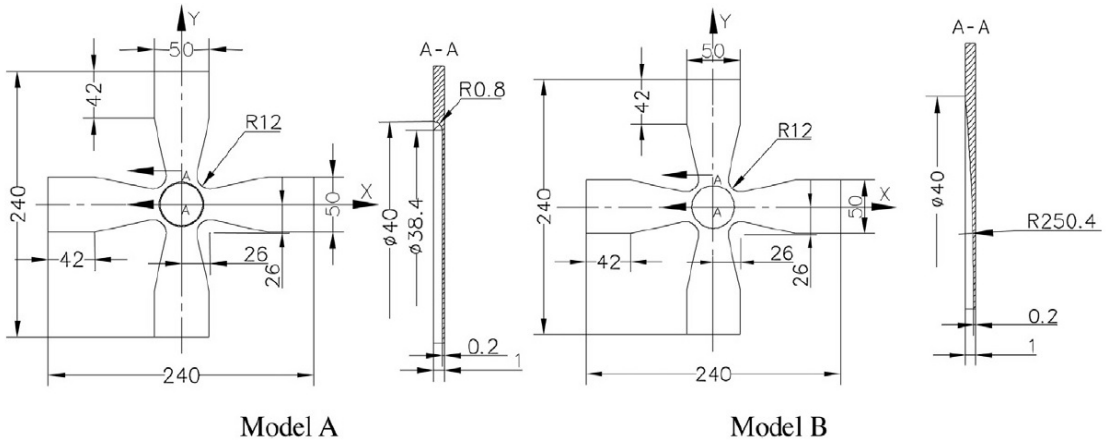

Figure 3.17: Cruciform specimen with circular reduced zone [47]

helps to shift plastic deformation closer to the central zone; (2) the slots in arms are very effective in making the strain distribution in the central zone almost uniform. Narrow, multiple and equally spaced slots are preferable for homogeneous strains; (3) the increase of notch depth promotes plastic deformation closer to the central zone; (4) the thickness reduction of central zone is essential for the onset of fracture at the central point of specimen.

3.3 Numerical investigations based on four cruciform specimens shapes

3.3.1 Selected and redesigned cruciform shapes

Four cruciform specimens reported in previous literatures [95, 100, 12, 79] are selected due to their potential to develop large strains in the central zone. Figure 3.18 shows the geometries of the redesigned cruciform specimens. These cruciform specimens have been redesigned with the constraints recalled in Table 3.1: the original sheet thickness is fixed to 2 mm for all the shapes, the length of specimen and the width of arm are redesigned by considering the space requirements and loading capacity of the testing machine. The minimal thickness of the central zone is set to 0.75 mm in order to limit early fracture due to small defects produced by the milling process. The radius of circular zone in the center of specimen is fixed to 7 mm by considering the resolution of the camera.

Main characteristics of the proposed cruciform specimen shape are: (1) For the specimen 1, the thickness of the circular zone varies along a circular arc profile in the thickness direction. No slots are adopted in the arms; (2) The central zone of the specimen 2 is a two step thickness-reduced geometry. The shape of the first

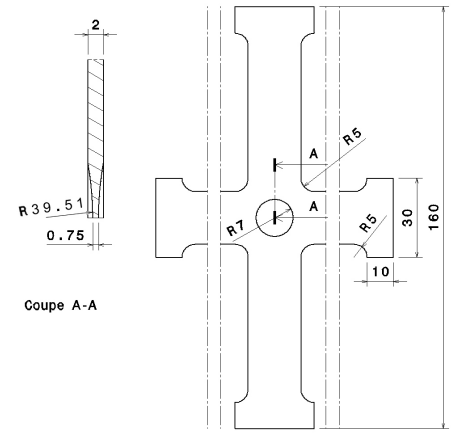

(a) Specimen 1

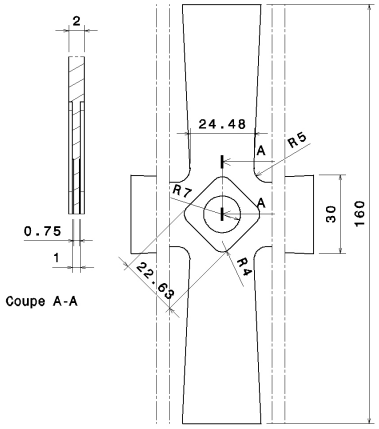

(b) Specimen 2

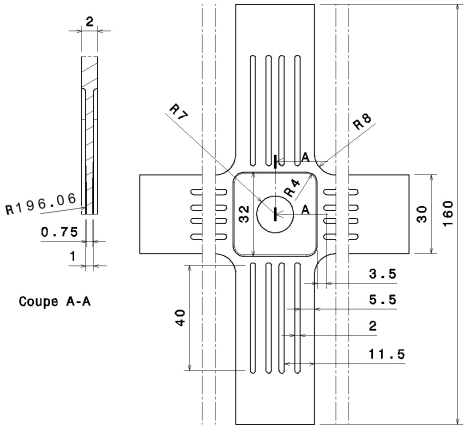

(c) Specimen 3

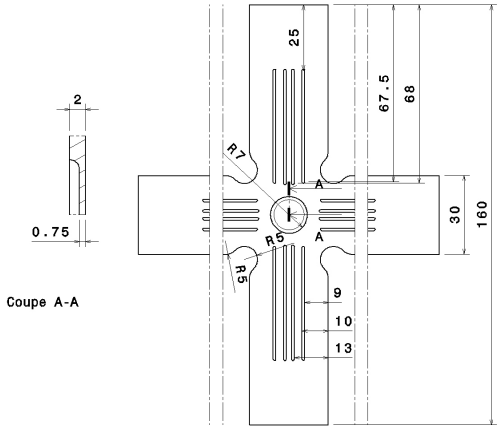

(d) Specimen 4

Figure 3.18: Geometries of redesigned cruciform specimens

thickness reduction is a square with rounded corners and with edges rotated by 45° relative to the axes of arms, while the shape of the second thickness reduction is a circle with flat bottom. Four tapered arms are included; (3) For the specimen 3, the thickness reduction is divided into two steps. The first step of thickness reduction is a square zone with edges paralled to arms and the second step is a circular zone with an arc profile in the thickness direction. Four identical slots are added for each arm; (4) For the specimen 4, the reduced zone is a circle with a flat bottom. Four slots are arranged in each arm around the central zone with different locations for median and outer slots.

Table 3.1: Parameters of the redesigned cruciform specimens

Original thickness of sheet	2 mm
Length of specimen	160 mm
Width of arms	$\leqslant$ 30 mm
Minimal thickness of central zone	0.75 mm
Radius of central zone	$\geqslant$ 7 mm

3.3.2 Numerical models of cruciform specimen

As shown in Figure 3.19, the FE models have been defined with the ABAQUS code for the redesigned cruciform specimens. Considering the symmetrical properties of specimen, only one-quater is modeled for each specimen. Linear tetrahedral solid elements are adopted for the meshes. A refined mesh is defined in the central area. Equibiaxial stretching tests under quasi-static conditions (1 mm/s) are simulated.

3.3.3 Constitutive model of DP600 sheet

In the automotive industry, advanced high-strength steel (AHSS) are adopted for vehicle safety and fuel economy. Dual phase (DP) steel is one type of AHSS, offering superior performance compared with conventional steels by incorporating a multi-phase microstructure-martensite in a ferritic matrix [102, 103]. DP600 sheet is a type of advanced high-strength steels (AHSS) with high strength, ductility and formability [104, 105].

The identification of DP600 steel behavior, subjected to in-plane equibiaxial stretching, was performed in a previous work [106] for a strain rate ranging from quasi-static to intermediate strain rate. The hardening law of DP600 sheet was identified for high strain levels (up to 30%), which makes reliable the calculation of stress field in the range of limit strains. This point will be essential for the numerical evaluation of ductile fracture criteria. Based on the above-mentioned work, the material constants and models used in the present work are briefly recalled hereafter:

Young's modulus of 200 GPa and Poisson's ratio of 0.3 are considered for the elasticity. For the plastic behavior, the associated normal flow rule is assumed and Hill48 yield criterion for plane-stress condition is adopted.

As shown in Table 3.2, the parameters of Hill48 yield criterion for DP600 sheet have been calculated from three anisotropic coefficients proposed by Ozturk et al [107].

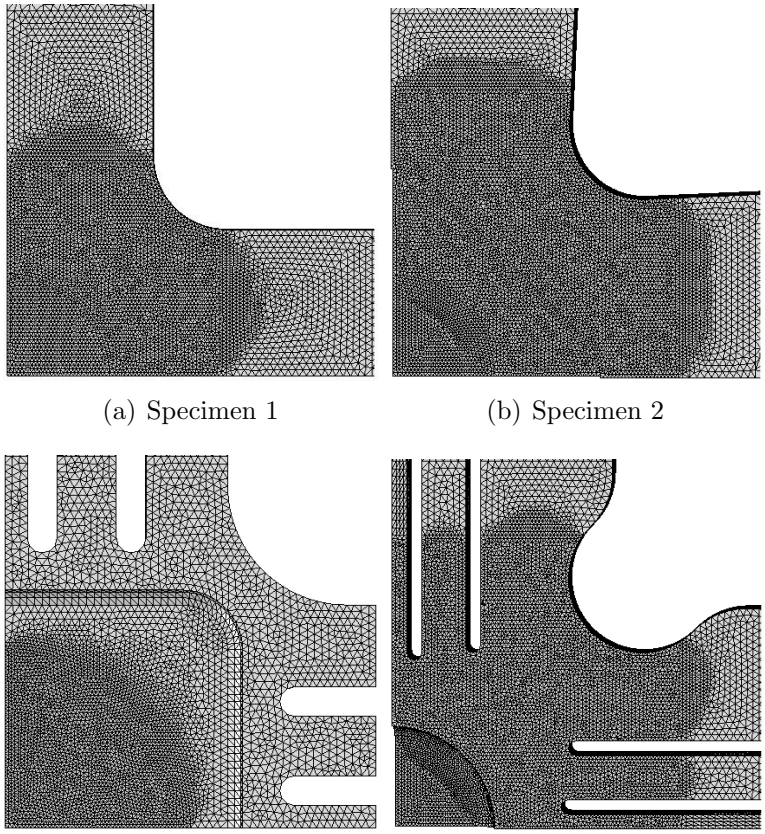

(a) Specimen 1 (b) Specimen 2

(c) Specimen 3 (d) Specimen 4

Figure 3.19: Meshes of redesigned cruciform specimens

Table 3.2: Lankford's coefficient and Hill48 yield parameters

r_0	r_{45}	r_{90}	F	G	H	L	M	N
0.89	0.85	1.12	0.420	0.529	0.471	1.500	1.500	1.282

A rate-dependent hardening law [80] on the basis of Ludwick's law has been used:

$$\bar{\sigma} = \sigma_0 \dot{\bar{\varepsilon}}^{m_1} + K \bar{\varepsilon}_p^n \dot{\bar{\varepsilon}}^{m_2} \tag{3.1}$$

where $\dot{\bar{\varepsilon}}$ is the equivalent strain rate. The parameters σ_0, K , n , m_1 and m_2 are identified by using an inverse procedure with the in-plane biaxial tensile test, as shown in Table 3.3.

3.3.4 Numerical strain fields

To evaluate the performance of each specimen, the following numerical results are given at the moment corresponding to a maximum value of major principal strain

Table 3.3: Identified parameters of the rate-dependent hardening law for Hill48 yield criterion

σ_0 (MPa)	K (MPa)	n	m_1	m_2
339.2	839.7	0.3864	0.0052	0.0158

of 20% inside the specimen. At the same time, fields of both major principal strain (LE) and equivalent plastic strain (PEEQ) and their evolutions along a specified path (path 1 to 4) are analyzed. The aim is to detect strain localizations in the specimen and the potential fracture zones.

Figure 3.20 shows the numerical results of specimen 1. The maximum value of major strain and the maximum value of equivalent plastic strain are all located in the arms. From the evaluations of major strain and equivalent plastic strain along path 1, it can be seen that the major strain is higher in the arms (20%) than in the central point (7%). With such a shape, failure will occur in the arms where an uniaxial tension strain state develops.

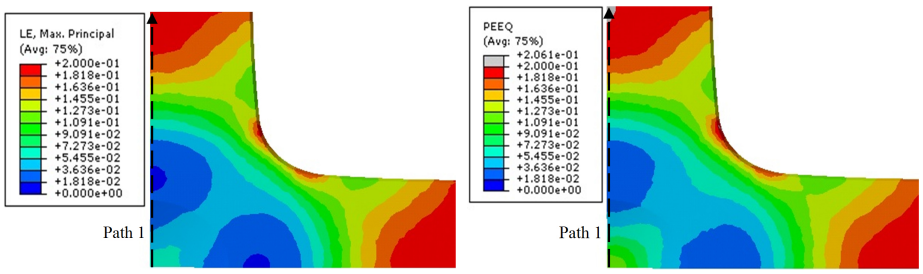

(a) LE (b) PEEQ

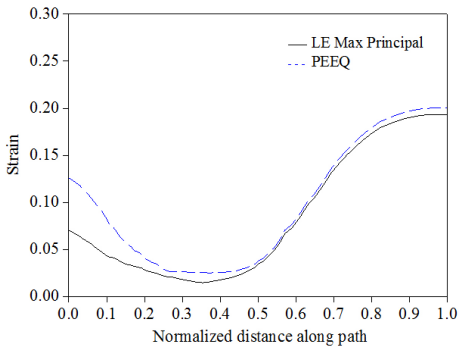

(c) Strain evolution

Figure 3.20: Numerical results of specimen 1

For specimen 2, as observed with strain fields (Figure 3.21 (a) and (b)) and with the strain evolutions along the diagonal path 2 (Figure 3.21 (c)), a homogeneous strain field is reached in the central zone. Unfortunately, the maximum value of

major strain and the maximum value of equivalent plastic strain are localized at the transition zone of arms (under uniaxial tensile state). At the central point, the maximum value of major strain is 6%. The equivalent plastic strain presents two rapid changes at the transition between two zones with different thickness. In this case, the failure will happen at the corner radius between two arms.

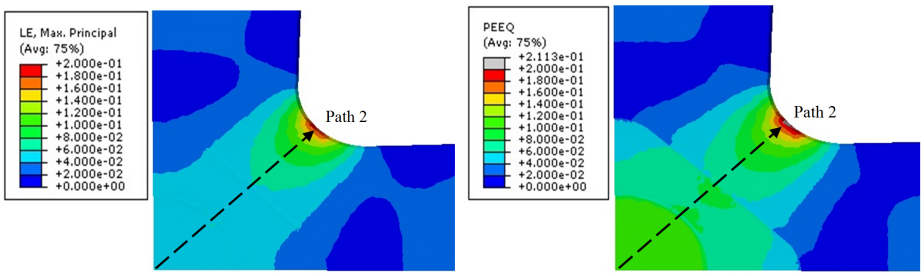

(a) LE (b) PEEQ

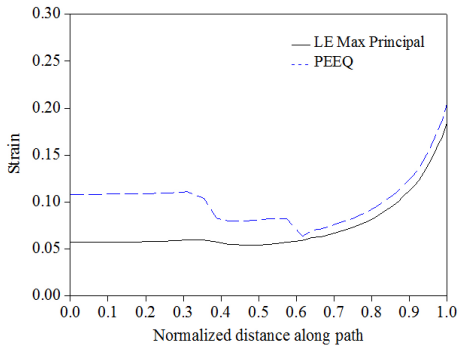

(c) Strain evolution

Figure 3.21: Numerical results of specimen 2

For specimen 3 (Figure 3.22), the maximum value of major strain is reached at the slot tip (under uniaxial tension). At the same time, an equivalent plastic strain of 18% is reached at the central point under equibiaxial stretching. So for this shape, the fracture will probably initiate at the end of slot (see Figure 3.22 (c)) where the major strain is higher than the one at the central point.

Figure 3.23 shows the numerical results of specimen 4. Both the maximum value of major strain and equivalent plastic strain are located at the slot tip. As observed along the path 4, the major strain is much higher at the slot tip (20%) than at the central point (7%). Another strain localization appears in the fillet radius between the flat reduced thickness central zone and the rest of specimen, which may lead to fracture.

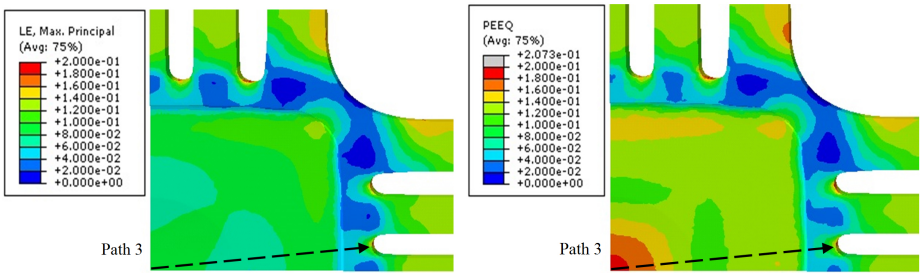

(a) LE (b) PEEQ

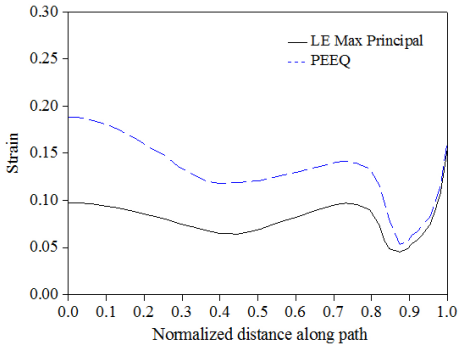

(c) Strain evolution

Figure 3.22: Numerical results of specimen 3

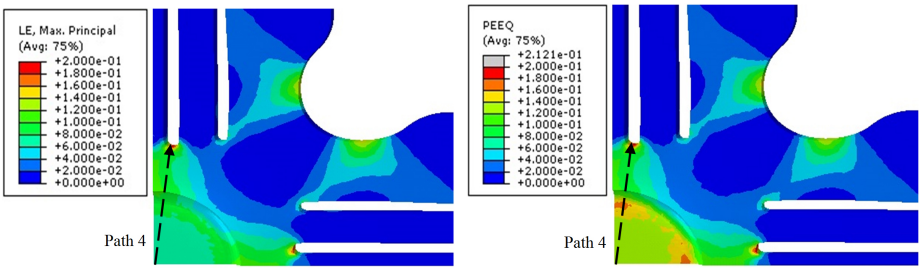

(a) LE (b) PEEQ

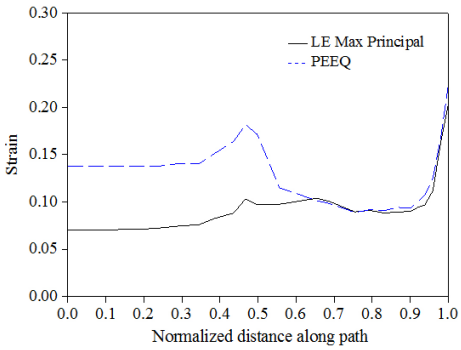

(c) Strain evolution

Figure 3.23: Numerical results of specimen 4

3.4 Optimization of cruciform specimen

Based on the above numerical results, a new shape of cruciform specimen is proposed for obtaining the fracture at the central point (Figure 3.24). For this specimen, a circular reduced thickness central zone with a radius value of 7 mm is chosen. In the thickness direction, a circular profile is adopted to lead strain localization to the central point. A transition of the arms with a radius value of 5 mm is used to reduce the strain localization in this zone. Six slots and a progressive width of arms are used to enhance the strain localization at the central point. D_i (i=1, 2 and 3) represents the distance from the slot tip to the central line of specimen for each slot. W_i indicates the width of arm. The arrangement of slots (D_1, D_2 and D_3) and the widths of arm (W_1 and W_2) will be changed step by step to optimize the cruciform specimen.

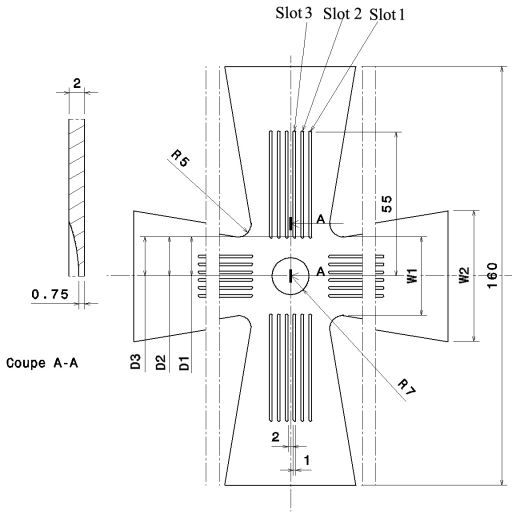

Figure 3.24: Geometry of the proposed cruciform specimen

For the optimization, the equibiaxial stretching is used and the loading speed for each arm of cruciform specimen is fixed at 1 mm/s. The same mesh characteristics and same material constitutive models used in Section 3.3 are chosen for the following section. All the numerical results are given at the moment corresponding to a maximum value of major principal strain of 20% inside the specimen.

3.4.1 Optimization for arrangement of slots

The slots in each arm are produced to reduce the transverse rigidity of arms. The arrangement of slots is important to lead the strain localization to the central point of specimen. As shown in Table 3.4, five specimens (A1 to A5) with different sets

of D_1, D_2 and D_3 (angle θ) for the arrangement of slots are considered. The Angle θ is indicated in Figure 3.25 (b).

Table 3.4: Arrangement of slots with different values of angle θ

No.	D_1 (mm)	D_2 (mm)	D_3 (mm)	Angle θ (^{o})	W_1 (mm)	W_2 (mm)
A1	15	15	15	0	30	50
A2	15	14.5	14	14	30	50
A3	15	14	13	26.6	30	50
A4	15	13.5	12	36.9	30	50
A5	15	13	11	45	30	50

The fields of major principal strain for the specimens with different values of angle θ are shown in Figure 3.25. With increasing the value of angle θ, the deformation is gradually located in the central area.

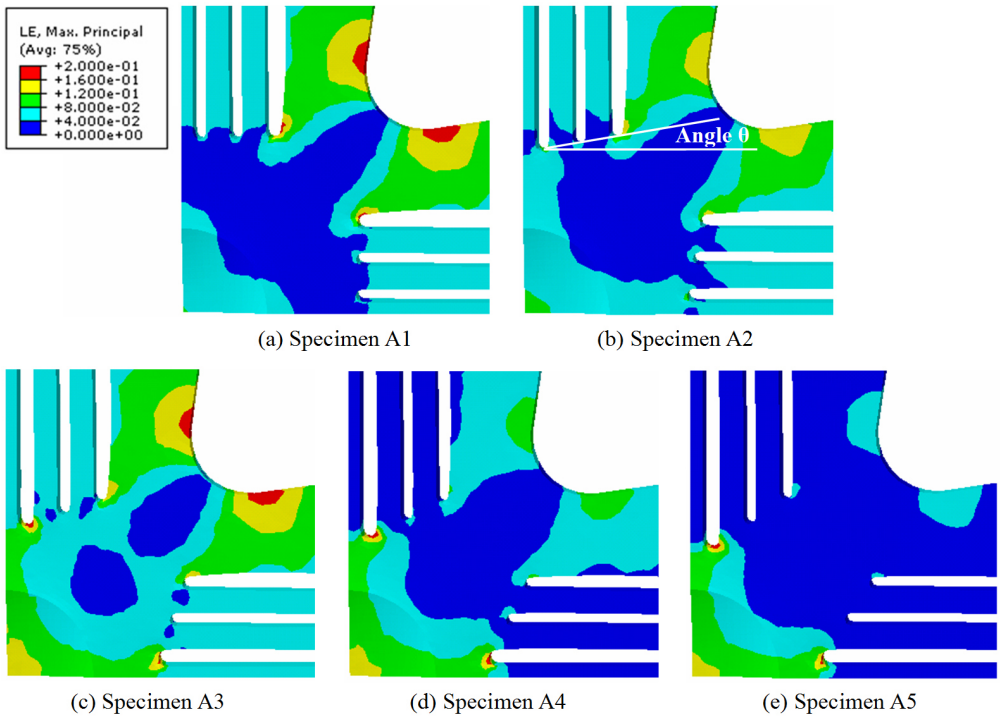

(a) Specimen A1 (b) Specimen A2

(c) Specimen A3 (d) Specimen A4 (e) Specimen A5

Figure 3.25: Fields of major principal strain for the specimens with different values of angle θ

The values of major principal strains at central point, slot and arm are shown in Figure 3.26. For all the specimens, the maximum values of major principal strain are located at slots. Because the value of major principal strain at central point

of specimen A3 is the biggest in those specimens, it is selected for the next step of optimization.

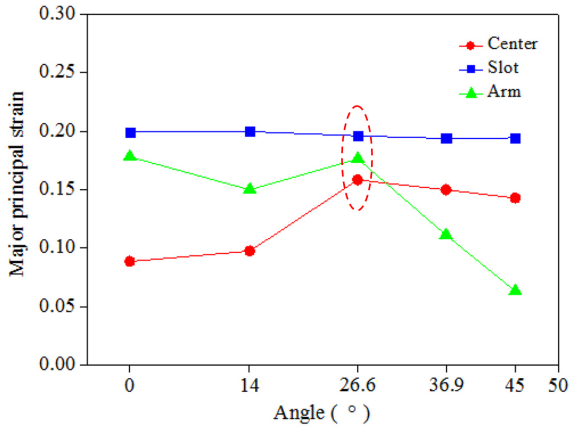

Figure 3.26: Major principal strains in different zones for the specimens with different angles

Different locations of the Slot 2 (D_2 = 13 mm, 13.1 mm, 13.2 mm, 13.3 mm, 13.4 mm and 13.5 mm) are considered to find the optimized arrangement of slots. The fields of major principal strain for the specimens with different values of D_2 are shown in Figure 3.27. For the specimen A8 and A9, a little change in the value of D_2 can lead to a different field of major principal strain.

Table 3.5: Arrangement of slots with different values of D_2

No.	A6	A7	A8	A9	A10	A11
D_2 (mm)	13	13.1	13.2	13.3	13.4	13.5

The values of major principal strains at central point, slot and arm are shown in Figure 3.28. The specimen A9 is selected for the next step of optimization due to the biggest value of major principal strain at the central point. However, for the specimen A9, the major principal strain at arm is also very high. For the next step of optimization, the strain level in arms should be decreased.

3.4.2 Optimization for arm shape

Tapered arm

For decreasing the strain level at arms near to the transition zone, the shape of tapered arm is considered to change. As shown in Table 3.6, the value of W_1 is fixed to 30 mm and different values of W_2 are used to produce various shapes of arm.

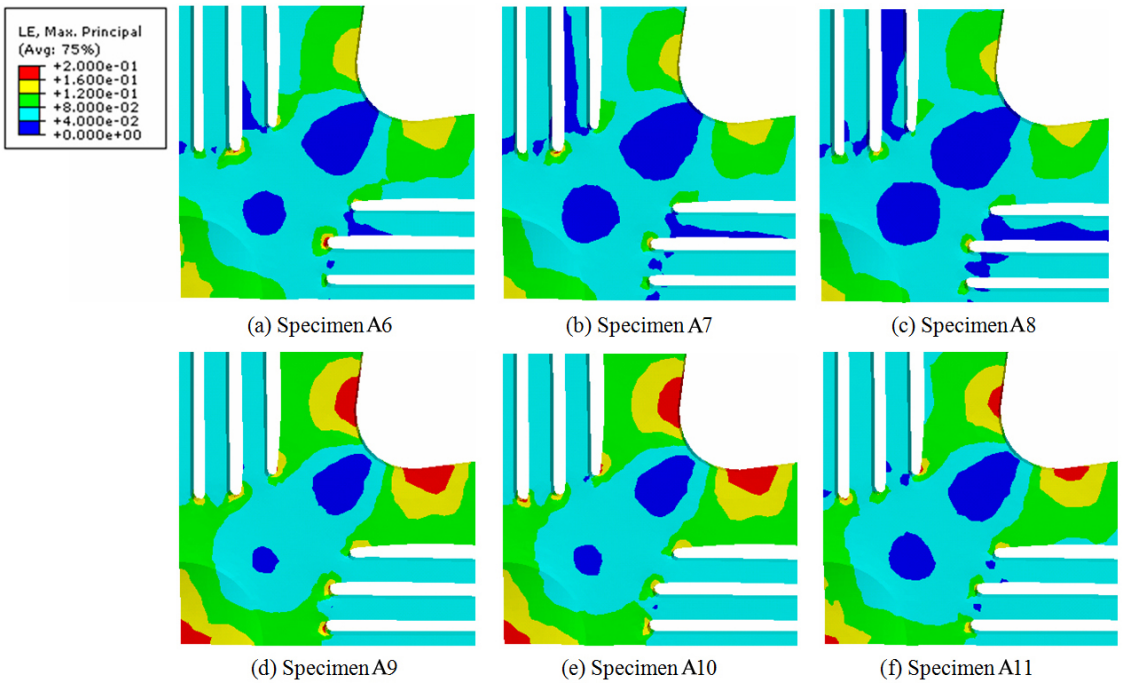

Figure 3.27: Fields of major principal strain for the specimens with different values of D_2

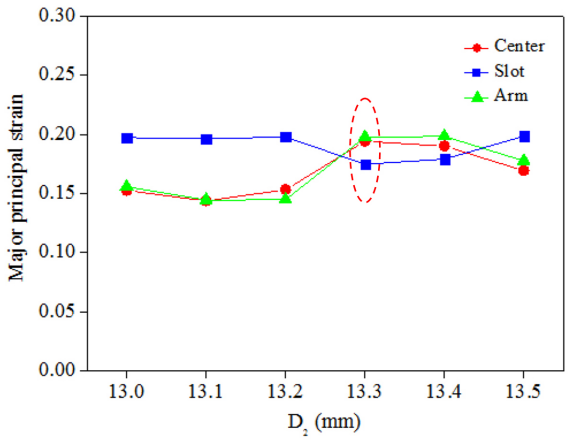

Figure 3.28: Major principal strains in different zones for the specimens with different values of D_2

Table 3.6: Different values of W_2 for the arm shape

No.	S1	S2	S3	S4	S5
W_2 (mm)	50	45	40	35	30

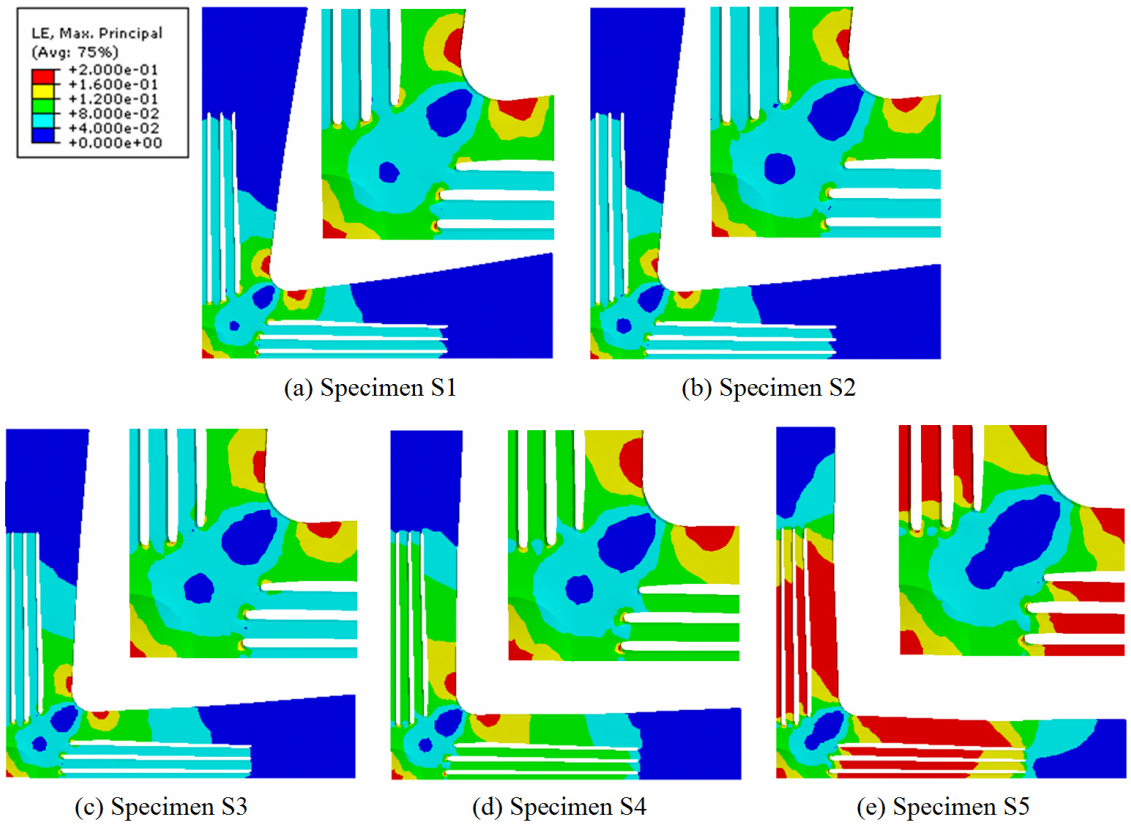

(a) Specimen S1 (b) Specimen S2

(c) Specimen S3 (d) Specimen S4 (e) Specimen S5

Figure 3.29: Fields of major principal strain for the specimens with different values of W_2

As shown in Figure 3.29, there are two strain localizations in the transition zone of arms when $W_2 > W_1$ (Specimen S1, S2, S3 and S4). The strain in arm becomes more uniform when $W_2 = W_1$ (Specimen S5). As shown in Figure 3.30, it can be seen that the major principal strain reaches 20% at the central point of specimen when $W_2 = W_1$. However, the strain level in arm is also very high. The specimen A9 with a constant arm ($W_1 = W_2 = 30$ mm) is selected for the next step of optimization and the strain level in arms for this specimen needs to be decreased.

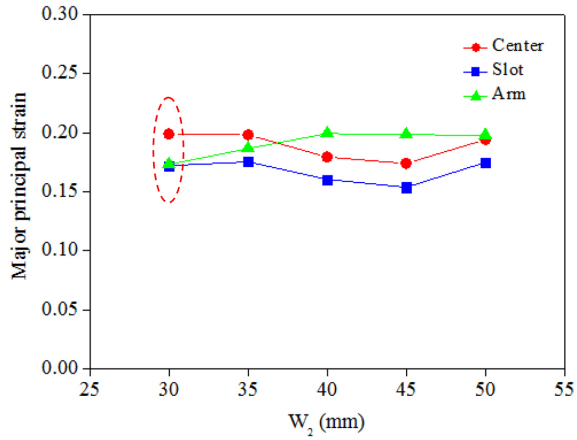

Figure 3.30: Major principal strains in different zones for the specimens with different values of W_2

Constant width arm

As shown in Table 3.7, different values of W_1 and W_2 are used to produce different widths of constant width arm, which aims to reduce the global strain level.

Table 3.7: Different values of W_1 and W_2 for the arm shape

No.	S5	S6	S7	S8	S9
W_1 (mm)	30	32	34	36	38
W_2 (mm)	30	32	34	36	38

The fields of major principal strain at the central point, slot and arm are shown in Figure 3.31. It can be observed that the strain field changes a lot with increasing the arm width. As shown in Figure 3.32, the major principal strain at arm decreases obviously with increasing the arm width, while the major principal strain at slot has a small increasing trend. For the specimen S6 or S7 or S8, the strain level is higher at central point than at slot. Except for the specimen S5, the value of major principal strain at arm for each specimen is smallest. It is very hard to reduce the

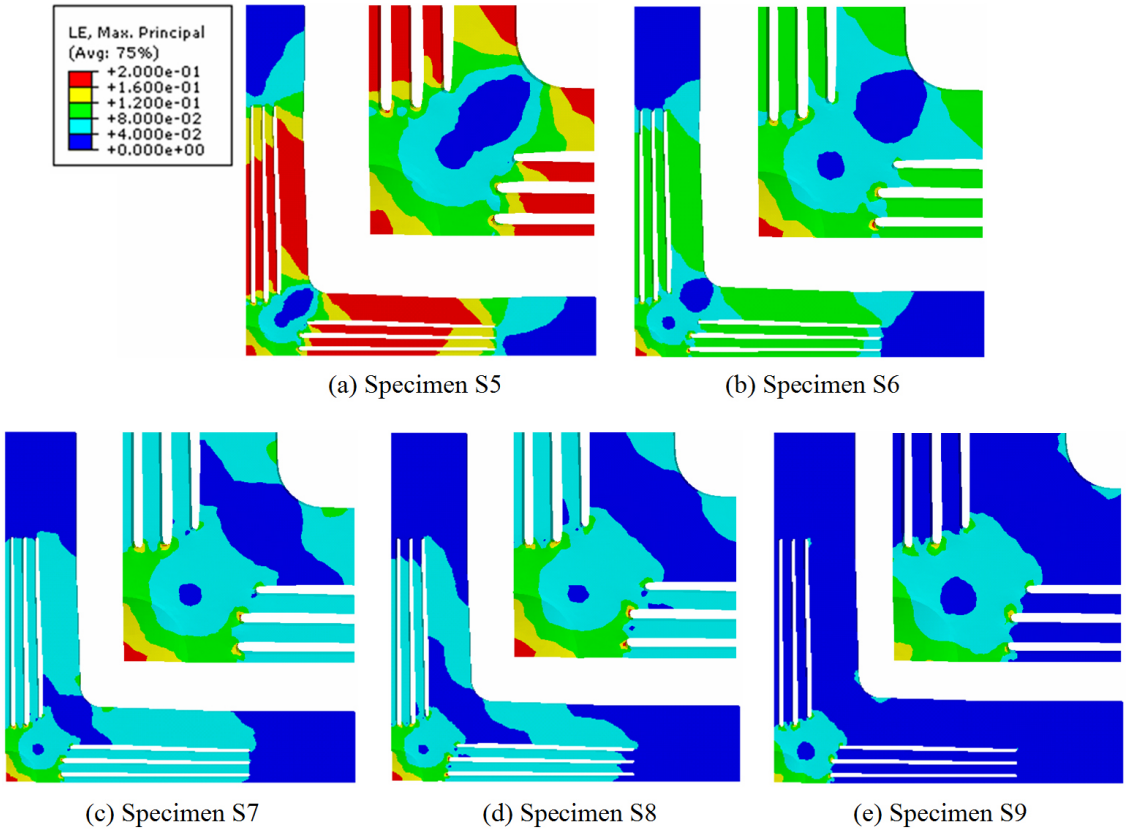

(a) Specimen S5 (b) Specimen S6

(c) Specimen S7 (d) Specimen S8 (e) Specimen S9

Figure 3.31: Fields of major principal strain for the specimens with different values of W_1

strain level at slot, especially at the tip of slot. Among the three specimens: S6, S7 and S8, the specimen S6 presents the better potentiel to obtain fracture at the central point of the cruciform specimen.

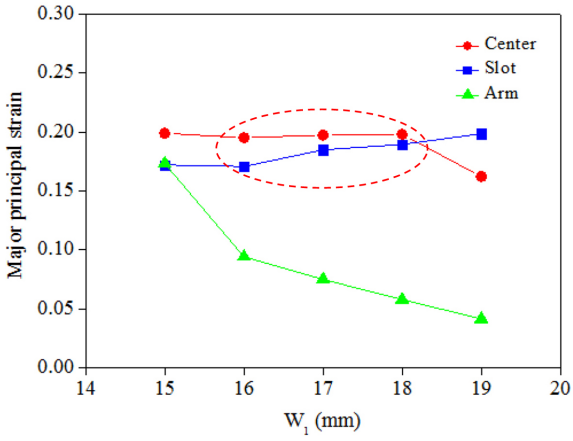

Figure 3.32: Major principal strains in different zones for the specimens with different values of W_1

3.4.3 Validation of the optimized shape for different strain paths

The final geometry of the optimized cruciform specimen S6 is shown in Figure 3.33. Different loading conditions (velocity ratio R of axis X and Y: 0.75, 0.5, 0.25, 0.05 and uniaxial tension) are considered for the optimized specimen. The numerical results are shown in Figure 3.34, in which we can observe the evolutions of different strain paths at the central point of the specimen. A wide range of strain path from equibiaxial stretching to uniaxial tension across plane-strain tension is obtained. Therefore, this optimized cruciform specimen shape presents an interesting potential and will be experimentally evaluated in order to plot the whole FLCN and FLCF of DP600 sheet metal with an original thickness of 2 mm.

Some conclusions can be obtained for the Section 3.4: (1) The arrangement of slot is a key parameter to lead the strain localization to the central point of cruciform specimen. A small change of the location of slot can result in a very different strain field and a careful choice should be considered; (2) The arm shape has an effect on the strain field. Increasing the width of constant arm can reduce the strain level at arm; (3) The optimized cruciform specimen permits to produce different numerical strain paths.

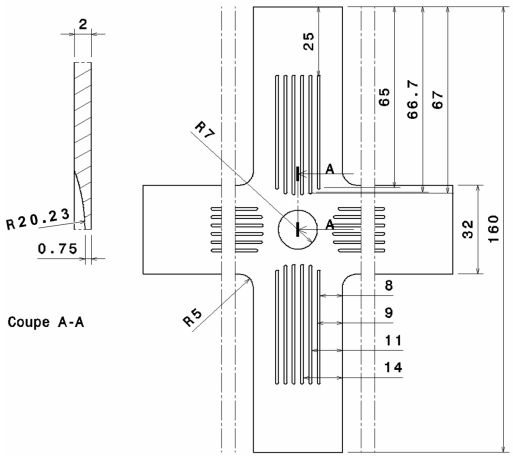

Figure 3.33: Geometry of optimized specimen

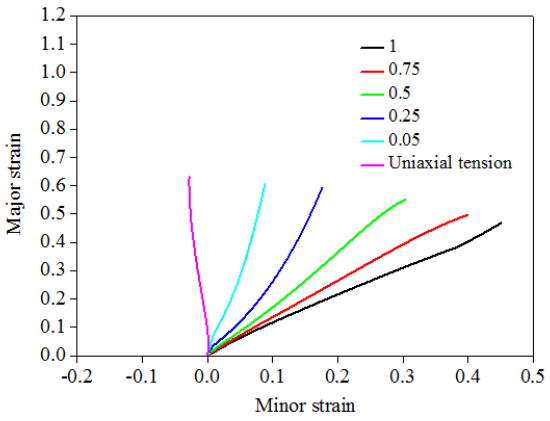

Figure 3.34: Numerical strain paths produced by the optimized specimen

3.5 Effect of thickness reduction on forming limits of DP600 sheet

The original thickness of DP600 sheet is 2mm, while the thickness of the central zone of optimized specimen is 0.75 mm. The effect of thickness reduction for the DP600 sheet on forming limit strains at fracture will be considered.

3.5.1 Thickness reduction for the whole sheet

The whole original sheet thickness is reduced by milling machine to different final thicknesses t. Figure 3.35 shows the dimensions of the uniaxial tensile specimen, in which different final thicknesses (t=2 mm, 1.85 mm, 1.7 mm and 1.3 mm) are considered.

The DIC method is used to evaluate the strain components at the specimen

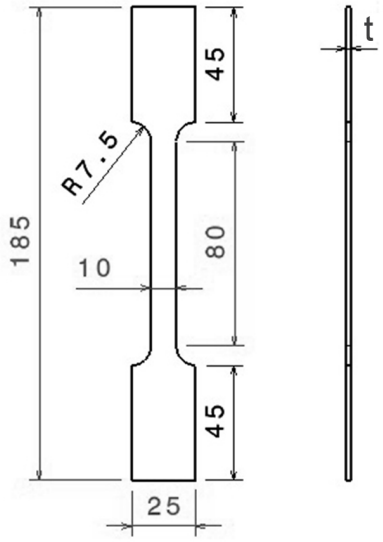

Figure 3.35: Dimensions of the uniaxial tension specimen of DP600 sheet

surface. Figure 3.36 shows the equivalent strain field of the specimen (thickness of 2 mm) at the time 0.02 s before fracture. The dash line indicates the central line and two zones A and B (8×8 mm size) are selected to investigate the strain evolution.

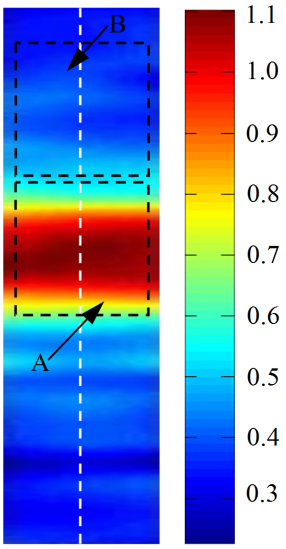

Figure 3.36: Equivalent strain field of the original sheet at the time 0.02s before fracture

The time-dependent method based on the evolution of equivalent strain and the observation of macroscopic image of specimen is used to identify the onset of fracture. As shown in Figure 3.37, the level of equivalent strain of zone A increases with time and an abrupt change can be observed at last of the test. It can be found that the macroscopic crack appears (see Figure 3.38) when the abrupt change of

equivalent strain happens. The time 0.02s before the fracture is used to identify the major and minor strains at fracture.

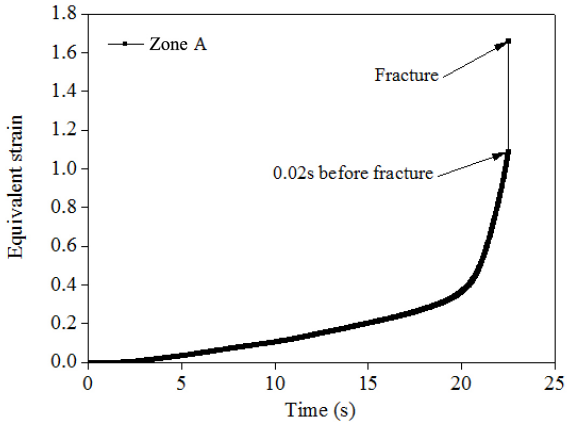

Figure 3.37: Evolution of equivalent strain of zone A

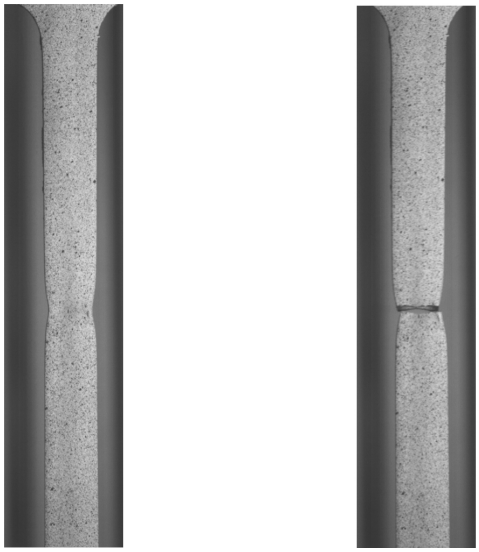

(a) 0.02s before fracture (b) fracture

Figure 3.38: DIC figures of specimen under uniaxial tension

The critical ratio method is used to identify the onset of necking for the uniaxial tensile test. As shown in Figure 3.39, the equivalent strain of zone A increase with time until the onset of fracture, while the equivalent strain of zone B increases with time and then reaches the saturation at one moment, which indicates the onset of necking. The major and minor strains of zone A at the moment of onset of necking are used to define the major and minor strains at necking.

The distribution of major strain along the dash line in Figure 3.36 during the test is shown in Figure 3.40. The deformation develops generally in three stages

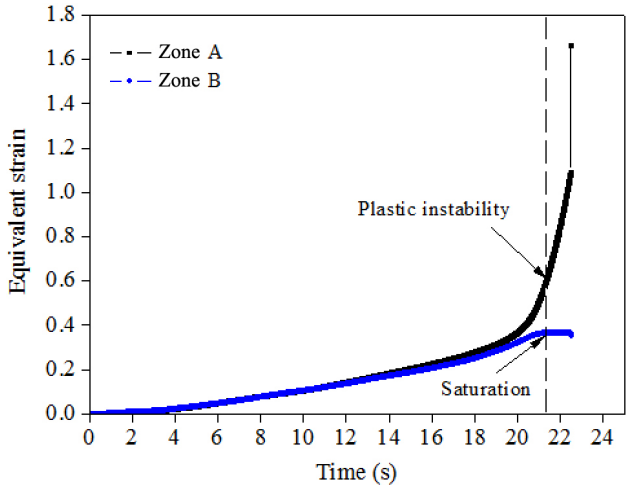

Figure 3.39: Identification of necking for the original sheet under uniaxial tension

during the test: (1) the homogenous deformation, (2) the continuously increasing localization and (3) the final fracture. It can be clearly observed that the plastic region smoothly collapses to a narrow band before the appearance of fracture.

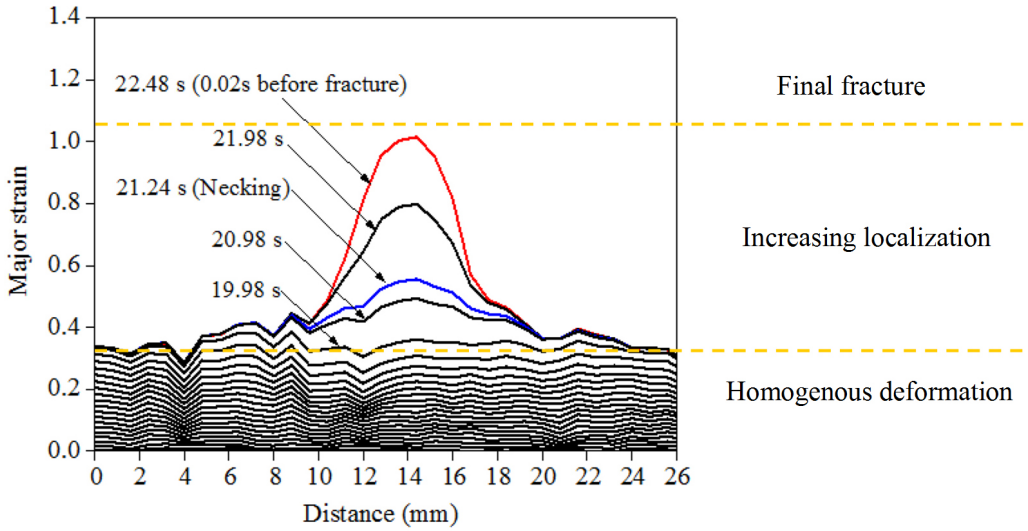

Figure 3.40: Major strain along the longitudinal axis of the specimen during the uniaxial tensile test carried out on the original sheet

Figure 3.41 shows the forming limit strains at necking for the thickness reductions of 0%, 7.5%, 15% and 35% corresponding respectively to final thickness of 2 mm, 1.85 mm, 1.7 mm and 1.3 mm. The thickness reduction has almost no effect on the major strain at necking, while the minor strain at fracture decreases a little with the thickness.

As shown in Figure 3.42, the solid markers and dashed lines represent the forming limit strains at fracture and the strain paths, respectively. It can be observed that

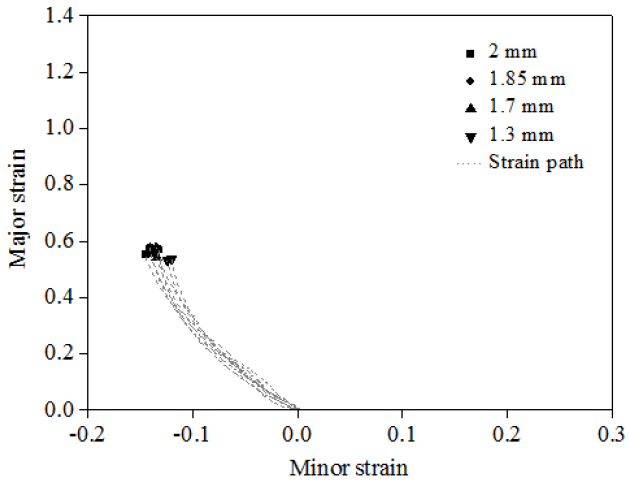

Figure 3.41: Forming limit strains at necking for the DP600 sheet with different thickness

the strain paths are different. For those specimens, the thicknesses are different while the widths are the same, which results in different strain paths. In this figure, the major and minor strains at fracture decrease a little with the thickness.

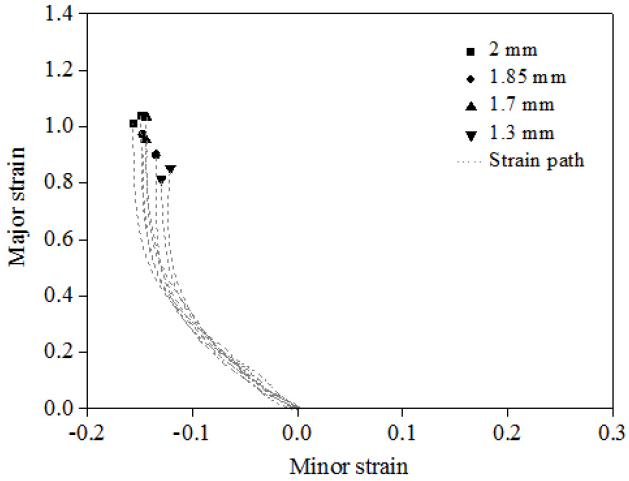

Figure 3.42: Forming limit strains at fracture for the DP600 sheet with different thickness from 2 mm to 1.3 mm

As described in the previous section, the final thickness of the central zone for the optimized cruciform specimen is 0.75 mm. However, for the uniaxial tensile specimen, it is difficult to reduce the 2 mm initial thickness of the whole sheet by classical manufacturing process (milling) up to 0.75 mm. Therefore, in the next section, a partial reduction of the thickness is considered in the central part of the specimen.

3.5.2 Thickness reduction for a partial area of sheet

Figure 3.43 shows the uniaxial tension specimens with a partial reduction of thickness. The influence on the forming limit strain at fracture of three final thickness of 0.75 mm, 1.5 mm and 2 mm in the central zone are investigated.

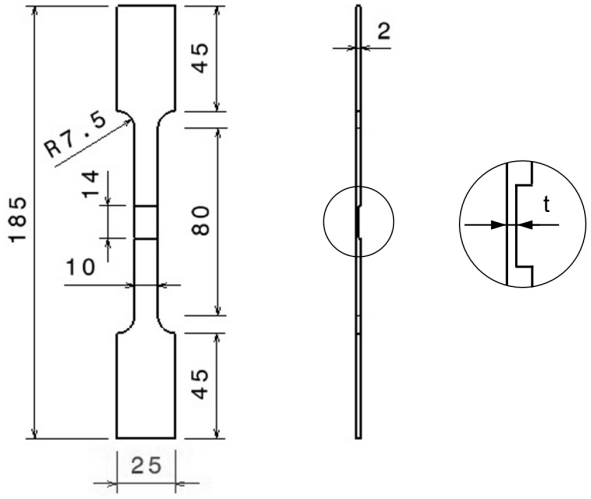

Figure 3.43: Uniaxial tension specimen of DP600 sheet with a partial reduction of thickness

Figure 3.44 shows the forming limit strains at fracture for the thickness of 2 mm, 1.5 mm and 0.75 mm. A small decrease of the level of forming limit strain at fracture can be observed.

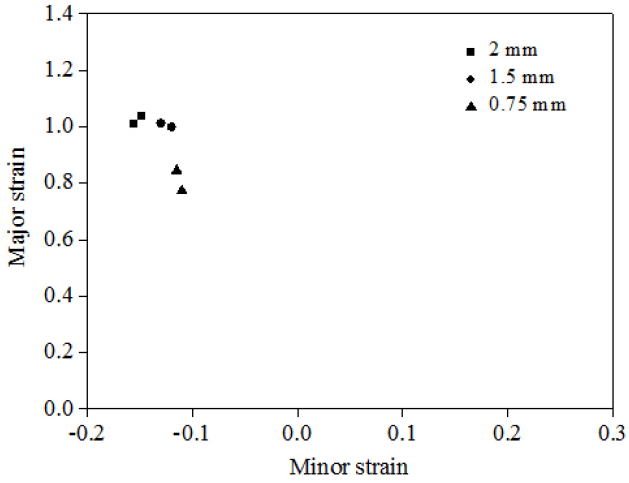

Figure 3.44: Forming limit strains at fracture for the DP600 sheet with different thickness from 2 mm to 0.75 mm

Two conclusions can be obtained for the Section 3.5: (1) The thickness reduction for the DP600 sheet has almost no influence on the forming limit strains at necking; (2) The thickness reduction has a small influence on the forming limit strains

at fracture, but the strain path modification does not allow to conclude an obvious sensibility of the forming limit strains at necking or fracture due to thickness reduction by milling.

3.6 Conclusion

A summary of cruciform specimen shapes for in-plane biaxial tensile test in previous researches has been presented. The following rules have been concluded for designing a cruciform specimen shape for investigating fracture: (1) the tapered arm helps to shift plastic deformation closer to the central zone; (2) the slots in arms are very effective in making the strain distribution in the central zone almost uniform. Narrow, multiple and equally spaced slots are preferable for homogeneous strains; (3) the increase of notch depth promotes plastic deformation closer to the central zone; (4) the thickness reduction of central zone is essential for the onset of fracture at the specimen central point.

Four cruciform specimen have been selected and redesigned. Their potential to reach large strains at the central point of the specimen has been numerically investigated. Based on the numerical results of those specimens, a new shape of cruciform specimen has been proposed and optimized step by step by changing the arrangement of slots and the shape of arm. The optimized cruciform shape permits to produce different numerical strain paths from uniaxial tension to equibiaxial stretching through plane-strain tension.

The effect of thickness reduction on forming limit strains of DP600 sheets has been investigated. The thickness reduction has almost no effect on the forming limit strains at necking, while it has a small influence on the forming limit strains at fracture.

Chapter 4

Characterization and prediction of forming limits of DP600 sheet

Résumé

Dans ce chapitre, la forme d'éprouvette définie au chapitre 3 est utilisée afin de déterminer les déformations limites à striction et à rupture pour des tôles de 2 mm d'épaisseur d'un acier Dual Phase (DP600) utilisé dans l'industrie automobile. Les déformations à rupture sont déterminées par application de la méthode temporelle proposée au chapitre 2.

Tout d'abord, la CLFR et la CLFS sont déterminées expérimentalement pour des chemins de déformation linéaires. Les résultats obtenus permettent de valider la géométrie de l'éprouvette définie au chapitre précédent, la localisation des déformations apparaissant bien au centre de l'éprouvette. Les déformations expérimentales à rupture peuvent être approximées par une droite et ces déformations sont supérieures à celles obtenues à striction sauf pour le chemin de chargement équibiaxial où la striction n'apparait pas.

Par la suite, deux types de chemin de déformation non-linéaire sont considérés:

-Type 2A: une déformation de traction uniaxiale est tout d'abord appliquée avant un chargement équibiaxial,

-Type 2B: une déformation équibiaxiale est tout d'abord appliquée avant un chargement en déformation plane.

L'ensemble des résultats expérimentaux obtenus pour les différents niveaux de pré-contrainte des chemins non-linéaires 2A et 2B peuvent être approximés par une droite unique. Le changement de chemin de déformation a donc peu d'impact sur la CLFR expérimentale.

Pour les résultats à striction, une pré-déformation en traction uniaxiale suivie par une traction équibiaxiale peut améliorer la déformation limite, alors qu'une pré-déformation équibiaxiale suivie d'un chargement en déformation plane n'a que peu d'influence sur la déformation limite à la striction.

Concernant les modèles de rupture ductile présentés au chapitre 1, le critère d'Oyane, à deux paramètres, permet de prédire de manière satisfaisante les résultats expérimentaux à la fois sous des chargements linéaires et non-linéaires.

4.1 Introduction

In this chapter, the optimized cruciform specimen in chapter 3 is used to identify the forming limits of DP600 sheet with an original thickness of 2 mm. Firstly, the experimental FLCF and FLCN under linear strain paths are investigated in Section 4.2. Then, two types of non-linear strain paths are considered for the experimental FLCF and FLCN in Section 4.3. The experimental results under linear and non-linear strain paths are compared in Section 4.4. Lastly, the predictive FLCFs under linear and non-linear strain paths are investigated by using different ductile fracture criteria in Section 4.5.

4.2 Formability of DP600 sheet under linear strain paths

4.2.1 Experimental characterization for FLCF

Different strain paths are considered to obtain the whole FLCF and FLCN for DP600 sheet. Table 4.1 shows the velocity ratios of actuators for the strain paths from equibiaxial stretching to uniaxial tension through plane-strain tension. The axis X corresponds to the rolling direction of the DP600 sheet. For each strain path, two tests are considered.

Table 4.1: Velocity ratios of actuators for different strain paths

Velocity ratio R	1	0.5	0.25	0.05	uniaxial tension
Velocity in axis X (mm/s)	1	1	1	2	1
Velocity in axis Y (mm/s)	1	0.5	0.25	0.1	free

For each test, the generation of speckle pattern is performed on the plane surface of central zone on the side of the specimen without machining. The time-dependent method presented in section 2.3 is used to identify the onset of fracture for DP600 specimen. The equivalent strain field of the central area of DP600 specimen at the time 0.004s before fracture is presented in Figure 4.1 for uniaxial tension. The dashed circle shows the thickness reduced zone on the other side of the specimen. The evolution of equivalent strain of zone A (2.4 × 2.4 mm) is plotted in Figure 4.2. The onset of fracture (Figure 4.3) can be identified based on the above two figures.

As shown in Figure 4.4, experiments are produced out under different strain paths from uniaxial tension to equibiaxial stretching through plane-strain tension.

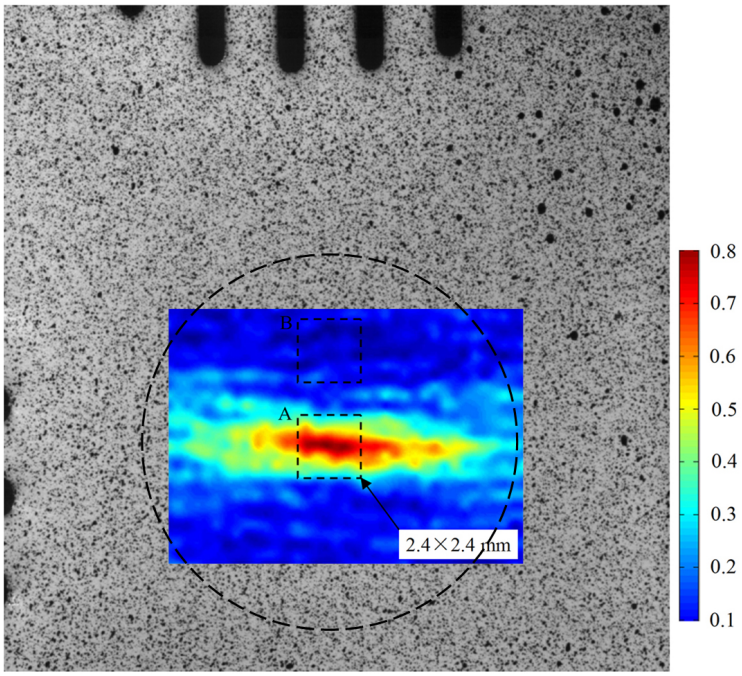

Figure 4.1: Equivalent strain field of central area of DP600 specimen at the time 0.004s before fracture under uniaxial tension

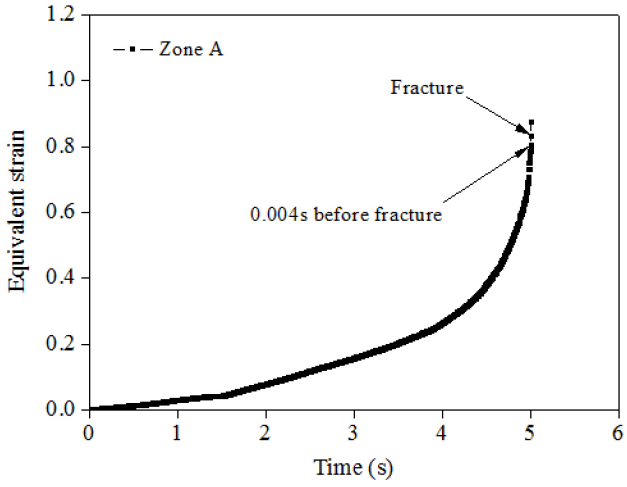

Figure 4.2: Identification of fracture for DP600 specimen under uniaxial tension

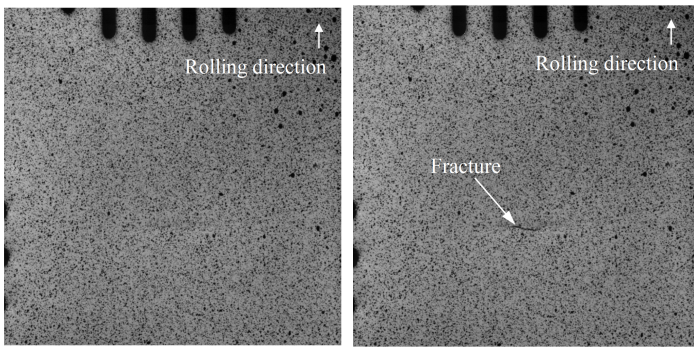

(a) 0.004s before fracture (b) fracture

Figure 4.3: DIC figures of DP600 specimen surface under uniaxial tension

The solid markers and dashed lines represent the forming limit strains at fracture and the quasi-linear strain paths, respectively.

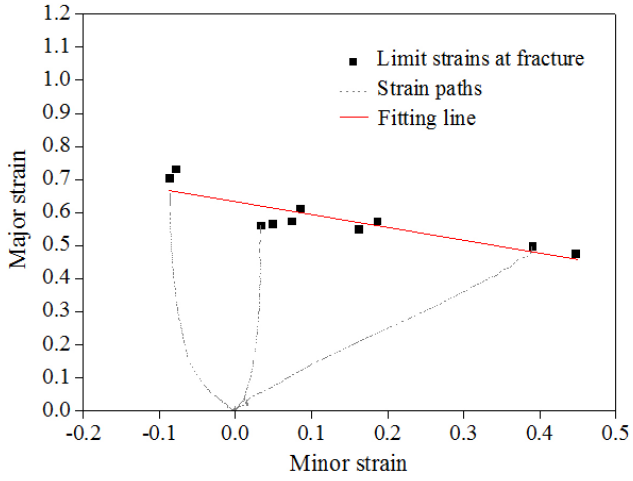

Figure 4.4: Forming limit strains at fracture of DP600 sheet under different linear strain paths

As shown in the above figure, the forming limit strains at fracture of the DP600 sheet metal are fitted by the Fracture Forming Limit Line. The least-square method (4.1) is considered for the fitting process and k=-0.39 and A=0.63 (R-square value of 0.73) are obtained.

$$\varepsilon_{major} = k\varepsilon_{minor} + A \tag{4.1}$$

Figure 4.5 shows fractures under different linear strain paths. For all the strain paths, the initial fracture occurs in the center of the cruciform specimen and all the cracks are perpendicular to the rolling direction.

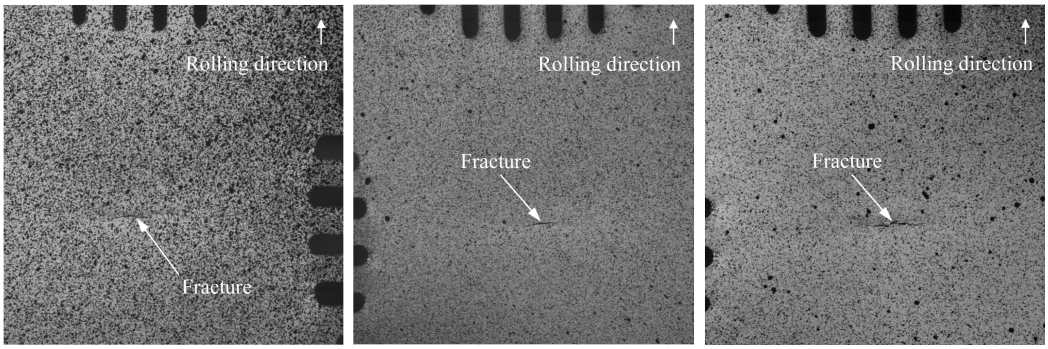

(a) Uniaxial tension (b) Plane-strain tension (c) Equibiaxial stretching

Figure 4.5: Fractures of cruciform specimen under different linear strain paths

4.2.2 Experimental characterization for FLCN

The critical ratio method applied in previous works [27, 108] is used to identify the forming limit strains at necking. As shown in Figure 4.6, when the necking occurs in the central area (Zone A in Figure 4.1), the level of equivalent strain increases abruptly due to the appearance of plastic instability. Outside the necking zone (Zone B in Figure 4.1), the level of equivalent strain stops increase. The equivalent strain increment ratio between zone A and B is defined as a critical ratio for identifying the onset of necking, and the corresponding major and minor strains of zone A define the forming limit strains at necking.

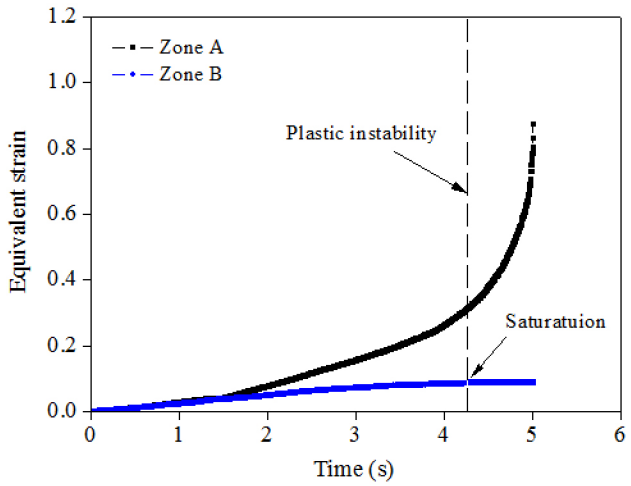

Figure 4.6: Evolution of equivalent strain of zone A and B under uniaxial tension

Figure 4.7 shows the evolution of equivalent strain increment ratio. A critical ratio 8 is considered in this study. This value was used in previous research [12] to identify the onset of necking by using a cruciform specimen.

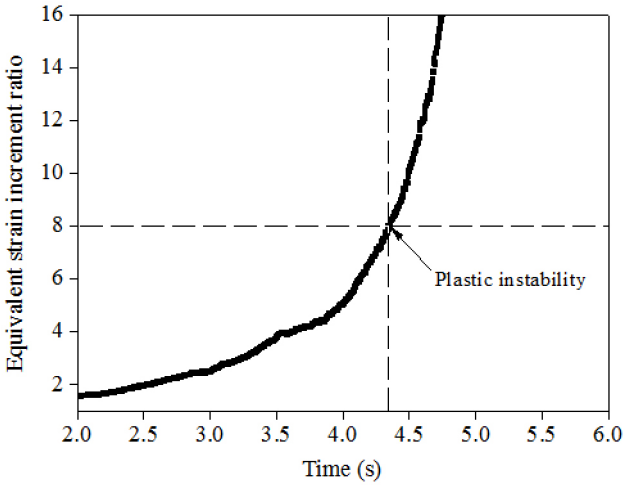

Figure 4.7: Evolution of equivalent strain increment ratio under uniaxial tension

Figure 4.8 shows the forming limit strains at necking under different linear strain paths, which are identified by the critical value of equivalent strain increment value except for the equibiaxial stretching. Dashed lines show the strain paths under uniaxial tension, plane-stain tension and equibiaxial stretching. All the strain paths are quasi-linear for a constant speed ratio. The solid markers represent the forming limit strains at necking.

As shown in Figure 4.9, the same zones (Zone A and B) are used to identify the onset of necking for the equibiaxial stretching. Figure 4.10 shows the evolution of equivalent strains for the two zones. It can be observed that there is no saturation of equivalent strain until fracture for the zone B. Therefore, no necking occurs under the equibiaxial stretching. The forming limit strains at fracture determines the deformation achievable. Under the equibiaxial stretching, ductile fracture due to void formation is induced before onset of localized necking, which results in fracture without appearance of necking. This phenomenon is rather common and was frequently observed in formability identification for aluminium alloys, as reported by Embury et al. [109] for AA5154 sheet or by Takuda et al. [42] for AA5182 sheet.

4.2.3 Comparison of FLCF and FLCN

Figure 4.11 shows the forming limit strains at necking and fracture under different linear strain paths. The forming limit strains at fracture are higher at fracture than at necking, except for the equibiaxial stretching condition. The biggest difference between the FLCF and the FLCN is located near the plane-strain tension.

Some conclusions can be obtained for Section 4.2: (1) The optimized cruciform specimen can be used to produce different experimental linear strain paths; (2)

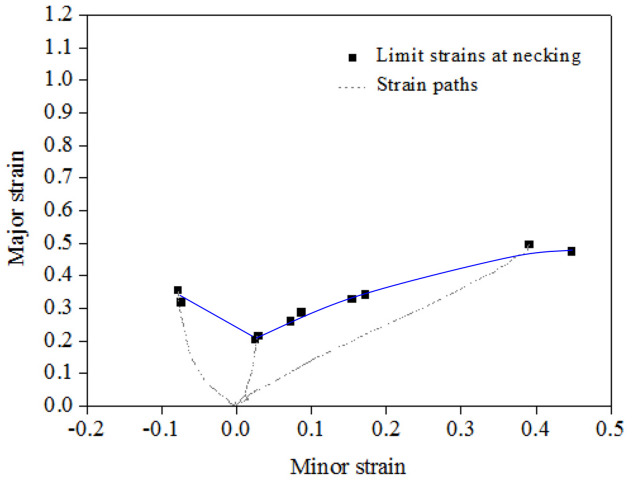

Figure 4.8: Forming limit strains at necking of DP600 sheet under different linear strain paths

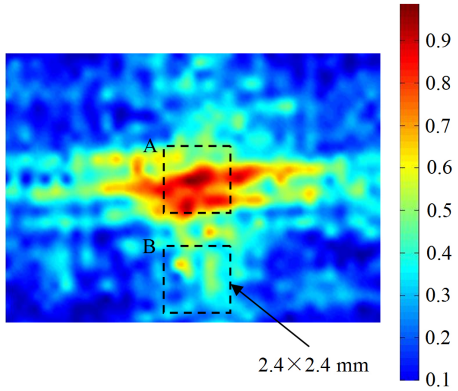

Figure 4.9: Equivalent strain field of central area at the time 0.004s before fracture under equibiaxial stretching

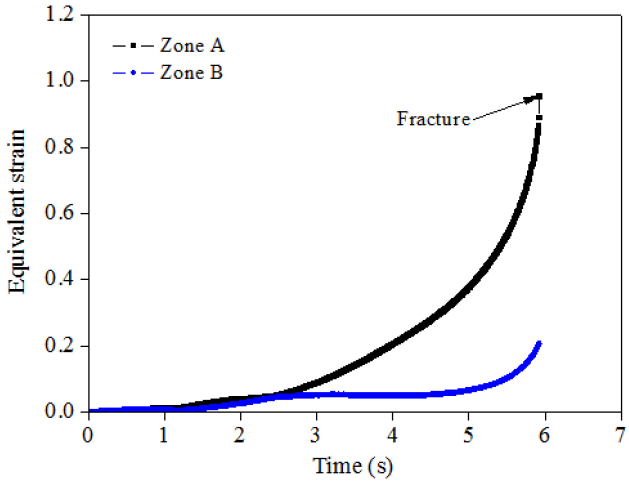

Figure 4.10: Evolution of equivalent strains under equibiaxial stretching

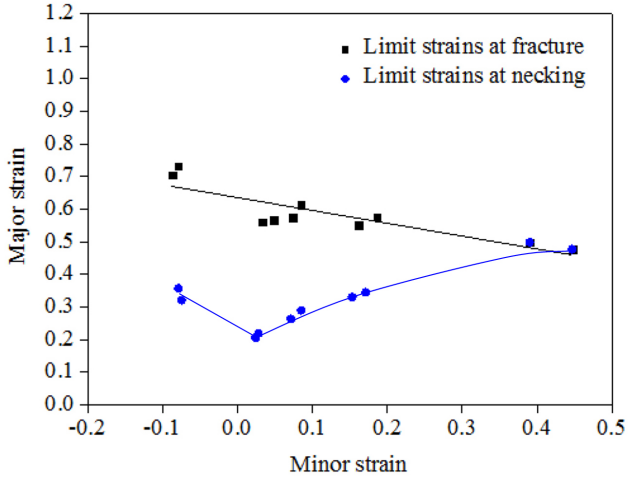

Figure 4.11: Forming limit strains at necking and fracture of DP600 sheet under different linear strain paths

The forming limit strains at fracture of DP600 sheet can be fitted by a straight line; (3) The forming limit strains at fracture are higher than those at necking under different linear strain paths, except for the equibiaxial stretching, in which no necking happens.

4.3 Formability of DP600 sheet under non-linear strain paths

4.3.1 Two types of non-linear strain paths

The type 2 of non-linear strain path in Figure 1.11 is adopted. In detail, two types for the type 2 of non-linear strain path are considered: Type 2-A and Type 2-B. As shown in Figure 4.12 (a), two steps of loading without unloading are used for the type 2-A, in which the first step corresponds to uniaxial tension in the rolling direction of sheet metal and the second step corresponds to equibiaxial stretching. As shown in Figure 4.12 (b), equibiaxial stretching is considered in the first step and the plane-strain tension in the rolling direction of sheet metal is used in the second step for the type 2-B without unloading. For each type of non-linear strain path, different displacements in step 1 are used to produce different levels of prestrain. Table 4.2 shows the details of displacement in step 1 under two types of non-linear strain path.

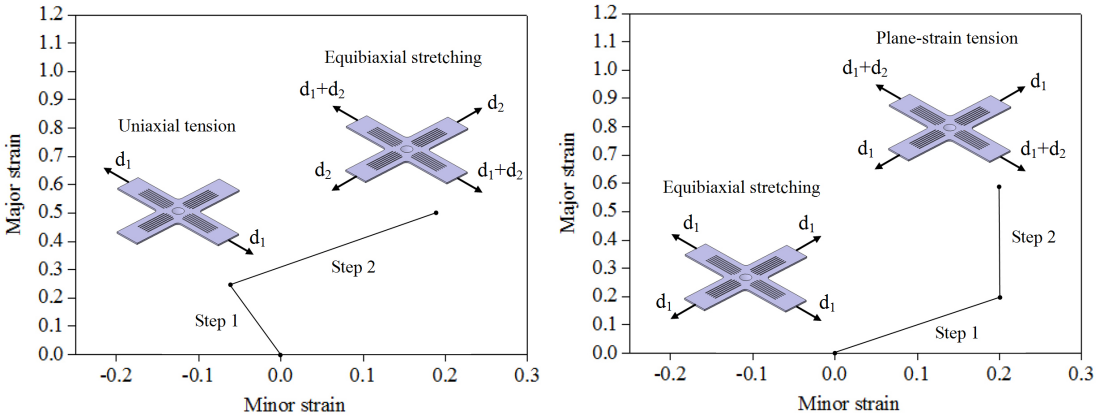

(a) Type 2-A (b) Type 2-B

Figure 4.12: Two types of non-linear strain path

Table 4.2: Different tested displacements for the prestrain stage (step 1)

Type 2-A	Type 2-B
2.0 mm	2.0 mm
2.5 mm	2.5 mm
3.0 mm	3.0 mm
3.5 mm	3.5 mm
4.0 mm	4.0 mm
-	4.5 mm
until fracture	until fracture

4.3.2 Experimental characterization for FLCF

Type 2-A

The time-dependent method is relatively efficient for identifying the onset of fracture and the forming limit strains at fracture of DP600 sheet under different linear strain paths. This method is now applied for determining the forming limit strains at fracture under non-linear strain paths.

For the type 2-A, six pre-displacements from 2.0 mm to until fracture in uniaxial tension (first step) are considered. The identification of onset of fracture and forming limit strains at fracture for the pre-displacements 2.0 mm and 4.0 mm will be presented in details.

Figure 4.13 shows the equivalent strain field of central area at the time 0.004s before the fracture with different pre-displacements in uniaxial tension. The evolution of equivalent strain of zone A for pre-displacements of 2 mm and 4 mm are plotted in Figure 4.14 (a) and (b). It can be observed that the macroscopic crack (Figure 4.15 and Figure 4.16) occurs with an abrupt change of equivalent strain in a very short time (0.004 s) under this type of non-linear strain path. The same phenomenon is observed for the identification of fracture under linear strain paths in previous section.

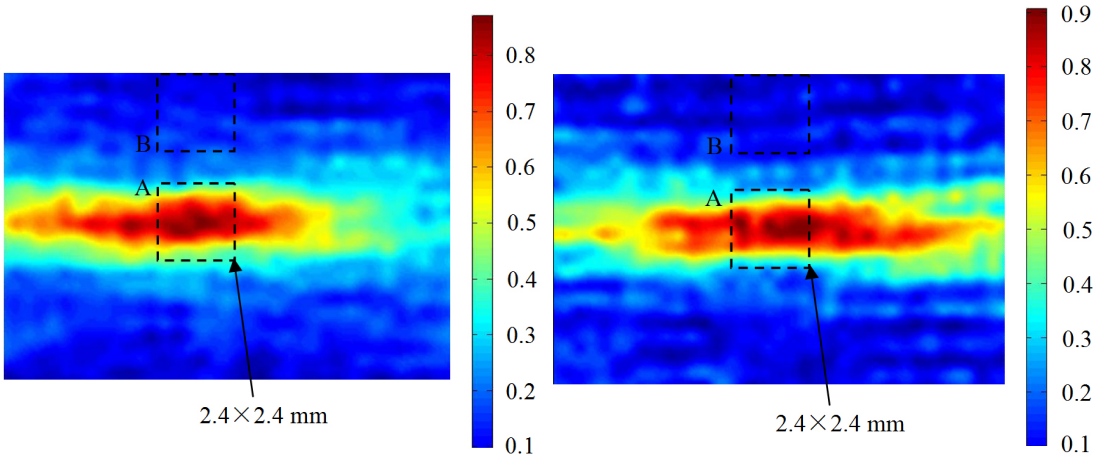

(a) 2.0 mm (b) 4.0 mm

Figure 4.13: Equivalent strain field of central area at the time 0.004s before fracture with different pre-displacements in uniaxial tension

For other pre-displacements (2.5 mm, 3.0 mm, 3.5 mm and until fracture) in uniaxial tension, the same method is adopted to identify the forming limit strains at fracture.

Figure 4.17 shows the forming limit strains at fracture under the type 2-A of

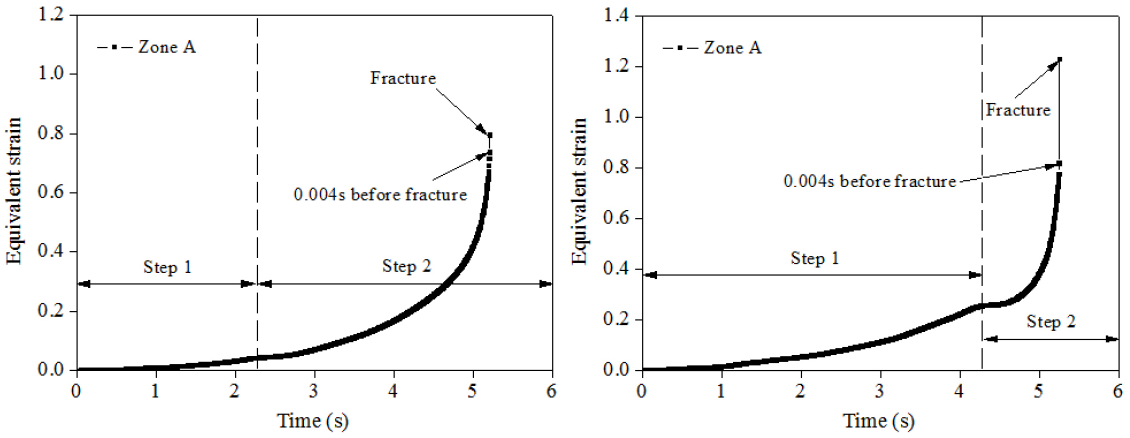

(a) 2 mm (b) 4 mm

Figure 4.14: Identification of fracture for DP600 specimen with different pre-displacement in uniaxial tension

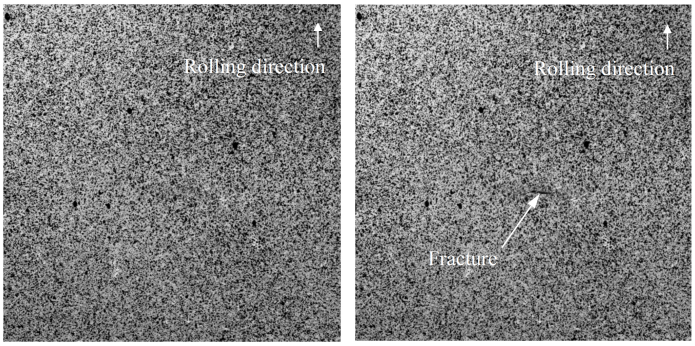

(a) 0.004s before fracture (b) fracture

Figure 4.15: DIC figures of DP600 specimen surface with the pre-displacement of 2.0 mm in uniaxial tension

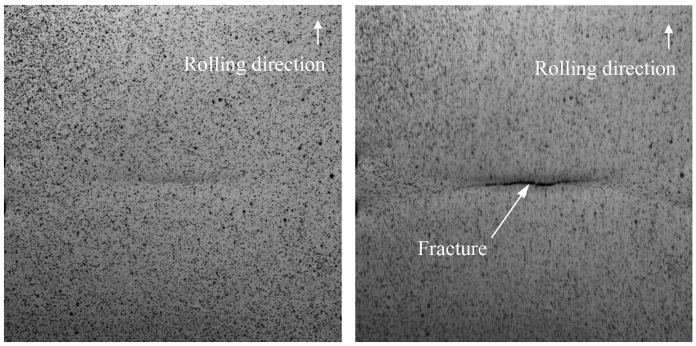

(a) 0.004s before fracture (b) fracture

Figure 4.16: DIC figures of DP600 specimen surface with the pre-displacement of 4.0 mm in uniaxial tension

non-linear strain path. In this figure, the solid markers and dashed lines represent the forming limit strains at fracture and the strain paths, respectively. For the first step of loading, different pre-displacements correspond to different prestrain levels, as shown in Table 4.3. As shown in the figure, the transition between the two steps of loading corresponds to an abrupt change of strain path. With increasing the prestrain from 7% to 27%, the forming limit major strain at fracture increases a little.

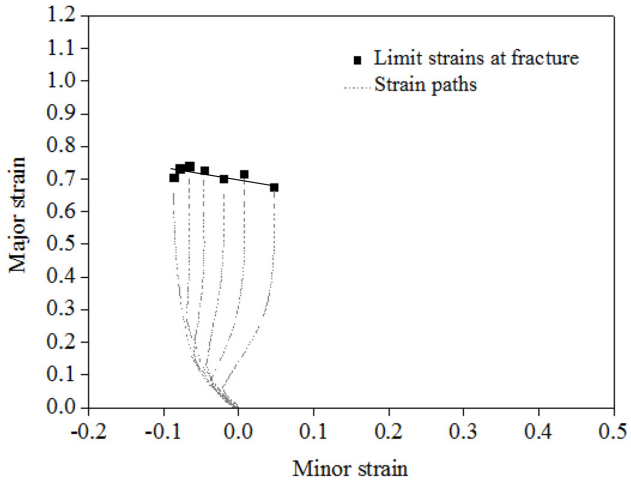

Figure 4.17: Forming limit strains at fracture of DP600 sheet under type 2-A of non-linear strain paths

Table 4.3: Different deformation levels after step 1 of type 2-A

Displacement in step 1 (mm)	2.0	2.5	3.0	3.5	4.0	until fracture
Prestrain level	7%	9%	13%	17%	27%	until fracture

It can be seen that a strain path change exists during the second step of loading. The strain path changes from equibiaxial stretching to plane strain when the prestrain level is under 27%. For the prestrain level of 7%, this strain path change is obvious, which is shown clearly in Figure 4.18. In step 2, the specimen is deformed until fracture. Before fracture happens, the occurrence of necking can result in a change of strain path. However, no obvious change of strain path is observed in step 2 for a high level of prestrain (27%). The strain path changes from uniaxial to plane strain directly after the first step of loading.

Type 2-B

For the type 2-B of non-linear strain path, seven pre-displacements (2.0 mm, 2.5 mm, 3.0 mm, 3.5 mm, 4.0 mm, 4.5 mm and until fracture) in equibiaxial stretching

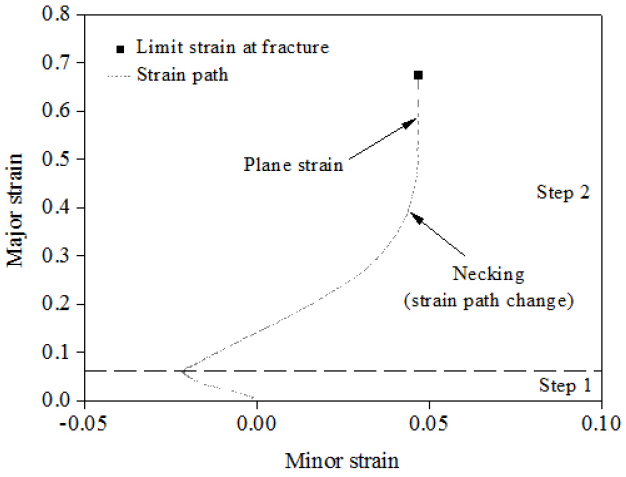

Figure 4.18: Evolution of strain path under loading with a prestrain level of 7% in uniaxial tension

(first step) are considered.

The equivalent strain fields with the pre-displacement of 2.0 mm and 4.0 mm in equibiaxial stretching are shown in Figure 4.19. The evolution of equivalent strain of zone A for the two pre-displacements are plotted in Figure 4.20 (a) and (b). It can be observed that the macroscopic cracks in Figure 4.21 and Figure 4.22 occur with an abrupt change of equivalent strain in a very short time (0.004 s). For other pre-displacements (2.5 mm, 3.0 mm, 3.5 mm and until fracture) in equibiaxial stretching, the time-dependent method is also used to identify the onset of fracture and the forming limit strains at fracture.

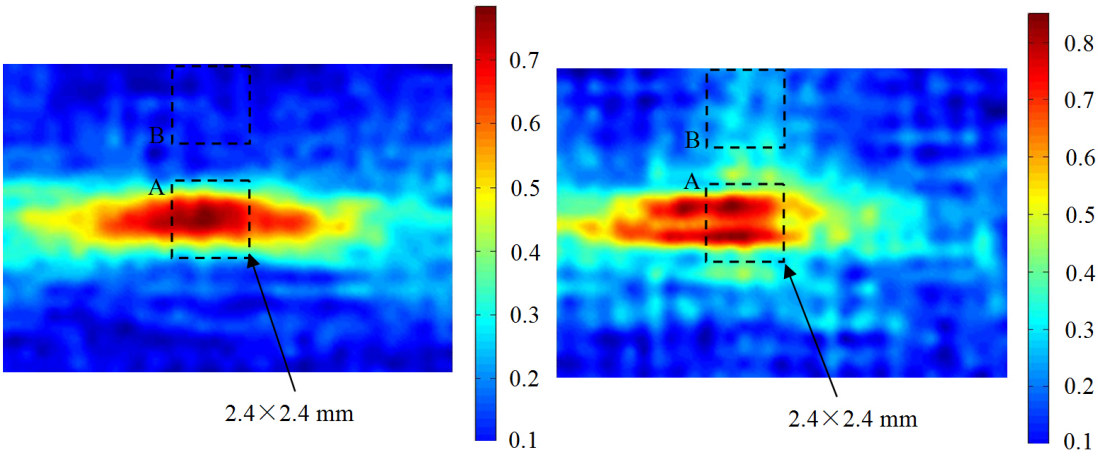

(a) 2.0 mm (b) 4.0 mm

Figure 4.19: Equivalent strain field of central area at the time 0.004s before fracture with different pre-displacements in equibiaxial stretching

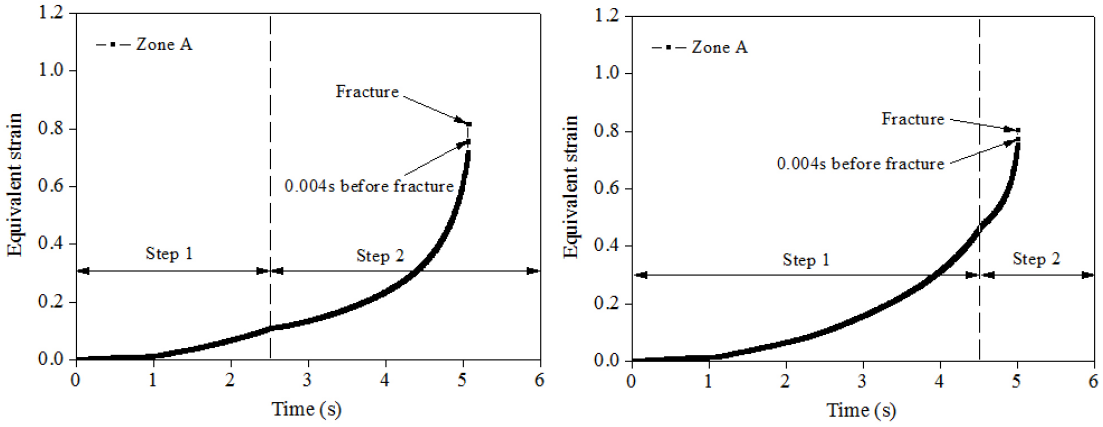

(a) 2 mm (b) 4 mm

Figure 4.20: Identification of fracture for DP600 specimen with different pre-displacement in equibiaxial stretching

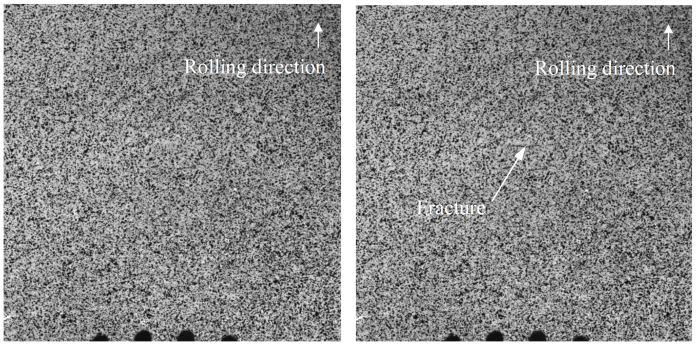

(a) 0.004s before fracture (b) fracture

Figure 4.21: DIC figures of DP600 specimen surface with the pre-displacement of 2.0 mm in equibiaxial stretching

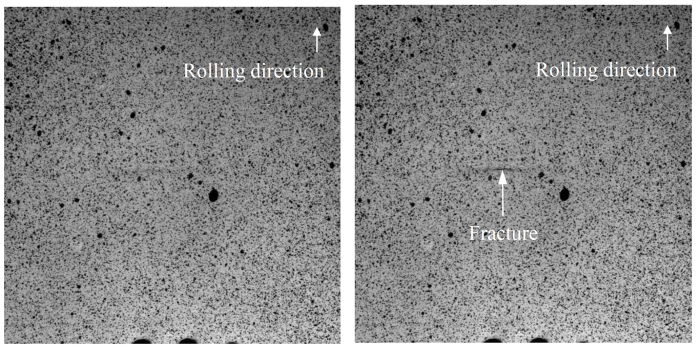

(a) 0.004s before fracture (b) fracture

Figure 4.22: DIC figures of DP600 specimen surface with the pre-displacement of 4.0 mm in equibiaxial stretching

Figure 4.23 shows the forming limit strains at fracture under type 2-B of non-linear strain path. The solid markers represent the forming limit strains at fracture and dashed lines show the strain paths. The prestrain levels produced by different displacements in step 1 are shown in Table 4.4. In the figure, the abrupt change of strain path from equibiaxial stretching to plane strain is obvious for each test. It can be found that the forming limit major strain at fracture decreases with increasing the prestrain from 8% to 38%.

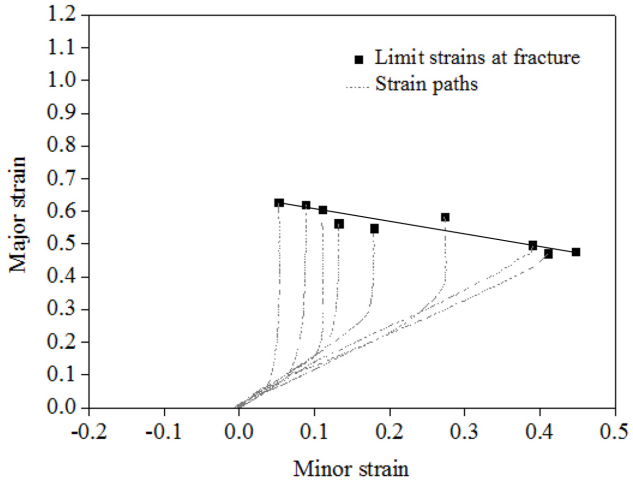

Figure 4.23: Forming limit strains at fracture of DP600 sheet under type 2-B of non-linear strain paths

Table 4.4: Different deformation levels in step 1 of type 2-B

Displacement in step 1 (mm)	2.0	2.5	3.0	3.5	4.0	4.5	until fracture
Prestrain level	8%	10%	15%	22%	30%	38%	until fracture

The forming limit strains at fracture under type 2-A and type 2-B are used to produce a FLCF under non-linear strain paths. As shown in Figure 4.24, a fitting line for all forming limit strains under the two types of non-linear strain paths is obtained by using the least-square method. For this fitting line, k=-0.50 and A=0.68 (R-square value of 0.91) are obtained.

4.3.3 Force evolution

Except for the strain, the force is also an important parameter during the tensile test. Here, the force evolution will be determined and used to identify the onset of fracture.

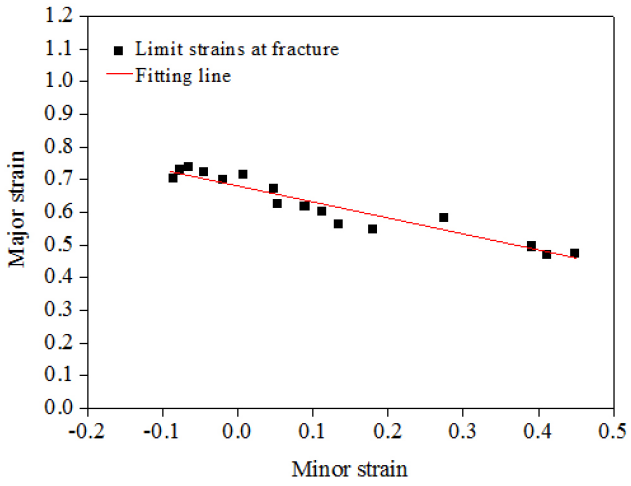

Figure 4.24: Forming limit strains at fracture of DP600 sheet under two types of non-linear strain paths

The pre-displacement of 2 mm in uniaxial tension followed by equibiaxial stretching is taken as an example. The zone A in Figure 4.13 (a) is adopted to investigate the force evolution.

As shown in Figure 4.25, the force in axis X increases with the time after the beginning of test, while it decreases abruptly at one moment in step 2 of loading. The force in axis Y increases after 2 s later of the beginning and an abrupt decrease is also observed. This 2 s leads to 2 mm of displacement in axis X. As described in the time-dependent method for identifying the onset of fracture, the equivalent strain increases with time and an abrupt decrease is observed when the fracture happens. A detail analysis for the relationship between the force evolution and the equivalent strain evolution needs to be performed.

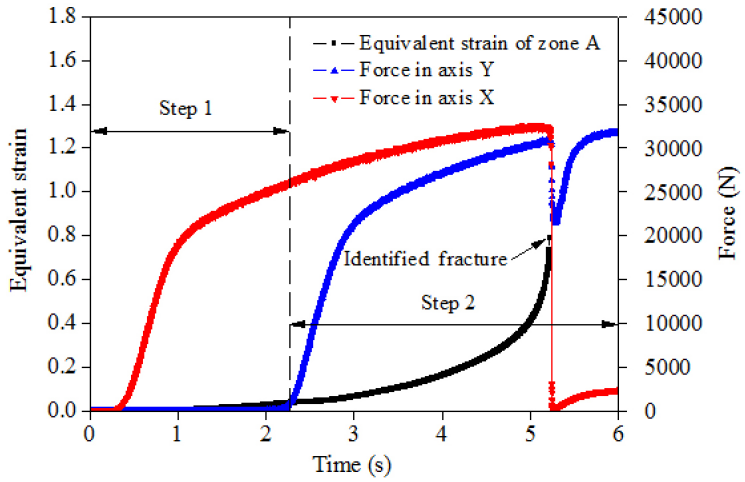

Figure 4.25: Force evolution in the test with a pre-displacement of 2 mm in uniaxial tension (type 2-A)

As shown in Figure 4.26, the onset of fracture identified by the time-dependent method is located at 5.21 s when the fracture can be observed clearly in Figure 4.15. However, there is no obvious decrease for the force in axis X or Y at 5.21 s. The force in axis X begins to decrease around 5.23 s, while the force in axis Y begins to decrease at 5.236 s. It can be concluded that it is hard to use the force evolution to identify the onset of fracture.

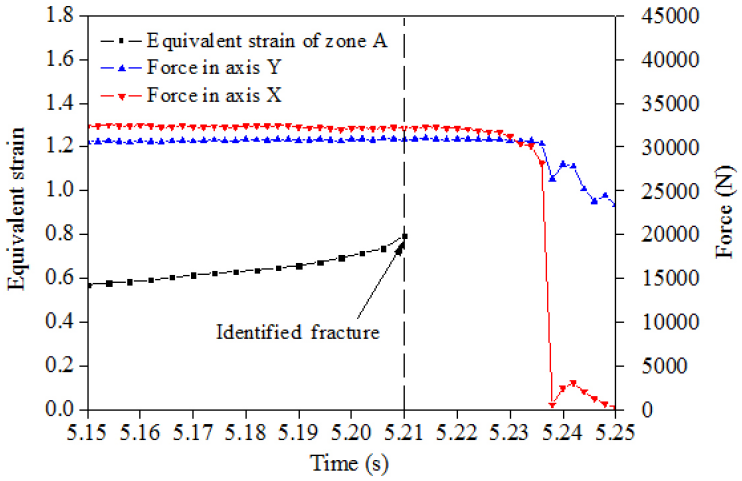

Figure 4.26: Force and strain evolution around the onset of fracture

4.3.4 Experimental characterization for FLCN

Type 2-A

The critical ratio method is applied to identify the forming limit strains at necking of DP600 sheet under the two types of non-linear strain paths.

The evolution of equivalent strain of zone A and B in Figure 4.13 under the type 2-A of non-linear strain path are shown in Figure 4.27. The identification of the onset of necking and forming limit strains with the pre-displacement of 2 mm and 4 mm in uniaxial tension are presented. When the necking happens in the central area, the equivalent strain of zone A increases abruptly due to the appearance of plastic instability, while the equivalent strain of zone B stops increase and a saturation appears. The moment of the saturation of equivalent strain in Figure 4.27 is used to define the onset of necking, and the major and minor strains of zone A corresponding to this moment define the forming limit strains at necking.

As shown in Figure 4.28, the levels of major strain for all strain paths is almost constant. It can be concluded that the prestrain in uniaxial tension has a small effect on the major strain at necking.

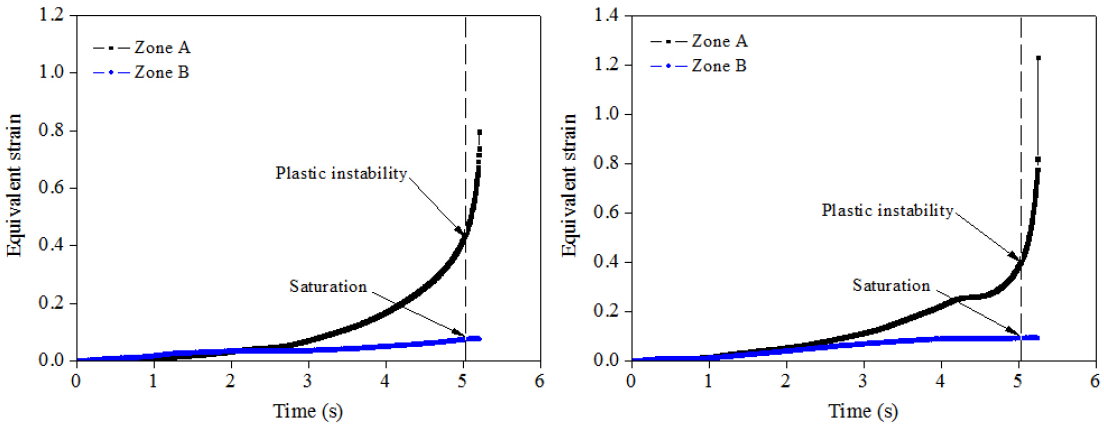

(a) 2 mm (b) 4 mm

Figure 4.27: Identification of necking for DP600 specimen with different pre-displacement in uniaxial tension

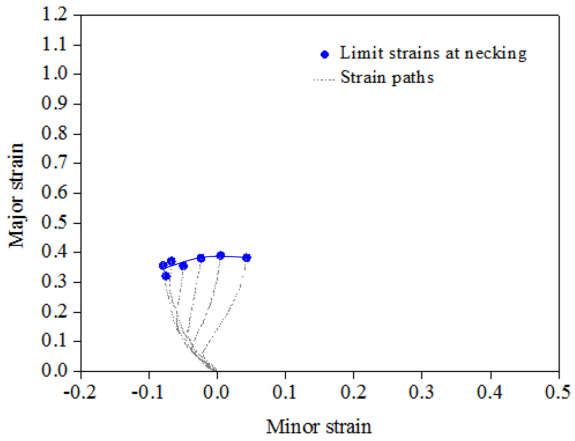

Figure 4.28: Forming limit strains at necking of DP600 sheet under type 2-A of non-linear strain paths

Type 2-B

For the type 2-B , the evolution of equivalent strain of zone A and B are shown in Figure 4.29. The identification of onset of necking and forming limit strains at necking with the pre-displacement of 2 mm and 4 mm in equibiaxial stretching are presented. In Figure 4.29 (a), and (b) , the equivalent strain of zone A and B increase with the displacement until the appearance of saturation. When the necking happens, the equivalent strain of zone A continues to increase, but the equivalent strain of zone B keep constant. The beginning time of saturation is used to define the onset of necking and the major and minor strains are determined at this moment.

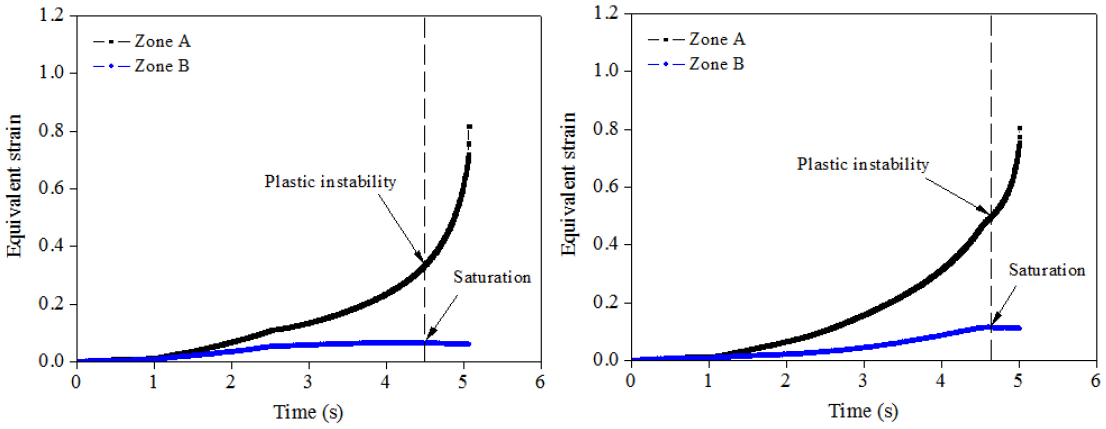

(a) 2 mm (b) 4 mm

Figure 4.29: Identification of necking for DP600 specimen with different pre-displacement in equibiaxial stretching

The forming limit strains at necking under type 2-B are shown in Figure 4.30. The level of major strain increases with the prestrain in equibiaxial stretching.

For the above section 4.3, some conclusions can be proposed: (1) The optimized cruciform specimen permits to produce the strain path change, and two types of non-linear strain paths have been realized; (2) The forming limit strain at fracture under two types of non-linear strain paths can be fitted by a straight line; (3) For the type 2-A of non-linear strain path, the prestrain in uniaxial tension has very small effect on the major strain at necking, while the major strain at necking increases with the prestrain in equibiaxial stretching for the type 2-B.

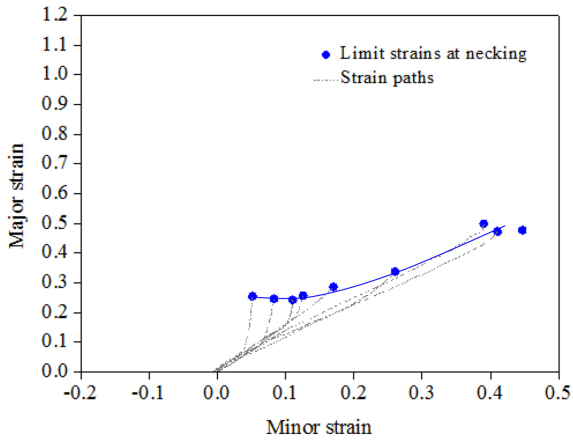

Figure 4.30: Forming limit strains at necking of DP600 sheet under type 2-B

4.4 Comparison of experimental results

4.4.1 FLCFs under linear and non-linear strain paths

Figure 4.31 shows the forming limit strains at fracture under linear and non-linear strain paths. As described previously, the forming limit strains at fracture under linear strain paths can be fitted by a straight line with k=-0.39 and A=0.63, while those under non-linear strain paths are fitted by a straight line with k=-0.49 and A=0.68. As shown in this figure, the difference between the FLCFs for linear strain paths and non-linear strain paths is small. In other words, the strain path change almost has very small effect on the forming limit strains at fracture.

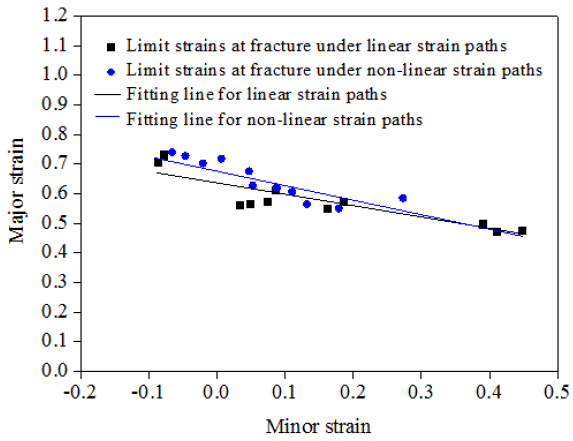

Figure 4.31: Forming limit strains at fracture of DP600 sheet under linear and non-linear strain paths

4.4.2 FLCNs under linear and non-linear strain paths

Figure 4.32 presents the comparison of forming limit strains at necking under linear and non-linear strain paths. For the type 2-A, the FLCN under non-linear strain paths shifts to the up with respect to the original FLCN under linear strain paths, and an increase of formability at necking is observed in Figure 4.32 (a). This phenomenon is also reported by Leotoing et al. [27] for an aluminium alloy sheet and Kuroda et al. [35] for a cold-rolled low-carbon steel, when the level of prestrain in uniaxial tension is not high. In their researches, a high level of prestrain in uniaxial tension can also reduce the formability at necking, which results in an abrupt decrease for the FLCN. In other words, the level of prestrain in uniaxial tension can either improve or reduce the formability at necking. However, as shown in Figure 4.32 (a), no reduction of formability at necking is observed under a high level of prestrain (major strain beyond 30%) in uniaxial tension. Therefore, it can be concluded that for the DP600 sheet, the prestrain in uniaxial tension can improve the formability at necking under the type 2-A of non-linear strain path.

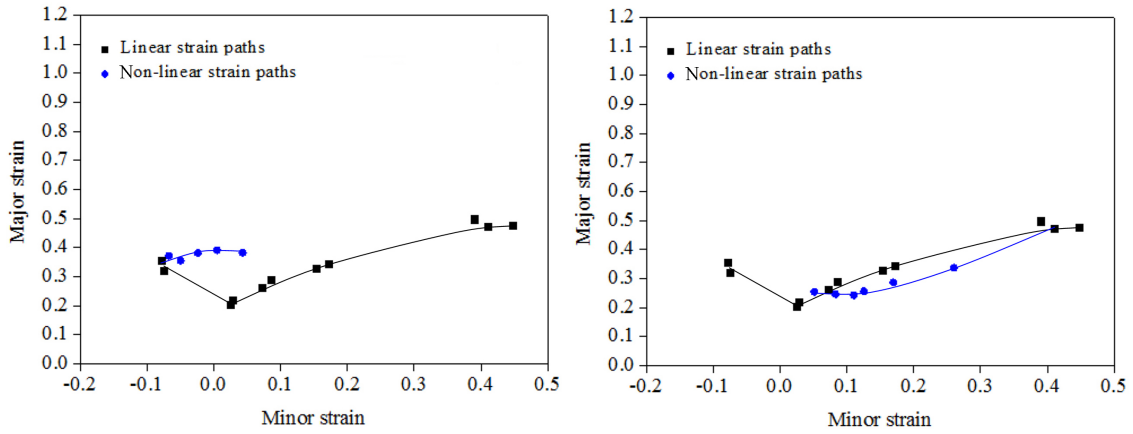

(a) Type 2-A (b) Type 2-B

Figure 4.32: Comparison of forming limit strains at necking of DP600 sheet under different strain paths

As shown in Figure 4.32 (b), the FLCN under non-linear strain path shifts to the down comparing with the original FLCN under linear strain paths. For small prestrain (8% or 10%) in equibiaxial stretching, there is no obvious difference between the FLCNs under linear strain paths and non-linear strain paths. With increasing the prestrain from 10% to 38%, a decrease of major strain at necking can be observed.

It can be concluded for the Section 4.4: (1) The strain path change has very small effect on the FLCF of DP600 sheet; (2) The prestrain in uniaxial tension

followed by equibiaxial stretching increases the forming limit strain at necking for DP600 sheet, while the prestrain in equibiaxial stretching followed by plane-strain tension decreases it.

4.5 Prediction of forming limits at fracture

For the numerical model of cruciform specimen and the constitutive model of DP600 sheet, detail informations are presented in Section 3.3. Cockroft and Latham criterion, Brozzo criterion, Ayada criterion, Rice and Tracey criterion, and Oyane criterion presented in Section 1.4.2 are used here to predict the experimental forming limits at fracture of DP600 sheet under linear and non-linear strain paths.

4.5.1 Numerical FLCFs under linear strain path

Cockroft and Latham criterion

Figure 4.33 shows the predictive results of forming limit strains with the Cockroft and Latham criterion, by introducing different values of C_1 (0.54, 0.57 and 0.72). For the three values of C_1, the numerical FLCFs calculated by the Cockroft and Latham criterion follow a line shape. With the increase of C_1 value, the position of the numerical FLCF changes while the slope keeps almost constant. The solid markers in the Figure 4.33 correspond to the experimental results identified with the DIC method. These experimental points are fitted by a red line with the least-square method. It can be observed that the slopes of the numerical and experimental FLCFs are quite different. For the DP600 sheet metal, the Cockroft and Latham criterion is not able to give a reliable prediction of forming limit strains, whatever the calibrated point. A calibration of the C_1 value near the plane-strain tension condition (C_1=0.57) will give the best prediction.

Brozzo criterion

The numerical FLCFs calculated by the Brozzo criterion with different values of C_2 (0.64, 0.74 and 0.84) are shown in Figure 4.34. The shape of the numerical FLCFs is very different from the experimental FLCF. Whatever the value of C_2 is used, the forming limit strains under equibiaxial stretching are significantly underestimated or those under uniaxial tension are significantly overestimated. Therefore, the Brozzo criterion is not suitable to predict fracture limits for the DP600 sheet.

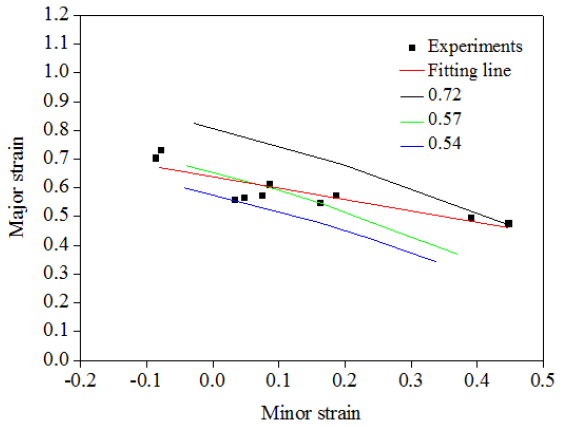

Figure 4.33: Numerical FLCFs under linear strain paths calculated by the Cockroft and Latham criterion

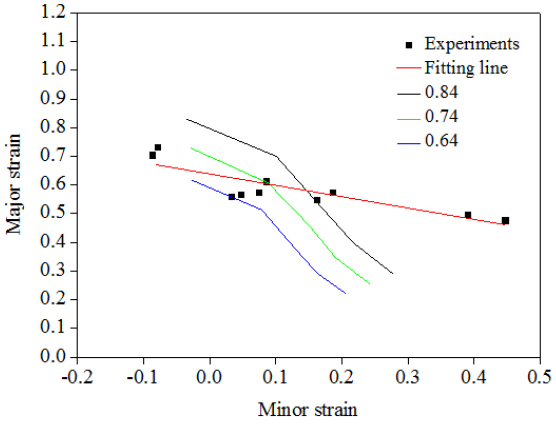

Figure 4.34: Numerical FLCFs under linear strain paths calculated by the Brozzo criterion

Ayada criterion

Figure 4.35 shows the numerical FLCFs calculated by the Ayada criterion with different values of C_3 (0.19, 0.17 and 0.15). For the three values of C_3, the numerical FLCFs show a line shape. The position of the numerical FLCF changes with increasing the value of C_3. However, whatever the value of C_3 is used, the slope of the numerical FLCFs is different from the one of experimental FLCF. For the DP600 sheet metal, the Ayada criterion is not suitable to produce numerical FLCF to predict the experimental results.

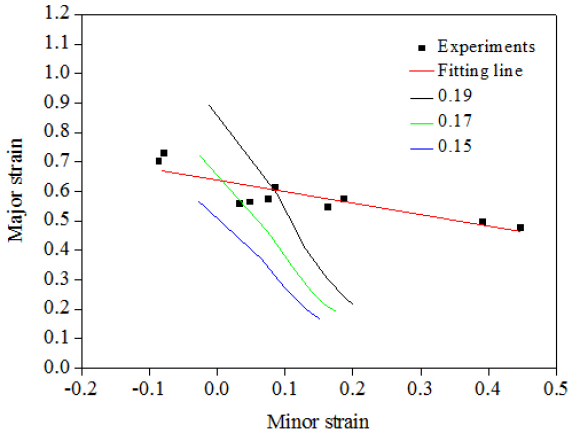

Figure 4.35: Numerical FLCFs under linear strain paths calculated by the Ayada criterion

Rice and Tracey criterion

Figure 4.36 shows the numerical FLCFs calculated by the Rice and Tracey criterion with different values of C_4 (1.25, 1.15 and 1.05). The numerical FLCFs calculated by three values of C_4 all present a line shape. Like the Ayada criterion, the slope of the numerical FLCFs is not suitable to predict the experimental results whatever the values of C_4 is used.

Oyane criterion

For the Oyane criterion, two parameters (C_{5a} and C_{5b}) have to be identified. In order to get the same slope of experimental FLCF (fitting line), a calibration procedure has been produced. Figure 4.37 (a) shows the numerical FLCFs calculated by two C_{5a} values. The Oyane criteiron becomes to the Ayada criterion if C_{5a}=0. As shown in the figure, the slope of the numerical FLCF calculated by C_{5a}=0 is not suitable to predict the experimental results. The slope of the numerical FLCF changes with

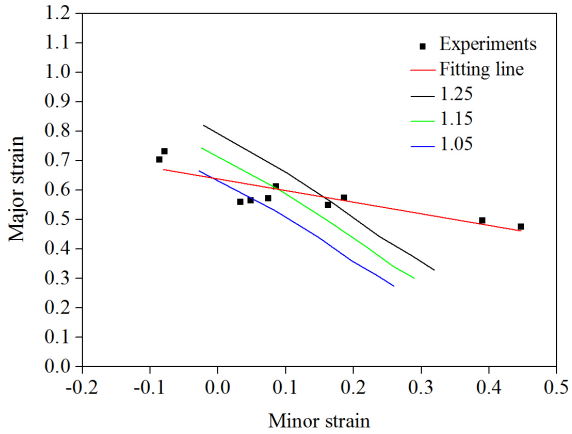

Figure 4.36: Numerical FLCFs under linear strain paths calculated by the Rice and Tracey criterion

the C_{5a} value, and the slopes of the experimetal fitting line and the numerical FLCF are almost same when C_{5a}=-1.

Three values of C_{5b} (0.48, 0.54 and 0.60) are used to discuss the effect of this parameter on the numerical FLCF. As shown in Figure 4.37 (b), the position is very sensitive to the values of C_{5b} and the fitting line of experimental values is used to choose the best value of C_{5b}. The numerical FLCF calibrated by C_{5b}=0.54 is almost overlapped by experimental fitting line. It can be concluded that the slope of the numerical FLCF depends on C_{5a} and the position is controlled by C_{5b}. The Oyane criterion with the set of values: C_{5a}=-1 and C_{5b}=0.54 predicts well the experimental results under different linear strain paths.

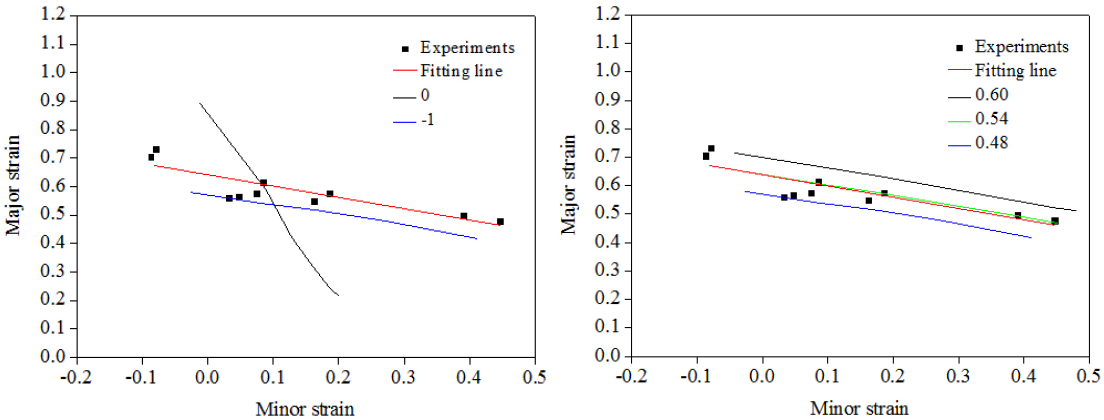

(a) Two C_{5a} values (b) Different C_{5b} values

Figure 4.37: Numerical FLCFs under linear strain paths calculated by the Oyane criterion

4.5.2 Numerical FLCFs under non-linear strain path

The Oyane criterion is selected to predict the experimental results under non-linear strain paths. As shown in Figure 4.38, the green and the blue lines show the numerical FLCFs under two types of non-linear strain paths calculated by the Oyane ductile fracture criterion (C_{5a}=-1.2 and C_{5b}=0.72). The red line shows the fitting line of the experimental results under two types of non-linear strain paths. It can be observed that the experimental results and the two numerical FLCFs are almost overlapped. The Oyane criterion predicts well the experimental results under two types of non-linear strain paths.

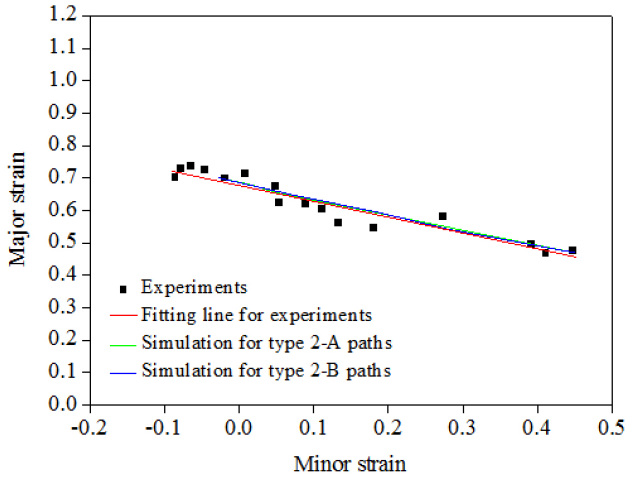

Figure 4.38: Prediction of forming limits at fracture for DP600 sheet under non-linear strain paths

4.6 Conclusion

In this chapter, the optimized cruciform specimen is validated by experimental tests. The experimental and numerical forming limit strains at necking and fracture of DP600 sheet under linear and non-linear strain paths have been investigated.

The experimental forming limit strains at fracture of DP600 sheet are determined by the proposed time-dependent method, while the ones at necking are identified by the critical ratio method. The forming limit strains are higher at fracture than at necking under different linear strain paths, except for equibiaxial stretching, for which no necking appears before fracture. The forming limit strains at fracture of DP600 sheet can be fitted by a straight line.

Two types of of non-linear strain paths without unloading are realized in the in-plane biaxial tensile tests. The experimental forming limit strains under non-linear strain paths can also be fitted by a straight line. The strain path change has very

small effect on the experimental FLCF. The prestrain in uniaxial tension followed by equibiaxial stretching can increase the level of forming limit strain at necking, while the prestrain in equibiaxial stretching followed by plane-strain tension can decrease it.

The Cockroft and Latham criterion, the Brozzo criterion, the Ayada criterion or the Rice and Tracey criterion with one parameter to be identified is not suitable to predict the experimental FLCF under linear strain paths. The Oyane criterion with two parameters to be identified predicts well the experimental results under linear and non-linear strain paths.

Conclusions and perspectives

The forming limits at necking and fracture of AA5086 and DP600 sheets under linear and non-linear strain paths have been investigated by using the in-plane biaxial tensile test with the cruciform specimen.

An existed cruciform specimen has been used to investigate the formability of AA5086 sheet with a thickness of 4 mm. This specimen permits to produce strain paths from equibiaxial stretching to uniaxial tension through plane-strain tension. The forming limit strains at fracture can be identified by a proposed time-dependent method combining the evolution of major strain with the observation of macroscopic crack at the specimen surface. The forming limit strains at fracture under linear strain paths can be fitted by a straight line, and the ones with the prestrain from 5% to 13% in uniaxial tension followed by equibiaxial stretching can also be fitted by a straight fitting line, while the ones with the prestrain of 19% are lower than it due to the occurrence of premature necking. The numerical predictions of FLCFs with three ductile fracture criteria from literatures can give very different results, depending on the experimental results chosen to calibrate the critical damage value. The Ayada criterion gives the best prediction. This cruciform specimen has been used to identify the fracture locus in equivalent strain and stress triaxiality space. Different linear strain paths can produce a wide range of stress triaxiality. The equivalent strain at fracture increases with decreasing the average stress triaxiality.

In order to widen the range of sheet thicknesses tested with this device, a new shape of cruciform specimen has been proposed for thinner sheet (2 mm). After a review of literatures, the following rules have been concluded to design a cruciform specimen shape for investigating fracture: (1) the tapered arm helps to shift plastic deformation closer to the central zone; (2) the slots in arms are very effective in making the strain distribution in the central zone almost uniform. Narrow, multiple and equally spaced slots are preferable for homogeneous strains; (3) the increase of notch depth promotes plastic deformation closer to the central zone; (4) the thickness reduction of central zone is essential for the onset of fracture at the specimen central point. Four previous cruciform specimens with an original thickness of 2 mm are selected and redesigned for obtaining the fracture in the center of specimen. Finally,

a new shape of specimen is proposed and optimized step by step.

The optimized cruciform specimen is used to identify the experimental and numerical forming limit strains at necking and fracture of DP600 sheet under linear and non-linear strain paths. The forming limit strains are higher at fracture than at necking under different linear strain paths, except for equibiaxial stretching, for which no necking appears before fracture. Two types of non-linear strain path without unloading are considered. The experimental forming limit strains at fracture under linear or non-linear strain paths can be fitted by a straight line. The strain path change has very small effect on the experimental FLCF. The prestrain in uniaxial tension followed by equibiaxial stretching increases the level of forming limit strain at necking, while the prestrain in equibiaxial stretching followed by plane-strain tension decreases it. The ductile fracture criteria with one parameter to be identified is not suitable to predict the experimental FLCF of DP600 sheet, while the Oyane criterion with two parameters to be identified gives a good prediction.

According to this work, two perspectives have been proposed:

(1) The in-plane biaxial tensile test with a cruciform specimen is proved to be efficient for identifying the forming limits at necking and fracture under ambient temperature. For improving the formability of sheet metal, warm forming processes are often considered. It is possible to use the in-plane biaxial tensile test to determine the forming limits at necking and fracture of sheet metal under different temperatures. Different strain rates in the range of intermediate strain rates can also be performed. The choice of the temperature and the strain rate will allow a precise characterization of the sheet formability in the real operating conditions.

(2) The strain path associated with the tension in a direction and the compression in the perpendicular direction can widen the range of the stress triaxiality. A modification of the experimental device is envisaged to be able to apply this type of loading. The numerical study has shown that such condition can make it possible to reach the negative stress triaxiality measured in the shear test. Validation of this type of test will increase the potential of the device to cover a wide range of strain path by using just a single shape of specimen.

Conclusions et perspectives

Les limites de formage à la striction et à la rupture de tôles en alliage d'aluminium AA5086 et en acier DP600 pour des chemins de déformation linéaires et non-linéaires ont pu être étudiées à partir d'un essai de traction plane biaxiale sur éprouvette cruciforme.

Une éprouvette cruciforme existante, développée pour des tôles de 4mm, a tout d'abord été utilisée pour caractériser la formabilité de l'alliage d'aluminium. Cette éprouvette permet d'atteindre des chemins de déformation dans le domaine du rétreint (traction mono-axiale) et dans celui de l'expansion (traction équi-biaxiale). Les déformations limites à rupture peuvent être identifiées grâce à un suivi temporel des déformations mesurées dans le plan de la tôle durant l'essai. Sur le diagramme limite de formage, les déformations limites à la rupture pour des chemins de déformation linéaires sont globalement réparties sur une ligne droite. Une conclusion identique peut être tirée lorsqu'une pré-déformation modérée sous chargement mono-axial est appliquée à l'éprouvette (jusqu' à 13%) avant un chargement équi-biaxial. Pour une pré-déformation plus importante, une rupture prématurée apparait lors du changement de chemin de déformation. La prédiction numérique des CLFR à partir de trois critères de rupture ductile de la littérature peut donner des résultats très différents, notamment suivant le choix des données expérimentales utilisées pour calibrer la valeur critique des variables d'endommagement. Le critère d'Ayada donne les meilleurs résultats. Les différents chemins de déformation linéaires permettent d'atteindre différents taux de triaxialité des contraintes. La déformation équivalente à la rupture augmente lorsque le taux de triaxialité des contraintes diminue.

Afin d'élargir la plage des épaisseurs de tôle testées avec ce dispositif, une nouvelle géométrie d'éprouvette cruciforme est optimisée pour des tôles moins épaisses (épaisseur initiale de 2mm). Une revue bibliographique sur les formes d'éprouvette cruciforme déjà utilisées a permis d'établir quelques règles claires pour atteindre systématiquement une rupture dans la zone centrale: (1) la variation de la largeur des bras favorise une localisation des déformations au centre; (2) la présence de rain-

ures (étroites et nombreuses) dans les bras permet d'homogénéiser les déformations au centre; (3) la forme du dégagement de matière dans la zone de raccord des bras joue un rôle sur la localisation des déformations dans la zone centrale; (4) la réduction de l'épaisseur au centre est essentielle pour observer une rupture au point central de l'éprouvette.

L'éprouvette cruciforme optimisée est utilisée pour identifier les déformations limites expérimentales et numériques de formage à la striction et à la rupture d'une tôle de DP600 pour différents modes de chargement (linéaires et non-linéaires). Les déformations limites sont plus élevées à la rupture qu'à la striction, excepté pour le chargement equi-biaxial pour lequel aucune striction n'apparaît avant la rupture. Deux types de chemin de déformation non-linéaire ont été considérés. Le type de chemin a très peu d'effet sur la CLFR expérimentale. Sur le diagramme limite de formage, le tracé des déformations limites expérimentales à la rupture pour des chemins de déformation linéaires et non-linéaires peut être approché par une droite. Pour la courbe limite de formage à striction, une pré-déformation en traction uniaxiale suivie d'une traction équi-biaxiale augmente le niveau de déformation atteint dans la tôle avant apparition d'une striction. L'effet est inverse lorsqu'une pré-déformation en traction equi-biaxiale est appliquée avant de poursuivre suivant un état de déformation plane dans le plan de la tôle. Les critères à la rupture ductile définis à partir du calibrage d'un unique paramètre ne semblent pas appropriés pour prédire la CLFR d'une tôle de DP600. L'utilisation d'un critère d'Oyane à deux paramètres a permis d'atteindre une bonne corrélation entre les résultats expérimentaux et numériques.

Suite à ce travail, deux perspectives principales sont envisagées :

(1) L'essai de traction biaxiale réalisé à partir d'une éprouvette cruciforme s'est avéré efficace pour identifier les limites de formage à la striction et à la rupture. Le dispositif a été validé à température ambiante. Pour améliorer la formabilité des tôles, des procédés de formage à chaud peuvent être envisagés. La caractérisation des limites de formage à différentes températures est possible avec le dispositif expérimental mis en place. Des essais à différentes vitesses de déformation, dans la gamme des vitesses de déformation intermédiaires, peuvent également être réalisés. Le choix des conditions de température et de vitesse de déformation permettra une caractérisation précise de la formabilité des tôles pour les conditions opératoires réellement appliquées lors de la mise en oeuvre du procédé de mise en forme choisi.

(2) Le chemin de déformation associé une traction dans une direction et à une compression suivant la direction perpendiculaire permettrait d'élargir considérablement la plage de variation du taux de triaxialité des contraintes. Une modification du dispositif expérimental est envisagée pour pouvoir appliquer ce type de charge-

ment. Une première étude numérique a montré que de telles conditions permettraient d'atteindre des taux de triaxialité des contraintes négatifs et de se rapprocher des taux mesurés lors d'un essai de cisaillement. La validation de ce type d'essai permettrait d'augmenter le potentiel du dispositif qui serait capable de couvrir une large plage de chemins de déformation en utilisant une forme d'éprouvette unique.

Appendix: List of publication and conference

International Journals

[1] Xiao SONG, Lionel LEOTOING, Dominique GUINES, Eric RAGNEAU. Characterization of forming limits at fracture with an optimized cruciform specimen: Application to DP600 steel sheets. International Journal of Mechanical Science, 2017, 126: 35-43.

[2] Xiao SONG, Lionel LEOTOING, Dominique GUINES, Eric RAGNEAU. Investigation of the forming limit strains at fracture of AA5086 sheets using an in-plane biaxial tensile test. Engineering Fracture Mechanics, 2016, 163: 130-140.

International Conferences

[1] Xiao SONG, Lionel LEOTOING, Dominique GUINES, Eric RAGNEAU. Identification of forming limits at fracture of DP600 sheet metal under linear and unloaded non-linear strain paths. International Conference on the Technology of Plasticity (ICTP 2017), Cambridge, United Kingdom (Published in Procedia Engineering, 2017, 207: 562-567).

[2] Xiao SONG, Lionel LEOTOING, Dominique GUINES, Eric RAGNEAU. Identification of forming limits at fracture using an in-plane biaxial tensile test with a dedicated cruciform specimen. International Conference on Multiaxial Fatigue and Fracture (ICMFF 2016), Seville, Spain.

References

[1] M. B. Silva, P. S. Nielsen, N. Bay, and P. A. F. Martins. Failure mechanisms in single-point incremental forming of metals. *The International Journal of Advanced Manufacturing Technology*, 56(9):893–903, 2011. 5

[2] S. K. Paul. Path independent limiting criteria in sheet metal forming. *Journal of Manufacturing Processes*, 20:291–303, 2015. 5

[3] Z. Marciniak, J. L. Duncan, and S. J. Hu. *Mechanics of sheet metal forming*. Butterworth-Heinemann, 2002. 5

[4] P. Eyckens, S. He, A. Van Bael, P. Van Houtte, and J. Duflou. Forming limit predictions for the serrated strain paths in single point incremental sheet forming. In *AIP Conference Proceedings*, volume 908, pages 141–146. AIP, 2007. 6

[5] K. Isik, M. B. Silva, A. E. Tekkaya, and P. A. F. Martins. Formability limits by fracture in sheet metal forming. *Journal of Materials Processing Technology*, 214(8):1557–1565, 2014. 7, 31, 32, 54

[6] J. Lemaitre, J. L. Chaboche, A. Benallal, and R. Desmorat. *Mecanique des materiaux solides*. Dunod, 2009. 11

[7] A. Gavrus. Constitutive equation for description of metallic materials behavior during static and dynamic loadings taking into account important gradients of plastic deformation. In *Key Engineering Materials*, volume 504, pages 697–702. Trans Tech Publ, 2012. 12

[8] P. A. F. Martins, N. Bay, A. E. Tekkaya, and A. G. Atkins. Characterization of fracture loci in metal forming. *International Journal of Mechanical Sciences*, 83:112–123, 2014. 12

[9] K. Yoshida, T. Kuwabara, and M. Kuroda. Path-dependence of the forming limit stresses in a sheet metal. *International Journal of Plasticity*, 23(3):361–384, 2007. 12, 30

[10] A.B. Da Rocha, F. Barlat, and J.M. Jalinier. Prediction of the forming limit diagrams of anisotropic sheets in linear and non-linear loading. *Materials science and engineering*, 68(2):151–164, 1985. 12, 22

[11] L. Léotoing, D. Guines, I. Zidane, and E. Ragneau. Cruciform shape benefits for experimental and numerical evaluation of sheet metal formability. *Journal of Materials Processing Technology*, 213(6):856–863, 2013. 14, 29, 34, 55

[12] I. Zidane, D. Guines, L. Léotoing, and E. Ragneau. Development of an in-plane biaxial test for forming limit curve (FLC) characterization of metallic sheets. *Measurement Science and Technology*, 21(5):055701, 2010. 15, 21, 22, 34, 48, 86, 114

[13] X. Song, L. Leotoing, D. Guines, and E. Ragneau. Investigation of the forming limit strains at fracture of AA5086 sheets using an in-plane biaxial tensile test. *Engineering Fracture Mechanics*, 163:130–140, 2016. 15

[14] International standard ISO 12004-2: 2008 metallic materials - sheet and strip - determination of forming-limit curves - part 2: Determination of forming-limit curve in the laboratory, 2008. 16

[15] X.R. Chu. *Caractérisation expérimentale et prédiction de la formabilité d'un alliage d'aluminium en fonction de la température et de la vitesse de déformation*. PhD thesis, INSA-Rennes, 2013. 16

[16] M. Merklein, A. Kuppert, and M. Geiger. Time dependent determination of forming limit diagrams. *CIRP Annals-Manufacturing Technology*, 59(1):295–298, 2010. 17, 18

[17] A.J. Martínez-Donaire, F.J. García-Lomas, and C. Vallellano. New approaches to detect the onset of localised necking in sheets under through-thickness strain gradients. *Materials and Design*, 57:135–145, 2014. 18, 19

[18] X.R. Chu, L. Léotoing, D. Guines, and E. Ragneau. Temperature and strain rate influence on aa5086 forming limit curves: Experimental results and discussion on the validity of the mk model. *International Journal of Mechanical Sciences*, 78:27–34, 2014. 19, 20, 48

[19] M. B. Silva, A. J. Martínez-Donaire, G. Centeno, D. Morales-Palma, C. Vallellano, and P. A. F. Martins. Recent approaches for the determination of forming limits by necking and fracture in sheet metal forming. *Procedia Engineering*, 132:342–349, 2015. 21

[20] D. Zeng, L. Chappuis, Z. Xia, and X. Zhu. A path independent forming limit criterion for sheet metal forming simulations. *SAE International Journal of Materials and Manufacturing*, 1(2008-01-1445):809–817, 2008. 21

[21] H. Ishigaki. *Deformation Analysis of Large Sized Panels in the Press Shop*, pages 315–339. Springer US, Boston, MA, 1978. 22, 23

[22] F. Zhalehfar, S. J. Hosseinipour, S. Nourouzi, and A. H. Gorji. A different approach for considering the effect of non-proportional loading path on the forming limit diagram of aa5083. *Materials & Design*, 50:165–173, 2013. 22

[23] W. Volk, H. Hoffmann, J. Suh, and J. Kim. Failure prediction for nonlinear strain paths in sheet metal forming. *CIRP Annals-Manufacturing Technology*, 61(1):259–262, 2012. 22

[24] A. Graf and W. Hosford. The influence of strain-path changes on forming limit diagrams of Al 6111 T4. *International Journal of Mechanical Sciences*, 36(10):897–910, 1994. 24

[25] T. B. Stoughton and J. W. Yoon. Path independent forming limits in strain and stress spaces. *International Journal of Solids and Structures*, 49(25):3616–3625, 2012. 24

[26] A. Graf and W. Hosford. Effect of changing strain paths on forming limit diagrams of al 2008-t4. *Metallurgical Transactions A*, 24A:2503–2512, 1993. 24

[27] L. Léotoing and D. Guines. Investigations of the effect of strain path changes on forming limit curves using an in-plane biaxial tensile test. *International Journal of Mechanical Sciences*, 99:21–28, 2015. 25, 34, 55, 63, 64, 114, 130

[28] C.L. Chow, L.G. Yu, W.H. Tai, and M.Y. Demeri. Prediction of forming limit diagrams for al6111-t4 under non-proportional loading. *International journal of mechanical sciences*, 43(2):471–486, 2001. 26

[29] R.T. Hill. On discontinuous plastic states, with special reference to localized necking in thin sheets. *Journal of the Mechanics and Physics of Solids*, 1(1):19–30, 1952. 27

[30] Z. Marciniak and K. Kuczyński. Limit strains in the processes of stretch-forming sheet metal. *International Journal of Mechanical Sciences*, 9(9):609–620, 1967. 27

[31] C. S. Zhang. *Etude de l'effet de la sensibilité la vitesse de déformation sur la formabilité de tôle en alliage d'aluminium*. PhD thesis, INSA-Rennes, 2008. 27, 28

[32] P. Hora, L. Tong, and B. Berisha. Modified maximum force criterion, a model for the theoretical prediction of forming limit curves. *International journal of material forming*, 6(2):267–279, 2013. 28

[33] C. S. Zhang, L. Léotoing, G. Q. Zhao, D. Guines, and E. Ragneau. A methodology for evaluating sheet formability combining the tensile test with the m–k model. *Materials Science and Engineering: A*, 528(1):480–485, 2010. 29

[34] A. Graf and W. Hosford. Calculations of forming limit diagrams for changing strain paths. *Metallurgical Transactions A*, 24(11):2497–2501, 1993. 29

[35] M. Kuroda and V. Tvergaard. Effect of strain path change on limits to ductility of anisotropic metal sheets. *International Journal of Mechanical Sciences*, 42(5):867–887, 2000. 30, 130

[36] R. Arrieux, C. Bedrin, and M. Boivin. Determination of an intrinsic forming limit stress diagram for isotropic sheets. In *Proceedings of the 12th IDDRG Congress*, volume 2, pages 61–71, 1982. 30

[37] T. B. Stoughton. A general forming limit criterion for sheet metal forming. *International Journal of Mechanical Sciences*, 42(1):1–27, 2000. 30

[38] T. B. Stoughton and J. W. Yoon. Sheet metal formability analysis for anisotropic materials under non-proportional loading. *International journal of mechanical sciences*, 47(12):1972–2002, 2005. 30

[39] M. C. Butuc, J. J. Gracio, and A. B. Da Rocha. An experimental and theoretical analysis on the application of stress-based forming limit criterion. *International Journal of Mechanical Sciences*, 48(4):414–429, 2006. 30

[40] M. B. Silva, M. Skjoedt, A. G. Atkins, N. Bay, and P. A. F. Martins. Single-point incremental forming and formability-failure diagrams. *The Journal of Strain Analysis for Engineering Design*, 43(1):15–35, 2008. 30

[41] S. Bruschi, T. Altan, D. Banabic, P. F. Bariani, A. Brosius, J. Cao, A. Ghiotti, M. Khraisheh, M. Merklein, and A. E. Tekkaya. Testing and modelling of material behaviour and formability in sheet metal forming. *CIRP Annals-Manufacturing Technology*, 63(2):727–749, 2014. 31

[42] H. Takuda, K. Mori, N. Takakura, and K. Yamaguchi. Finite element analysis of limit strains in biaxial stretching of sheet metals allowing for ductile fracture. *International Journal of Mechanical Sciences*, 42(4):785–798, 2000. 31, 37, 115

[43] H. N. Han and K. H. Kim. A ductile fracture criterion in sheet metal forming process. *Journal of Materials Processing Technology*, 142(1):231–238, 2003. 31

[44] P.A.F. Martins, L. Montanari, V.A. Cristino, and M.B. Silva. Formability and simulative tests in modern sheet metal forming education. In *Modern Mechanical Engineering*, pages 411–447. Springer, 2014. 31, 32

[45] M. Gorji, B. Berisha, P. Hora, and F. Barlat. Modeling of localization and fracture phenomena in strain and stress space for sheet metal forming. *International Journal of Material Forming*, pages 1–12, 2015. 33

[46] R. Xiao, X. X. Li, L. H. Lang, Y. K. Chen, and Y. F. Yang. Biaxial tensile testing of cruciform slim superalloy at elevated temperatures. *Materials & Design*, 94:286–294, 2016. 33

[47] R. Xiao, X. X. Li, L. H. Lang, Q. Song, and K. N. Liu. Forming limit in thermal cruciform biaxial tensile testing of titanium alloy. *Journal of Materials Processing Technology*, 240:354–361, 2017. 33, 34, 37, 85, 86

[48] B.P.P.A. Gouveia, J.M.C. Rodrigues, and P.A.F. Martins. Ductile fracture in metalworking: experimental and theoretical research. *Journal of Materials Processing Technology*, 101(1):52–63, 2000. 34

[49] H. Li, M.W. Fu, J. Lu, and H. Yang. Ductile fracture: experiments and computations. *International journal of plasticity*, 27(2):147–180, 2011. 34

[50] V. Tvergaard and A. Needleman. Analysis of the cup-cone fracture in a round tensile bar. *Acta metallurgica*, 32(1):157–169, 1984. 34

[51] J. Lemaitre. A continuous damage mechanics model for ductile fracture. *Journal of Engineering Materials and Technology*, 107(1):83–89, 1985. 34

[52] S. E. Clift. Fracture in forming process. In *Research, Development and Applications*, pages 406–418. Springer, 1992. 34

[53] Q. M. Li. Strain energy density failure criterion. *International Journal of Solids and Structures*, 38(38):6997–7013, 2001. 34

[54] A. S. Khan and H. Liu. A new approach for ductile fracture prediction on al 2024-t351 alloy. *International Journal of Plasticity*, 35:1–12, 2012. 34

[55] M. G. Cockroft and D. G. Latham. Ductility and the workability of metals. *Journal of the Institute of Metals*, 96:33–39, 1968. 35

[56] P. Brozzo, B. Deluca, and R. Rendina. A new method for the prediction of formability in metal sheets. In *Proceedings of the Seventh Biennial Conference of the IDDRG*, 1972. 35

[57] F. A. McClintock. A criterion for ductile fracture by the growth of holes. *Journal of applied mechanics*, 35(2):363–371, 1968. 35

[58] A. Mishra and S. Thuillier. Investigation of the rupture in tension and bending of dp980 steel sheet. *International Journal of Mechanical Sciences*, 84:171–181, 2014. 35, 36

[59] J. R. Rice and D. M. Tracey. On the ductile enlargement of voids in triaxial stress fields. *Journal of the Mechanics and Physics of Solids*, 17:201–207, 1969. 35

[60] M. Oyane, T. Sato, K. Okimoto, and S. Shima. Criteria for ductile fracture and their applications. *Journal of Mechanical Working Technology*, 4(1):65–81, 1980. 35

[61] H. Takuda, K. Mori, and N. Hatta. The application of some criteria for ductile fracture to the prediction of the forming limit of sheet metals. *Journal of materials processing technology*, 95(1):116–121, 1999. 35

[62] H. Takuda, K. Mori, H. Fujimoto, and N. Hatta. Prediction of forming limit in deep drawing of Fe/Al laminated composite sheets using ductile fracture criterion. *Journal of Materials Processing Technology*, 60(1):291–296, 1996. 35

[63] H. Takuda, K. Mori, H. Fujimoto, and N. Hatta. Prediction of forming limit in bore-expanding of sheet metals using ductile fracture criterion. *Journal of Materials Processing Technology*, 92:433–438, 1999. 36

[64] S. E. Clift, P. Hartley, C. E. N. Sturgess, and G. W. Rowe. Fracture prediction in plastic deformation processes. *International Journal of Mechanical Sciences*, 32(1):1–17, 1990. 36

[65] F. Ozturk and D Lee. Analysis of forming limits using ductile fracture criteria. *Journal of Materials Processing Technology*, 147(3):397–404, 2004. 36

[66] M. Jain, J. Allin, and D. J. Lloyd. Fracture limit prediction using ductile fracture criteria for forming of an automotive aluminum sheet. *International Journal of Mechanical Sciences*, 41(10):1273–1288, 1999. 37

[67] S. Gerke, P. Adulyasak, and M. Brünig. New biaxially loaded specimens for the analysis of damage and fracture in sheet metals. *International Journal of Solids and Structures*, 110:209–218, 2017. 38, 41, 43, 44

[68] Y. B. Bao and T. Wierzbicki. On fracture locus in the equivalent strain and stress triaxiality space. *International Journal of Mechanical Sciences*, 46(1):81–98, 2004. 39, 40, 68

[69] D. Anderson, S. Winkler, A. Bardelcik, and M. J. Worswick. Influence of stress triaxiality and strain rate on the failure behavior of a dual-phase dp780 steel. *Materials & Design*, 60:198–207, 2014. 39

[70] W. C. Li, F. F. Liao, T. H. Zhou, and H. Askes. Ductile fracture of q460 steel: Effects of stress triaxiality and lode angle. *Journal of Constructional Steel Research*, 123:1–17, 2016. 41

[71] M. Brünig, D. Brenner, and S. Gerke. Stress state dependence of ductile damage and fracture behavior: experiments and numerical simulations. *Engineering Fracture Mechanics*, 141:152–169, 2015. 41, 42

[72] M. Brünig, S. Gerke, and M. Schmidt. Biaxial experiments and phenomenological modeling of stress-state-dependent ductile damage and fracture. *International Journal of Fracture*, 200(1-2):63–76, 2016. 41

[73] I. Zidane. *Développement d'un banc d'essai de traction biaxiale pour la caractérisation de la formabilité et du comportement élastoplastique de tôles métalliques*. PhD thesis, INSA Rennes, 2009. 48, 84, 85

[74] B. Pan, K. M. Qian, H. M. Xie, and A. Asundi. Two-dimensional digital image correlation for in-plane displacement and strain measurement: a review. *Measurement science and technology*, 20(6):062001, 2009. 48, 50

[75] H. Schreier, J. J. Orteu, and M. A. Sutton. *Image correlation for shape, motion and deformation measurements*. Springer US, 2009. 50

[76] J. C. Dupre, P. Doumalin, V. Valle, and F. Bremand. *Mode d'emploi du logiciel CORRELA 2006*. Université de Poitiers, 2006. 50

[77] S. Y. Zhang, L. Léotoing, D. Guines, S. Thuillier, and S. L. Zang. Calibration of anisotropic yield criterion with conventional tests or biaxial test. *International Journal of Mechanical Sciences*, 85:142–151, 2014. 56

[78] S. Diot, D. Guines, A. Gavrus, and E. Ragneau. Forming process of a 5083 aluminium alloy constitutive model covering a large range of temperature. *International Journal of Forming Processes*, 9(2):167–188, 2006. 57

[79] W. Liu, D. Guines, L. Léotoing, and E. Ragneau. Identification of sheet metal hardening for large strains with an in-plane biaxial tensile test and a dedicated cross specimen. *International Journal of Mechanical Sciences*, 101:387–398, 2015. 57, 79, 80, 86

[80] W. Liu. *Identification of strain rate dependent hardening sensitivity of metallic sheets under in-plane biaxial loading*. PhD thesis, INSA-Rennes, 2015. 89

[81] T. Kuwabara. Advances in experiments on metal sheets and tubes in support of constitutive modeling and forming simulations. *International Journal of Plasticity*, 23(3):385–419, 2007. 75

[82] A. Hannon and P. Tiernan. A review of planar biaxial tensile test systems for sheet metal. *Journal of materials processing technology*, 198(1):1–13, 2008. 75

[83] W. Müller and K. Pohlandt. New experiments for determining yield loci of sheet metal. *Journal of Materials Processing Technology*, 60(1):643–648, 1996. 75, 76

[84] D. Banabic, H. Aretz, D.S. Comsa, and L. Paraianu. An improved analytical description of orthotropy in metallic sheets. *International Journal of Plasticity*, 21(3):493–512, 2005. 76

[85] T. Naka, Y. Nakayama, T. Uemori, R. Hino, and F. Yoshida. Effects of temperature on yield locus for 5083 aluminum alloy sheet. *Journal of Materials Processing Technology*, 140(1):494–499, 2003. 76, 77

[86] T. Kuwabara, S. Ikeda, and K. Kuroda. Measurement and analysis of differential work hardening in cold-rolled steel sheet under biaxial tension. *Journal of Materials Processing Technology*, 80:517–523, 1998. 76, 77

[87] T. Kuwabara, A. Van Bael, and E. Iizuka. Measurement and analysis of yield locus and work hardening characteristics of steel sheets wtih different r-values. *Acta materialia*, 50(14):3717–3729, 2002. 76

[88] M. Merklein and M. Biasutti. Development of a biaxial tensile machine for characterization of sheet metals. *Journal of Materials Processing Technology*, 213(6):939–946, 2013. 78

[89] D. Kulawinski, K. Nagel, S. Henkel, P. Hübner, H. Fischer, M. Kuna, and H. Biermann. Characterization of stress-strain behavior of a cast trip steel under different biaxial planar load ratios. *Engineering Fracture Mechanics*, 78(8):1684–1695, 2011. 78

[90] D. E. Green, K. W. Neale, S. R. MacEwen, A. Makinde, and R. Perrin. Experimental investigation of the biaxial behaviour of an aluminum sheet. *International journal of plasticity*, 20(8):1677–1706, 2004. 78

[91] A. Makinde, L. Thibodeau, and K. W. Neale. Development of an apparatus for biaxial testing using cruciform specimens. *Experimental mechanics*, 32(2):138–144, 1992. 78

[92] A. Makinde, L. Thibodeau, K. W. Neale, and D. Lefebvre. Design of a biaxial extensometer for measuring strains in cruciform specimens. *Experimental mechanics*, 32(2):132–137, 1992. 78

[93] N. X. Deng and Y. P. Korkolis. Cruciform specimen design and validation for constitutive identification of sheet metal. In *NUMISHEET 2014: The 9th International Conference and Workshop on Numerical Simulation of 3D Sheet Metal Forming Processes: Part A Benchmark Problems and Results and Part B General Papers*, volume 1567, pages 620–623. AIP Publishing, 2013. 78, 79

[94] G. Mitukiewicz and M. Głogowski. Cruciform specimen to obtain higher plastic deformation in a gauge region. *Journal of Materials Processing Technology*, 227:11–15, 2016. 79, 80

[95] C. C. Tasan, J. P. M. Hoefnagels, G. Quaak, and M. G. D. Geers. In-plane biaxial loading of sheet metal until fracture. In *Proceedings of the 2008 SEM XI international congress and exposition on experimental and applied mechanics, Orlando, Florida*, pages 2–5, 2008. 81, 86

[96] F. Abu-Farha, L. G. Hector Jr, and M. Khraisheh. Cruciform-shaped specimens for elevated temperature biaxial testing of lightweight materials. *JOM*, 61(8):48–56, 2009. 81, 82

[97] A. Makris, T. Vandenbergh, C. Ramault, D. Van Hemelrijck, E. Lamkanfi, and W. Van Paepegem. Shape optimisation of a biaxially loaded cruciform specimen. *Polymer Testing*, 29(2):216–223, 2010. 82

[98] F. Abbassi, S. Mistou, and A. Zghal. Failure analysis based on microvoid growth for sheet metal during uniaxial and biaxial tensile tests. *Materials & Design*, 49:638–646, 2013. 82, 83

[99] P. Tiernan and A. Hannon. Design optimisation of biaxial tensile test specimen using finite element analysis. *International journal of material forming*, 7(1):117–123, 2014. 82, 83

[100] R. S. Lee and T. W. Chien. A new method for testing formability in sheet metal forming at biaxial tensile state. In *Key Engineering Materials*, volume 626, pages 275–280. Trans Tech Publ, 2014. 83, 84, 86

[101] F. K. Abu-Farha, L. G. Hector, and M. A. Nazzal. On the development of viable cruciform-shaped specimens: towards accurate elevated temperature biaxial testing of lightweight materials. In *Key Engineering Materials*, volume 433, pages 93–101. Trans Tech Publ, 2010. 83, 84

[102] Q. Le, H. T. Kang, G. Kridli, A. K. Khosrovaneh, and B. Yan. Effect of prestrain paths on mechanical behavior of dual phase sheet steel. *International Journal of Fatigue*, 31(4):607–615, 2009. 88

[103] A. Ramazani, M. Abbasi, U. Prahl, and W. Bleck. Failure analysis of DP600 steel during the cross-die test. *Computational Materials Science*, 64:101–105, 2012. 88

[104] W. R. Wang, C. W. He, Z. H. Zhao, and X. C. Wei. The limit drawing ratio and formability prediction of advanced high strength dual-phase steels. *Materials and Design*, 32(6):3320–3327, 2011. 88

[105] F. Ozturk, S. Toros, and S. Kilic. Tensile and spring-back behavior of DP600 advanced high strength steel at warm temperatures. *Journal of Iron and Steel Research, International*, 16(6):41–46, 2009. 88

[106] W. Liu, D. Guines, L. Leotoing, and E. Ragneau. Identification of strain rate-dependent mechanical behaviour of DP600 under in-plane biaxial loadings. *Materials Science and Engineering: A*, 676:366–376, 2016. 88

[107] F. Ozturk, S. Toros, and S. Kilic. Effects of anisotropic yield functions on prediction of forming limit diagrams of DP600 advanced high strength steel. *Procedia Engineering*, 81:760–765, 2014. 88

[108] C. S. Zhang, L. Léotoing, G. Q. Zhao, D. Guines, and E. Ragneau. A comparative study of different necking criteria for numerical and experimental prediction of flcs. *Journal of materials engineering and performance*, 20(6):1036–1042, 2011. 114

[109] J. D. Embury and J. L. Duncan. Formability maps. *Annual Review of Materials Science*, 11(1):505–521, 1981. 115

INSA de RENNES
Service des Formations

AVIS DU JURY SUR LA REPRODUCTION DE LA THESE SOUTENUE

Titre de la thèse:
Identification of forming limits of sheet metals with an in-plane biaxial tensile test

Nom Prénom de l'auteur : SONG XIAO

Membres du jury :
- Monsieur RAGNEAU ERIC
- Monsieur GUINES Dominique
- Monsieur LEOTOING Lionel
- Madame BALLAND Pascale
- Monsieur THIBAUD Sébastien
- Monsieur BOUCHAR Pierre-Olivier

Président du jury : Pierre-olivier BOUCHARD

Date de la soutenance : 27 Mars 2018

Reproduction de la these soutenue

☒ Thèse pouvant être reproduite en l'état
☐ Thèse pouvant être reproduite après corrections suggérées

Fait à Rennes, le 27 Mars 2018

Signature du président de jury

Le Directeur,

M'hamed DRISSI

Résumé

Les procédés de mise en forme des tôles minces sont largement utilisés dans l'industrie pour la production de pièces très diverses. L'utilisation optimale des matériaux constitutifs de ces tôles, comme les alliages légers ou les aciers à haute résistance, propices à des économies d'énergie dans le domaine des transports, nécessite une connaissance approfondie de leurs limites de formabilité. Classiquement, la formabilité d'une tôle est caractérisée par son aptitude à se déformer sans apparition d'une striction localisée. L'outil associé est la courbe limite de formage à striction (CLFS) qui est généralement caractérisée pour des chemins de déformation linéaires. Cependant, pour des chargements spécifiques (chemins de déformation complexes, traction équi-biaxiale ...), une rupture ductile peut être induite avant apparition d'une forme de striction. Dans ce cas, la rupture plutôt que la striction caractérise la formabilité du matériau, la courbe limite de formage à rupture (CLFR) doit alors être considérée.

Pour identifier la CLFS et la CLFR pour des chemins de déformation linéaires et non-linéaires, les méthodes conventionnelles requièrent différents dispositifs expérimentaux et différentes formes d'éprouvette pour atteindre une large gamme de chemins de déformation. L'essai de traction biaxiale, associé à une éprouvette cruciforme, est une alternative intéressante à ces méthodes. Le chemin de déformation suivi durant l'essai est directement contrôlé par le mouvement de quatre vérins indépendants. Ce dispositif permet de couvrir une large gamme de chemin, à partir d'une forme unique d'éprouvette cruciforme. De plus, le changement de chemin est activé au cours de l'essai, sans déchargement.

Le premier objectif de cette étude est de montrer que l'essai de traction biaxiale, associé à une forme unique d'éprouvette cruciforme, permet de tracer la CLFS et la CLFR pour plusieurs chemins de déformation, qu'ils soient linéaires ou non-linéaires. En premier lieu, des essais ont été réalisés sur des tôles d'alliage d'aluminium 5086 (épaisseur initiale de 4 mm) à partir d'une forme d'éprouvette déjà proposée au laboratoire. Des déformations limites à rupture pour des chemins de déformation linéaires et non-linéaires (traction uniaxiale suivie d'une traction équi-biaxiale) ont été identifiées. Une nouvelle forme d'éprouvette cruciforme a été proposée pour des tôles moins épaisses (2 mm), plus répandues. L'éprouvette cruciforme optimisée a été validée pour étudier la formabilité d'un acier dual phase DP600 pour deux types de chemin de déformation non-linéaires.

Le deuxième objectif est de discuter la validité de critères classiques de rupture ductile à partir d'une simulation par éléments finis de l'essai de traction biaxiale. Plusieurs critères de rupture existants ont été sélectionnés (Cockroft et Latham, Ayada, Oyane ...) et calibrés à partir des données expérimentales pour tracer des CLFR numériques pour les deux matériaux étudiés. Les CLFR obtenues peuvent être très différentes mais, pour chaque matériau, un critère a finalement été identifié pour prédire assez précisément les résultats expérimentaux.

Abstract

Sheet metal forming is very common in industry for producing various components. The optimal use of materials, like light alloys or high strength steels in transportation for energy economy, requires in-depth analysis of their formability. Usually, the formability of sheet metal is controlled by the onset of localized necking, and the forming limit curve at necking (FLCN), generally restricted to linear strain paths, is adopted. However, under specific loadings (complex strain paths, near balanced biaxial stretching ...), ductile fracture can be induced without any obvious necking phenomenon. In that case, the fracture rather than the necking characterizes the formability, and the forming limit curve at fracture (FLCF) should be considered.

For identifying FLCN and FLCF under linear and non-linear strain paths, conventional methods require different experimental devices and geometrical specifications of specimen to follow various strain paths. Using the in-plane biaxial tensile test with a cruciform specimen can be an interesting alternative to overcome the drawbacks of conventional methods. The strain path during the test can be directly controlled by the motion of four independent actuators, which is sufficient to cover a wide range of strain paths, just with one shape of cruciform specimen. Besides, changes of strain path are made during the same test, without unloading.

The first objective of this study is to show that the in-plane biaxial tensile test with a single type of cruciform specimen permits to investigate the FLCN and FLCF of sheet metals under different strain paths including linear and non-linear evolutions. Firstly, in-plane biaxial tensile tests have been carried out on AA5086 sheets with an original thickness of 4 mm by testing a dedicated cruciform specimen, already optimized in the laboratory. The forming limit strains at fracture of AA5086 sheet under linear and non-linear strain paths (uniaxial tension followed by equi-biaxial stretching) have been characterized. Thinner sheet metals are often used in industry, so a new shape of cruciform specimen with an original thickness of 2 mm was proposed and optimized step by step. This new cruciform specimen is successfully used to investigate the formability of DP600 sheet under linear and two types of non-linear strain paths.

The second objective is to discuss the validity of commonly used ductile fracture criteria to predict the onset of fracture for sheet metal by means of a finite element simulation of the in-plane biaxial tensile test. Some ductile fracture criteria from literature were selected (Cockroft and Latham, Ayada, Oyane ...) and calibrated with experimental results to produce numerical FLCFs for AA5086 and DP600 sheet. Depending on the fracture criterion, numerical results can give very different predictions. Finally, for the two tested materials, it is possible to find a criterion that can predict well the experimental FLCFs for either linear or non-linear strain paths.

INSA RENNES

N° d'ordre : 18ISAR 05 / D18 - 05

Institut National des Sciences Appliquées de Rennes
20, Avenue des Buttes de Coëmes • CS 70839 • F-35708 Rennes Cedex 7
Tel : 02 23 23 82 00 - Fax : 02 23 23 83 96